12-2006

A Robust Conjugate Heat Transfer Methodology with Novel Turbulence Modeling Applied to Internally-Cooled Gas Turbine Airfoils

William York
Clemson University, wyork@clemson.edu

A ROBUST CONJUGATE HEAT TRANSFER METHODOLOGY WITH NOVEL TURBULENCE MODELING APPLIED TO INTERNALLY-COOLED GAS TURBINE AIRFOILS

A Dissertation
Presented to
the Graduate School of
Clemson University

In Partial Fulfillment
of the Requirements for the Degree
Doctor of Philosophy
Mechanical Engineering

---

by
William David York
December 2006

Accepted by:
Dr. James Leylek, Committee Chair
Dr. Richard Miller
Dr. Chenning Tong
Dr. Christian Przirembel

ABSTRACT

Computational fluid dynamics and heat transfer (CFD) has become a viable, physics-based analysis tool for complex flow and/or heat transfer problems in recent years due, in large part, to rapid advances in computing power. CFD based on the Reynolds-averaged Navier-Stokes (RANS) equations is starting to enter the mainstream design environment in certain industries where rapid and reliable predictive capability is necessary. One such application is the gas turbine industry, where thermal management of airfoils at extremely high temperatures is one of the most critical components in engine design for reliability. The problem is complicated by the need for advanced airfoil cooling techniques, which typically includes internal convection cooling.

Current turbine aerothermal design practice involves separate simulations or empirical correlations for the airfoil external aerodynamics and heat transfer, the internal heat transfer, and conduction in the metal part. This approach is time-consuming and quite inefficient when design iterations are required, and accuracy is lost in the decoupling of the heat transfer modes. The physically-realistic approach is a single CFD simulation in which the convective heat transfer (fluid zones) and heat diffusion in the solid are fully coupled. This is known as the conjugate heat transfer (CHT) method, and it is ideally suited to the rigors of design. An obstacle to the adoption of the CHT method is difficulty in the accurate prediction of heat transfer coefficients on both external and internal surfaces, which is usually attributed to performance of the turbulence models used to close the RANS equations.

The present study develops a comprehensive, “best-practice” RANS-based conjugate heat transfer methodology for application to the aerothermal problem of an internally-cooled gas turbine airfoil at realistic operating conditions. With the design environment in mind, attention is given to high-quality mesh generation, efficient solution initialization, and solution-based adaption for grid-independence. Matching the conditions of the only experimental test case available in the literature, the simulations consist of a linear cascade of C3X vanes cooled by air flowing radially through ten smooth-walled cooling channels. Initially, popular “off-the-shelf” k-ε turbulence models are employed. Predictions for vane external surface temperature distribution at the midspan generally agree well with experimental data. The only exception is along a portion of the suction (convex) surface of the airfoil, where the predicted temperature is significantly greater than measured. This indicates an overprediction in the local heat transfer coefficient, and it corresponds to the region of strong curvature of the surface.

In an effort to correct the excessive heat transfer coefficients predicted on the vane suction surface, a new eddy-viscosity-based turbulence model is developed to include correct sensitivity to the effects of streamline curvature (and, by analogy, system rotation). The novel feature of the model is the elimination of second derivatives in the formulation of the eddy-viscosity, making it much more robust than other curvature-sensitive models when implemented in general-purpose solvers with unstructured meshes. A new dynamic two-layer near-wall treatment is included for integration of the flow to the wall. The new model is proven to exhibit physically-accurate results in several fundamental test cases. When the C3X vane conjugate heat transfer simulation is revisited with the new model, the heat transfer coefficients in the region of strong convex

curvature are correctly attenuated, and the wall temperature predictions are much closer to measurements.

Cooling channels in many hot-section turbine airfoils have ribs machined on their walls to augment heat transfer, and they make multiple passes through the airfoil, meaning sharp turns are present. In order to extend the CHT methodology to these more complex internal cooling configurations, work is also conducted on the prediction of heat transfer in ribbed channels and in channel 180^{o}-turns. In the two ribbed-channel cases studied, the use of steady simulations with popular turbulence models result in a significant underprediction of Nusselt numbers on the ribbed walls. Predictions improve significantly with unsteady (time-accurate) RANS simulations using another new in-house turbulence model, which is designed to promote and sustain small-scale unsteady motions. The results clearly show the importance of capturing the unsteady shear layer breakup into roller vortices aft of the ribs. In a simulation of a channel of square cross-section making a sharp 180^{o}–turn, the new curvature-sensitive turbulence model gives Nusselt number predictions that are superior to existing k–ε models. With the added capability to handle complex internal cooling configurations, the conjugate heat transfer methodology becomes a versatile gas turbine aerothermal design tool.

ACKNOWLEDGEMENTS

This work reflects the help and support of so many individuals in my life. First and foremost, I would like to thank my wife, Jennifer, for her patience and encouragement. Appreciation goes to my entire family, especially my mom, dad, and brother, who quietly cheered me on through the years, even though they probably wondered if I would be a student forever. I owe a giant thanks to my advisor of nine years, James Leylek, who has been a mentor, teacher, and friend to me during three degree programs. He always challenged me and gave me the tools to succeed.

I am very lucky to have worked with many smart and stimulating individuals in the Advanced Computational Research Lab. These folks made the days (and sometimes nights) exciting and fun. Special thanks goes to Scott Holloway (the math guru) and Keith Walters (the turbulence modeling guru), who were always there to offer suggestions, answer questions, crack jokes, and listen to me talk. I'd like to thank Will Robinson, who kept the computers and network in the lab running smoothly. I appreciate the efforts of my dissertation committee – Dr. Miller, Dr. Tong, and Dr. Przirembel. And last, but not least, I must thank Casandra Gibson, who unselfishly answered my varied requests for assistance and always brightened the days with her giggling and smiles.

I am grateful for financial support for this research, which came partially from a National Science Foundation Graduate Research Fellowship. Clemson University provided additional support for the work. Appreciation goes to Fluent Inc. and Sun Microsystems for generous grants of computational software and hardware, respectively.

TABLE OF CONTENTS

Table of Contents (Continued)

Table of Contents (Continued)

Page

LIST OF TABLES

LIST OF FIGURES

List of Figures (Continued)

List of Figures (Continued)

List of Figures (Continued)

List of Figures (Continued)

List of Figures (Continued)

List of Figures (Continued)

Figure Page

List of Figures (Continued)

Figure Page

NOMENCLATURE

Acronyms

ACRL	Advanced Computational Research Laboratory at Clemson University
ACRL-EVRC	Eddy-Viscosity model for Rotation and Curvature developed in ACRL
ACRL-EVU	Eddy-Viscosity-based Unsteady model developed in ACRL
ACRL-SDSM	Semi-Deterministic Stress Model developed in ACRL
ASM	Algebraic Stress Model
CFD	Computational Fluid Dynamics and Heat Transfer
CHT	Conjugate Heat Transfer
EVM	Eddy-Viscosity-based Model
INST	instantaneous (in time)
LE	Leading Edge of airfoil
LES	Large Eddy Simulation
PS	Pressure Surface of airfoil
RANS	Reynolds-Averaged Navier-Stokes
RKE	Realizeable k-ε turbulence model
RSM	Differential Reynolds Stress Model
SKE	Standard k-ε turbulence model
SS	Suction Surface of airfoil
TA	Time-Averaged
TE	Trailing Edge of airfoil
URANS	Unsteady Reynolds Averaged Navier-Stokes

Nomenclature (Continued)

Symbols

a	acoustic wave speed in fluid [m/s]
b_{ij}	turbulence anisotropy tensor = $\frac{\widetilde{\overline{\rho}u_i u_j}}{\overline{\rho}k} - \frac{2}{3}\delta_{ij}$
c, c_p	specific heat [J/kg-K]
C_f	skin friction coefficient
C_p	pressure coefficient
C_μ	eddy-viscosity coefficient
D	cooling channel (hydraulic) diameter [m]
e_0	total internal energy = $h - \frac{p}{\rho} + \frac{1}{2}u_i u_i$ [J/kg]
E_0	mass-weighted-averaged total internal energy [J]
F_{ij}	Reynolds-stress rotational production
g	term in algebraic stress model
h	rib height [m], specific enthalpy [J/kg]
h_0	total enthalpy = $h + \frac{1}{2}u_i u_i$ [J/kg]
H	channel height [m]
H_0	mass-weighted-averaged total enthalpy [J]
h_c	convective heat transfer coefficient [W/m^{2}K]
k	turbulent kinetic energy = $\frac{1}{2}\overline{u_i u_i}$ [m^2/s^2]
l	length scale [m]
L	characteristic length, total surface arc length [m]

Nomenclature (Continued)

$\dot{m}$	mass flow rate [kg/s]
Ma	Mach number = V / a
n	normal distance to surface or boundary [m], number of cooling channels
Nu	Nusselt number = hD / κ
p	pressure [N/m^2]
P_{ij}	Reynolds-stress production tensor
P^k	production of turbulent kinetic energy
Pr	Prandtl number
q	heat flux [W]
R	thermal resistance [m^{2}K/W], radius of curvature of streamline [m], gas constant [J/kg-K]
Re	Reynolds number
Re_y	Turbulent Reynolds number for near-wall turbulence model = $\frac{\sqrt{k} \cdot y}{\nu}$
Re_τ	Turbulent Reynolds number for wall-bounded flow = $\frac{u^* h}{\nu}$
Ro	Rotation number = $\frac{\omega H}{U_m^2}$
RP	grid refinement parameter = ωl / V
s	distance along airfoil surface from LE [m]
S	rib spacing [m], strainrate magnitude = $\sqrt{2S_{ij}S_{ij}}$

Nomenclature (Continued)

S_{ij}	rate-of-strain tensor = $\frac{1}{2}\left(\frac{\partial U_i}{\partial x_j}+\frac{\partial U_j}{\partial x_i}\right)$ [s^{-1}]
S_{ij}^*	normalized strain rate tensor
St	Stanton number = $\frac{h_c}{\rho c_p U_{ref}}$
t	time [s]
Δt	time step size [s]
T	temperature [K]
T_{ij}	Reynolds-stress transport tensor
T^k	transport of turbulent kinetic energy
TL	turbulence level = $100 \cdot \sqrt{2k/3}\,/U_\infty$ [%]
u ,v, w	velocity components in the x, y, and z directions, respectively [m/s]
U	mean velocity component (with i, j, k index), velocity magnitude [m/s]
u^*	wall friction velocity = $\sqrt{\tau_w/\rho}$ [m/s]
v	velocity scale [m/s]
W	mean flow rotation rate magnitude = $\sqrt{2W_{ij}W_{ij}}$ [s^{-1}]
W_{ij}	mean flow rotation rate tensor [s^{-1}]
W_{ij}^*	normalized relative rotation rate tensor
$W_{ij}^{'}$	absolute rate-of-rotation tensor = $W_{ij}^{'}=\frac{1}{2}\left(\frac{\partial U_i}{\partial x_j}-\frac{\partial U_j}{\partial x_i}\right)+e_{mji}\omega_m$ [s^{-1}]
x, y, z	cartesian coordinate directions

Nomenclature (Continued)

y^+	non-dimensional wall distance in turbulent boundary layer
Y_M	compressible dissipation term
x'	streamwise distance measured from downstream edge of a rib [m]
β_{ij}	structural parameter = $\frac{\overline{u_i u_j}}{k}$
Δ	magnitude of the rate of volume dilatation [s^{-1}]
ε	dissipation rate of turbulent kinetic energy [m^2/s^3]
ε_{ij}	Reynolds-stress dissipation tensor [m^2/s^3]
η	parameter in algebraic stress model = $\sqrt{S_{ij}^* S_{ij}^*}$
κ	thermal conductivity [W/m-K], von Karman constant
μ	dynamic viscosity [N-s/m^2]
μ_T	turbulent (eddy) viscosity [N-s/m2]
ν	kinematic viscosity [m^2/s]
π_{ij}	pressure-strain correlation in modeled Reynolds-stress equations
ρ	density [kg/m^3]
θ	dimensionless temperature = (T - T_c) / (T_0 - T_c), angle in U-bend
τ_{ij}	stress tensor for Newtonian fluid [N/m^2]
τ_w	wall shear stress [N/m^2]
ω	specific dissipation rate of turbulence, vorticity [s^{-1}]
ω_r	system rotation rate [s^{-1}]
ω_m	angular velocity of reference frame relative to inertial frame [s^{-1}]

Nomenclature (Continued)

Ω	relative rotation rate magnitude = $\sqrt{2\Omega_{ij}\Omega_{ij}}$ [s^{-1}]
Ω_{ij}	relative rotation rate tensor = $\frac{1}{2}\left(\frac{\partial U_i}{\partial x_j} - \frac{\partial U_j}{\partial x_i}\right)$ [s^{-1}]
ζ	parameter in algebraic stress model = $\sqrt{W_{ij}^{*}W_{ij}^{*}}$

Subscripts

c	coolant air total (stagnation) condition, based on airfoil chord length
cond	heat conduction in metal
e	coolant channel exit condition
i, j, k	indices used in tensor notation
i	internal flow/convection, initial condition
IW	airfoil internal (cooling channel) wall
LE	at airfoil leading edge plane
m	mean value over channel cross-section
OW	airfoil outer (external) wall
PS	pressure surface
ref	condition at reference location
SS	suction surface
T	turbulent
TE	at airfoil trailing edge plane
w	from wall or condition at surface
∞	inlet or freestream condition

Nomenclature (Continued)

0	total (stagnation)
α, β	indices used in tensor notation

Superscripts and Operators

”	per unit area
~ (overbar)	instantaneous
¯ (overbar)	ensemble or time average
< >	spatial average
e_{ijk}	tensor permutation operator
δ_{ij}	kronecker delta

CHAPTER 1

INTRODUCTION

Background

Thermal management of hot section components in modern gas turbine engines, employed for propulsion and for land-based power generation, is a complex and critical issue. Increased engine thermodynamic efficiencies have come with a rise in turbine inlet temperatures, in excess of 1600^{o}C in the latest, large turbofan engines. Without innovative cooling schemes, forward-stage turbine airfoils made from the most advanced alloys would fail due to thermal stresses. A plot of approximate turbine inlet temperatures in large commercial aircraft engines over the last half-century is shown in Figure 1.1. The dashed line indicates the material temperature limit, which exhibits a relatively small increase through the years. The large gap between this limit and the current operating temperatures is attributed to advanced cooling designs. Hot section technology is arguably the most critical element in gas turbine design, as evidenced by the millions of dollars spent yearly on research and development in this area. An increase of as little as 10 or 20 degrees in the temperature of a metal part can mean double-digit percentage reductions in the life of the part. Often, increases in engine thrust or power output are limited by the ability to maintain turbine airfoils at acceptable temperatures, as thermodynamic efficiency is directly linked to the turbine inlet temperature.

Modern rotor and stator airfoils comprising the forward-stages of the turbine typically contain internal cooling channels to keep the metal temperature below limits.

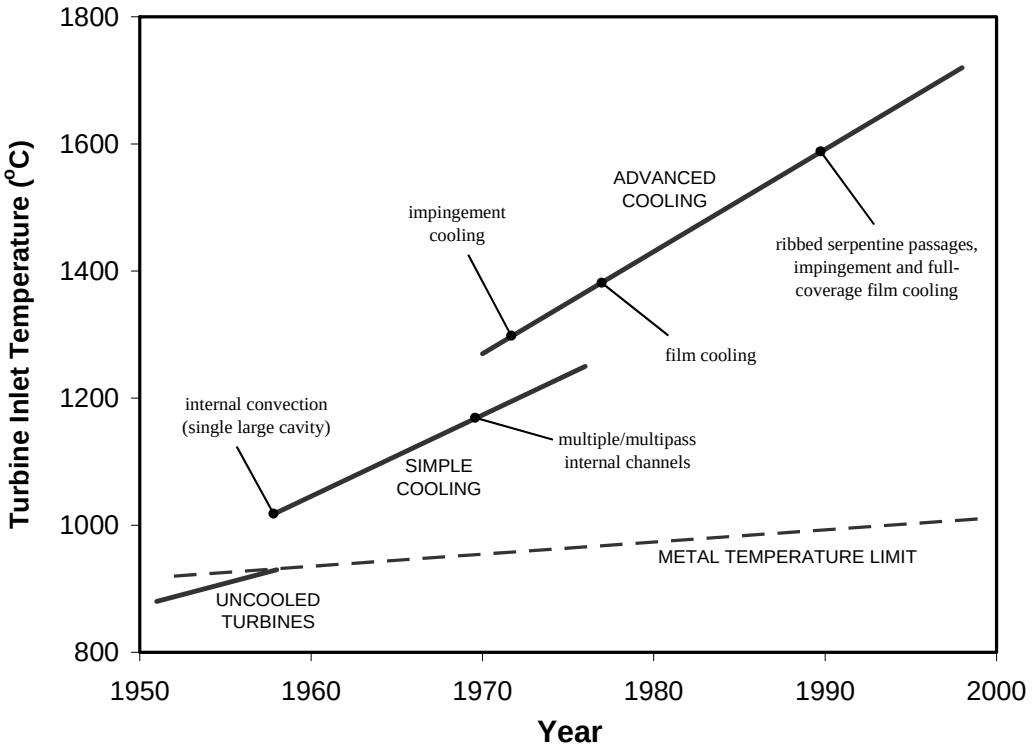

Figure 1.1 Approximate trendlines for turbine inlet temperature as a function of year for the last half-century showing the importance of airfoil cooling. Most data for plot adapted from Bredberg (2002).

The coolant air is bled from the compressor, bypasses the combustion chamber, and is delivered to the turbine airfoils through their hubs. It circulates through the internal passages, removing heat from the metal by convection, and may be expelled into the main gas flow. The geometry of the cooling channels is dictated by the cooling needs of the airfoil and the shape and size of the part. Internal channels for propulsion gas turbine airfoils are commonly “serpentine,” meaning they make multiple spanwise passes through the airfoil, and they often contain ribs on one or more walls to increase turbulence levels and augment convective heat transfer. Optimally, the coolant mass flow should be minimized, as this highly-compressed air removed from the primary gas path

cannot produce power or thrust. This is especially important in gas turbines for aviation applications, where high engine thrust-to-weight ratio is a key design parameter.

Depending on the thermal environment, additional cooling may come from internal impingement cooling, produced by placing thin, perforated inserts just inside of the channel walls, or from film cooling. In film cooling, the coolant air is ejected through arrays of short, small-diameter holes to the exterior of the airfoil, where it will optimally remain in the boundary layer and protect the metal from the hot mainstream. A cut-away sketch of a turbine airfoil showing the internal features and the overall complexity of the cooling design is seen in Figure 1.2. Figure 1.3 shows photographs of an assembly of two high-pressure turbine vanes (stators) from a modern, turbofan engine capable of producing a maximum static thrust in the range of 20,000 to 34,000 pounds. The internal cooling channels with ribs and film cooling holes on the exterior are visible.

Gas turbine manufacturers rely primarily on a “build-and-bust” approach in the design of engine hot-section components. The initial prototype parts are designed with empirically-based correlations for aerodynamics and heat transfer, combined with performance data from previous versions of production engines. Laboratory experiments are extremely difficult and expensive to conduct for realistic engine conditions. Instead, the prototype engine is tested until failure, a process which is costly and time-consuming. There is a great need for a physics-based, predictive design tool to streamline the design process. Computational fluid dynamics and heat transfer (CFD) has the potential to meet this need. But high-fidelity of the computations is vital, since even small inaccuracies in predictions can be amplified when used to estimate the lifespan of parts.

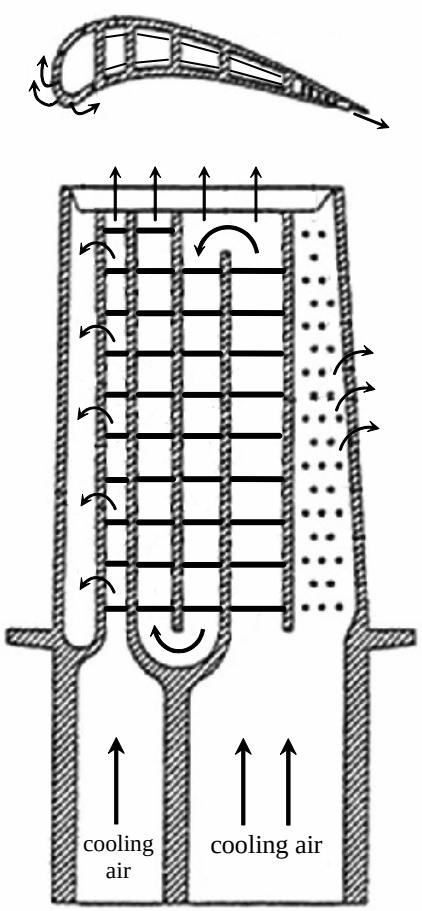

Figure 1.2 Cut-away sketch showing the cooling features of a typical modern turbine blade with ribbed, serpentine cooling channels and film cooling.

In the past two decades, CFD has seen limited use as a supplementary research instrument in the gas turbine industry, but it has yet to become a core element in mainstream design. Early use of CFD in design employed “Euler codes” for inviscid flow, and these simulations were focused at airfoil aerodynamics studies. “Boundary-layer codes”, which solve the parabolized, averaged Navier-Stokes equations, have been used to get one- and two-dimensional heat transfer predictions, but are incapable of simulating recirculating flows or separated boundary-layers. In recent years, three-dimensional (3-D), “general-purpose” Reynolds-averaged Navier-Stokes (RANS) solvers

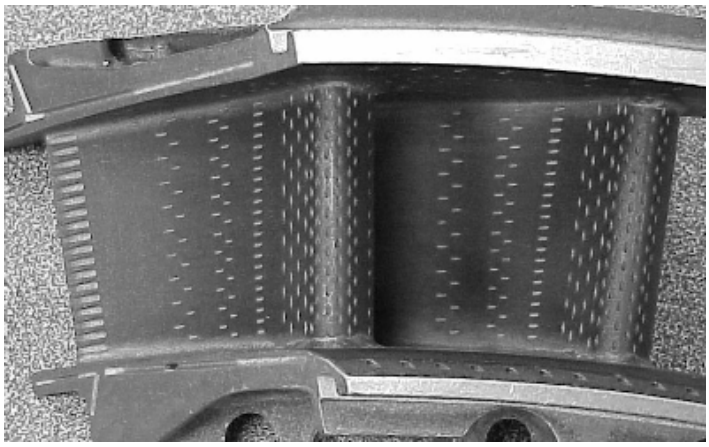

(a) View of leading edge and pressure surface (axial direction)

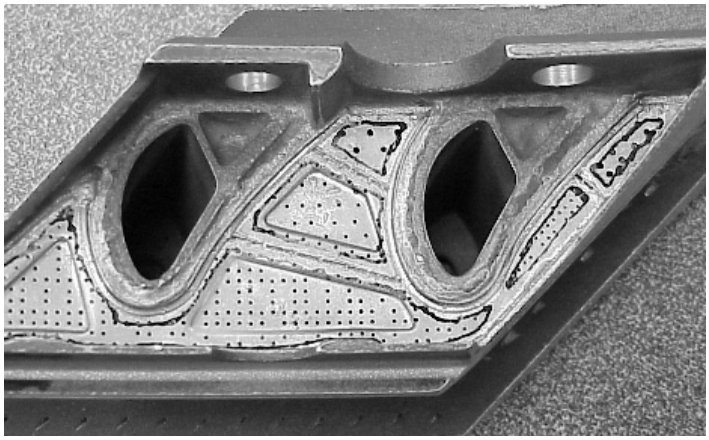

(b) View of base or hub (radial direction)

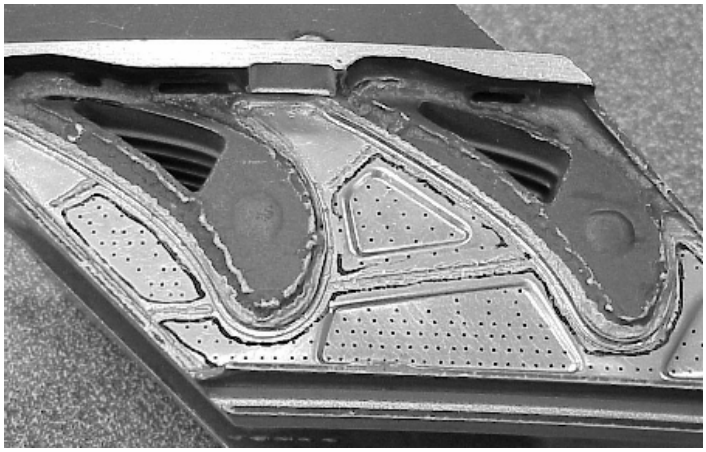

(c) View of tip at casing (radial direction)

Figure 1.3 Photographs of a high-pressure, first-stage, turbine vane assembly from a popular turbofan engine with a rating range of 20,000 to 34,000 lbs static thrust. Visible is the complex cooling design, including ribbed internal passages and numerous film-cooling holes.

have become popular, and many gas turbine companies have turned to commercially-available RANS codes. RANS simulations are ideally suited for a wide variety of fluid flow and heat transfer problems, which may include complex geometries and flow patterns and turbulent and/or compressible flow. It should be noted that two other major classes of CFD solvers are available – Large-Eddy Simulations (LES) and Direct Numerical Simulations (DNS) – but at this point both are too computationally intensive to be used for design of turbomachinery, though they serve as valuable tools for fundamental research in turbulent flows.

Recent leaps in computer technology have made numerical solutions to complex problems feasible, and RANS-based CFD is positioned to be widely integrated into the hot-section design process. For this to occur, computational methods must be tested and validated on realistic problems facing gas turbine designers, not only the fundamental test cases that are prevalent in the literature. In the author's opinion, the goal is a robust computational methodology that may be used with confidence for a wide variety of gas turbine heat transfer problems to yield consistently accurate results. To this end, there is still much work to be completed, including efforts in economic numerical grid generation, solver efficiency and stability, turbulence modeling, and testing and validation. The proposed study will address all of these unresolved issues, with emphasis on turbulence modeling and validation, in an effort to reach the goal set forth above.

The Nature of the Problem and the Conjugate Heat Transfer Approach

The aerodynamic and heat transfer design of a turbine stage is, by nature, a unitary, complex problem. For example, the external aerodynamics (loading) obviously directly impacts the convective heat transfer at the airfoil surface, internal heat transfer

coefficients are linked to total pressure losses in the cooling passages, and thermal diffusion within the metal results in “communication” between the external heat transfer and the internal heat transfer. The current design practice does not employ this physically-realistic coupled approach, primarily because the process is rooted in empiricism gained by studying the individual pieces of the problem. Even with CFD being adopted for certain tasks, the process remains decoupled.

Figure 1.4 illustrates the current “typical” process for the design of a new high-pressure turbine vane. The aerodynamicist is tasked with achieving specific airfoil loading, passage Mach number distribution, and minimizing total pressure losses by specifying airfoil shape, size, and count. Modern CFD codes have been proven to accurately predict aerodynamic loading of airfoils in most cases. The heat transfer design starts with information on the aerodynamic design. Heat transfer coefficients are

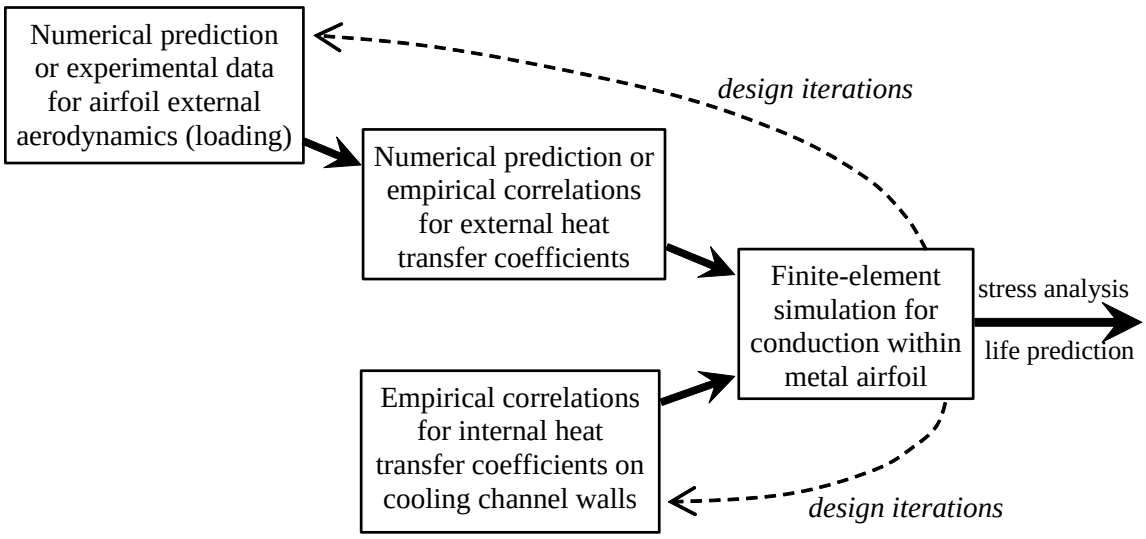

Figure 1.4 General schematic of the current “decoupled” aerothermal design process for an internally-cooled turbine airfoil. The conjugate numerical technique reduces this costly process into a single, “coupled” simulation.

computed with empirical correlations or via one- or two- dimensional boundary-layer computational codes. The internal coolant flow rates depend on the stage inlet temperature and hot gas mass flow rates. Correlations derived from plentiful experimental research on channel flow are usually employed to estimate internal heat transfer coefficients. All of the above data are fed into a finite-element code solving the heat diffusion equation to find the metal temperature distribution. This final step is often performed in conjunction with a stress analysis, since it is the thermal stresses that could result in failure of the part.

Assume that the current design process is carried out, and the temperatures (or stresses) are above the acceptable limits. Some or all of the steps must be repeated with a modified design, and these design iterations in a decoupled environment are quite costly. For example, say the coolant flow rate is increased in one or more internal cooling channels in an effort to reduce the metal temperature. New estimates for the heat transfer coefficients on the channel walls must be obtained with correlations or simulation results. Because of the large temperature differences between the mainstream and coolant, the heat transfer rate between the two fluid zones (via conduction in the metal) is very high. The change in coolant flow rate will reduce the temperature of the external airfoil surface enough to actually change the heat transfer coefficients for the external flow since the fluid properties change with temperature. Therefore, a new simulation must be carried out for the external convection as well. Then another solution for the conduction in the metal must be obtained. Since the heat transfer modes continuously influence each other, for accuracy, numerous simulations would need to be conducted for internal flow, external flow, and heat diffusion in the solid, with results passed back and forth as boundary

conditions. This process becomes a trade-off between economy (number of simulations) and accuracy.

The conjugate heat transfer (CHT) method eliminates the need for a compromise, as it minimizes cost and pushes accuracy to the limits of the discretization scheme and turbulence modeling. The CHT technique is rooted in the physical, coupled nature of the problem, in which a single numerical simulation includes the external aerodynamics and heat transfer, internal flow and heat transfer, and conduction within the metal. In other words, the many steps in the design process (Figure 1.4) are reduced into a single simulation. The only boundary conditions needed are the characteristics of the main gas flow entering and exiting the turbine stage (usually specified with passage inlet total pressure and exit static pressure, inlet total temperature, as well as turbulence quantities) and the coolant temperature and mass flow rates supplied to each of the internal channels. Though the conjugate simulation likely has a larger domain, more finite volumes in the numerical mesh, and therefore greater computational requirements when compared to each phase of the traditional decoupled approach, it is certainly much less costly overall than multiple disconnected simulations that may have to be repeated several times

While the conjugate approach seems like an obvious solution to the problem, since it allows all heat transfer modes to realistically “communicate” with each other, it has only rarely been studied and developed in recent years and has not been adopted into mainstream design. The author is convinced that this is primarily due to two difficulties: (i) the lack of confidence in predicting both external and internal heat transfer coefficients, which causes many designers to question CHT simulation results, and (ii) the relatively high computational cost, since the computational domain cannot be

"simplified" (for example, simplifiying a 3D problem into a 2D approximation). The importance of the latter reason should diminish in the near future as computer technology continues to advance.

One of the main obstacles to an accepted conjugate heat transfer methodology is the consistently accurate numerical prediction of heat transfer coefficients for the internal cooling channels. As discussed previously in this chapter, most coolant channels in modern gas turbine airfoils have ribs, or turbulators, on at least one surface, as well as multiple 180^{o} bends. These two items - ribs and sharp bends - are arguably the source of the greatest deficiencies in the prediction of heat transfer in cooling channels. While it seems like a simple problem for computational methods, since the geometry, grid, and boundary conditions are straightforward, a review of the literature (see Chapter 2) exposed many failed attempts to accurately predict heat transfer in ribbed passages. The reason for the deficiency in CFD predictions lies squarely on the turbulence modeling. All of the readily available turbulence models for RANS simulations are incapable of correctly capturing flow and heat transfer over ribbed surfaces and bends (strong curvature). For the rib case, this is due to the inability of the models to account for small-scale unsteadiness that arises during and after the break-up of the detached shear layer (a Kelvin-Helmholz instability) aft of the rib. In the case of the U-bend, most models do not capture the effect of strong streamline curvature on the turbulence field.

Current Research

The research described in this manuscript is an effort to fill a need in the gas turbine industry for a systematic, validated computational methodology for conjugate heat transfer problems. Because of the nature of cooling for turbine airfoils, it is deemed

to be necessary to include comprehensive numerical study on internal cooling with ribbed channels and investigate heat transfer predictions in channel turns. The current state of research in the field is discussed in depth in Chapter 2, and the need for this work is established. The present research effort will aid in establishing the conjugate heat transfer methodology as a major physics-based tool in mainstream design, where it can greatly reduce design cycle times and costs. The objectives of the research program and the outline of study are clarified in Chapter 3.

CHAPTER 2

LITERATURE REVIEW

This chapter reviews the open literature that pertains to the topics in this proposal. As previously discussed, the final goal of the present work is a comprehensive conjugate heat transfer methodology for predicting heat transfer for internally-cooled turbine vanes. However, this complete work has not yet been accomplished in the open research forum, and therefore the literature survey is best grouped with the component studies of: (i) turbine airfoil conjugate heat transfer simulation; (ii) heat transfer prediction in straight ribbed channels; and (iii) heat transfer prediction in the 180^o turn region of an internal cooling channel. Additional work from the literature pertaining to computational methodologies and turbulence modeling is interspersed in Chapter 4 and Chapter 5.

Conjugate Heat Transfer Methods

Open literature work in conjugate heat transfer (CHT) for turbomachinery applications has been “thin”, and nearly all research has been conducted in the last decade. This is because of the relative infancy of CFD simulations of turbine airfoil heat transfer in general. Most computational work has instead isolated external (hot gas side) heat transfer or internal cooling channels, and coupling with conduction in the metal is omitted. Due to the needs of the industry, however, increasing work in conjugate heat transfer is appearing. Evidence of this is the creation for the first time several years ago of a dedicated “Conjugate Heat Transfer” session (3-5 paper presentations) at the annual International Gas Turbine Congress, sponsored by the International Gas Turbine Institute,

a division of the American Society of Mechanical Engineers. The author has attended and/or participated in two of the three total sessions.

All of the conjugate codes discussed in the literature are based on solution of the Reynolds-averaged Navier-Stokes equations in the fluid regions. It should be noted that any CHT simulations have been conducted without any sort of validation, or comparison with experimental data. This may be due in part to the fact that only a single code validation-quality experiment turned up in a very exhaustive search of the literature. It is the author's opinion that complete validation is an essential part of the CFD process, and these conjugate studies without validation are suspect, owing to the fact that even accurate predictions of heat transfer coefficients are elusive in many cases. Still, one can gain insight on methods from these studies, including ideas for gridding, initialization, discretization and solution algorithms, and *relative* performance of turbulence models.

Due to the lack of experimental studies, some researchers have turned to simpler test configurations to validate their CHT codes. An example is the work of Rigby and Lepicovsky (2001), in which two CHT simulations were performed to mimic some, albeit simplified, features of turbomachinery applications. The first case was laminar flow in a thin-walled metal pipe, and results for the pipe wall temperatures for several Reynolds numbers showed excellent agreement with experiments. The second problem involved a metal plate that was subjected to hot parallel airflow on one side and cool crossflow in a channel on the other. Large discrepancies in the external Nusselt numbers through a range of internal/external Reynolds number combinations was attributed to the one-dimensional heat conduction assumption used to obtain heat transfer coefficients in the experiment.

The work of Hylton et al. (1983) is the only experimental work in the literature on internally-cooled turbine airfoils in which the solid is “active” in a heat diffusion sense. This study is numerically modeled by several researchers for conjugate methods validation purposes. A peculiar aspect of the work of Hylton et al. (1983), contained in a NASA Contractor Report, is that it was not conceived as a CHT benchmarking study, although in recent years it has emerged as just that. The conjugate nature of this study was a consequence of a unique experimental technique to obtain heat transfer coefficients for a turbine vane. The stainless steel test vane was centered in a two-passage (three vane) linear cascade, and was instrumented with thermocouples at the exterior surface at midspan. Ten smooth-walled cooling channels of circular cross-section were oriented radially in the vane. The channels were spaced to give a fairly uniform external wall temperature, and this was aided by adjusting individual coolant flow rates accordingly. The mainstream flow was of fairly engine-realistic Mach number, temperature, and turbulence level. In the experimental run, the steady-state external wall temperature distribution was measured, and this information was used as a boundary condition for a two-dimensional finite element conduction analysis, which employed a correlation for the internal channel heat transfer coefficients. The external heat transfer coefficient distribution could be estimated from the predicted temperature gradients in the metal at the outside surface. Fortunately for researchers seeking validation data for conjugate numerical methods, the authors reported the measured external temperatures on the vane. It should also be noted that Hylton et al. (1983) studied two different vane designs. The first was the “Mark II” vane, which had a non-realistic circular leading edge and a thick

trailing edge. The more engine-realistic vane was the “C3X” design, which was subsequently used in a variety of experiments for nearly a decade.

One of the first conjugate numerical simulations of a cooled turbine airfoil was the work of Bohn et al. (1995). The authors computationally modeled a two-dimensional (2-D) “slice” of the Mark II turbine guide vane from the experiment of Hylton et al. (1983). Experimentally estimated average heat transfer coefficients were prescribed at the interior surfaces of the cooling “channels.” A relatively coarse grid was employed, and a simple algebraic (zero-equation) turbulence model was used with the in-house conjugate code. The predicted external surface temperature was within 2% of that measured by Hylton et al. (1983). The conjugate numerical model of the Mark II was extended to three-dimensions by Bohn and Shonenborn (1996). This work more accurately included the fluid flow in the cooling channels, yet the midspan surface temperature predictions were worse than the 2-D results, as they were significantly higher than the experimental data, especially on the suction surface. Using the same vane geometry, Bohn and Tummers (2003) applied the CHT method to investigate the effects of a thin layer of low-conductivity “thermal barrier coating” on the metal temperature, as well as the effects of reducing the coolant flow rate.

Bohn et al. (1997a) extended their conjugate approach to investigate leading edge film cooling. The showerhead at the leading edge is notorious for its complex thermal field that is greatly influenced by conduction in the metal, and the conjugate approach is more physically realistic than the study of heat transfer coefficients and adiabatic effectiveness separately. The authors modeled a turbine guide vane that was cooled by internal convection in a single plenum near the leading edge and by two slot jets near the

stagnation line. The flow was not calculated in the large internal cooling cavity, and rather a convective boundary condition was applied to the inner walls. The conjugate approach, as compared to a decoupled solution, changed the vane material temperature by up to eight percent of the difference in the mainstream and coolant total temperatures. Bohn et al. (1997b) also used a conjugate solver to investigate discrete-jet film cooling from two round holes at the leading edge of a steel turbine vane. This study employed a multi-block numerical mesh and an algebraic mixing-length model for turbulence closure.

A three-dimensional CHT simulation of a turbine blade convectively cooled with six smooth-walled cooling channels was performed by Bohn et al. (1999). A fairly coarse grid consisting of less than 900,000 nodes was used, and turbulence closure was obtained with an algebraic model, in order to minimize computational expense. The predictions for blade external surface temperature distribution was in reasonable agreement with some experimental data obtained with a thermal paint technique, although it should be noted that the experimental and numerical configurations had some significant differences, making comparison and validation difficult.

Han et al. (2000) performed a conjugate heat transfer simulation of a hollow turbine vane with four internal cooling cavities. They employed an unstructured grid for fast turnaround and a k-ω turbulence model. The three-dimensional vane was created by "stacking" a two-dimensional model, and heat flux boundary conditions were used on the internal walls of the vane instead of solving for the flow of coolant. Experimental data for validation was not available for this configuration. A lack of validation data was also the case for Takahashi et al. (2000), who performed a CHT simulation of a power generation

turbine blade that was cooled by round, smooth-walled channels. Like the previous study, a heat flux boundary condition was imposed on the vane internal surfaces, but the heat flux varied in the radial direction based on the estimation of bulk temperature in the coolant channels. At the blade tip, the coolant velocity and temperatures were prescribed to simulate mixing with the hot mainstream. Various parameters were varied to determine the effect on metal temperature distribution.

The CHT method was applied by Kusterer et al. (2004) to investigate a modern gas turbine vane cooled internally with serpentine passages and film cooling at the leading edge, on the pressure and suction surfaces, and at trailing edge. However, the computational model was simplified significantly from corresponding experiments, which employed a thermal paint method to obtain wall temperatures. One phase of the computations isolated the CHT zone at the leading edge region, with the rest of the airfoil having adiabatic walls, and the second phase neglected the leading edge film cooling and internal cooling channel. Additionally, less than half of the metal blade in the spanwise dimension (the tip portion) was included in the conjugate computational domain. Mesh sizes for the two phases of the study were 3.1 and 4.4 million finite volumes, and turbulence closure was accomplished with a simple algebraic model. Both “design point” and “off-design” conditions were tested. Validation was again questionable due to key differences between the experiment and computations. Kusterer et al. (2005) used the same CHT method and numerical model to suggest improvements to the cooling of this same blade, namely repositioning of cooling holes to reduce heat flux into the metal.

A different conjugate approach is the boundary element method (BEM), in which the governing heat diffusion equation is not discretized and solved in solid zones. Since

thermal diffusion in a solid is governed by the Laplace equation for temperature, it may be solved for the temperature distribution using only boundary discretization (which couples with the fluid-side solution). This method was used by Heidmann et al. (2003), to simulate a film-cooled vane. Only a single film-hole pitch in the radial direction was included, and therefore the simulation neglected convection due to the radial flow of cooling in the internal channels. This method allows only the use of a constant thermal conductivity in the solid, which is not accurate due to the large temperature differences within a turbine airfoil at realistic operating conditions. No comparison with any experimental data was made, so it was difficult to gauge the performance of the BEM method or the k-ω turbulence model. It should be noted that Heidmann et al. (2003) reported that each BEM step (conduction solver) took 25 times longer than the explicit flow solver time step. This seems to be a disadvantage of the BEM method as compared to the more traditional volume-discretized method, considering that the former does not have increased accuracy.

Several researchers have used commercial codes for CHT analysis of turbine airfoil heat transfer. Takahashi et al. (2005) used the Fluent code from Fluent, Inc. to investigate metal temperatures in a land-based gas turbine rotor blade cooled with ribbed internal passages. However, the actual convection in the cooling channels was omitted and instead accounted for with empirical correlations. The one-equation turbulence model of Spalart and Allmaras (1992) was used for closure in the external flow region. The numerical results were not compared to experimental data. Mazur et al. (2005) used the STAR-CD code from CD-adapco with the Renormalization Group (RNG) k-ε turbulence model of Yakhot and Orszag (1992) to predict temperature within a realistic

first-stage turbine nozzle. Again, no direct measurements from a corresponding experiment were available for validation.

Facchini et al. (2005) used the STAR-CD code to conduct a CHT validation study of the C3X Vane, investigated experimentally by Hylton et al. (1983) and numerically by several researchers discussed previously. Three turbulence models were used: (i) a low-Re k-ε model, (ii) the RNG k-ε model of Yakhot and Orszag (1992) combined with a one-equation model near the wall, and (iii) a high-Re k-ε model modified to satisfy the realizability constraints for the Reynolds stresses. All three models significantly overpredicted the heat transfer coefficients over the entire airfoil, most notably the low-Re version, and therefore in all cases the predicted wall temperature was greater than the measurements, especially at the leading edge. The authors attributed this to the inability to accurately capture the initially laminar boundary layer on the vane external surface and its transition to turbulence. Facchini et al. (2005) tested this hypothesis with a simple two-dimension simulation of the C3X vane with an intermittency-based boundary layer transition model. This proved to bring the predicted heat transfer coefficients in line with experiments. The need for models accounting for realistic laminar-to-turbulent boundary layer transition was also shown by Chmielniak et al. (2003), who performed a CHT simulation of a radially-cooled turbine blade.

Ribbed-Channel Heat Transfer

Heat transfer in ribbed channels has been an active research area for several decades because of the need for augmented internal heat transfer in many applications, including gas turbine cooling, heat exchangers, and cooling of electronic packages. Ribs added to the channel walls are often called “turbulators” for their contributions to

increasing turbulence levels, and consequently they provide a relatively cheap method for greatly increasing heat transfer coefficients. Early work was experimental in nature and open-literature papers number in the hundreds. Much recent experimental work focuses on optimization of rib geometry, including their size, shape, spacing, and orientation to the flow. Because of the large body of experimental work in this area, as well as the scope of the proposed research, experimental work will not be discussed unless experiments are combined with computations or used as validation for CFD.

Due to the wide applications of the problem, as well as the relative ease of modeling the geometry and building numerical meshes, computational studies of ribbed passage flow and heat transfer have been extensive. The problem appears simple at first glance, but most researchers have found difficulty in accurately predicting heat transfer and turbulence quantities due to the complexities of detached shear layers aft of the ribs. All of the early computational efforts on ribbed channel flow and heat transfer involved steady-state Reynolds-Averaged Navier-Stokes (RANS) simulations, closed with a variety of popular turbulence models. Liou et al. (1991) conducted a two-dimensional (2-D) numerical study of heat transfer in a ribbed passage using a k-ε turbulence model. They found a peak Nusselt number just upstream of the reattachment point between two ribs. Switching to an algebraic Reynolds stress model, Liou et al. (1992) observed better agreement with measured heat transfer data, attributing this fact to the anisotropy in the turbulent fluctuations allowed by the latter model.

Three-dimensional (3-D) studies add the realistic effects of the sidewalls, and are mush more computationally intensive than 2-D studies. Prakash and Zerkle (1995) investigated the performance of an economical wall-function approach in conjunction

with the *k*-ε model in a 3-D simulation of a single rib pitch in a straight channel with ribs on opposite walls. They found a slight underprediction of heat transfer when compared to textbook correlations. Interestingly, the authors stated that the results were significantly worse for the same case employing the more physically-accurate two-layer near wall treatment, for which the flow field is resolved down to the wall, but one should keep in mind that no experimental data on the configuration was available for comparison. In contrast, the wall function approach was deemed inappropriate for ribbed passage flows by Iacovides and Raisee (1999), who simulated two ribbed-channel configurations using three different closure models. The tested models were a zonal *k*-ε model, a zonal differential Reynolds stress model, and a low-Reynolds number differential stress model. Like most other numerical studies, the heat transfer predictions fell short of the experimental data, and the authors attributed this to the inability of the turbulence models to accurately capture flow in the separation zone aft of the ribs.

Bredberg and Davidson (1999) predicted heat transfer in a two-dimensional ribbed channel using four turbulence models: a zonal *k*-ε model, two different k-ω models, and an explicit algebraic Reynolds stress model. For a Reynolds number of Re=12,600, all turbulence models underpredicted Nusselt numbers as compared to experimental values. The authors stated the possibility that recirculation zones between ribs were not accurately captured and the turbulence levels very near the wall could be too low in the simulations. Bonhoff et al. (1999), using empirical correlations for comparison, found that the full differential Reynolds Stress Model (RSM) in the Fluent code gave results for heat transfer in a two-pass channel with angles ribs that were only slightly superior to the *k*-ε model. However, simulating a very comparable case as the

previous authors, Jang et al. (2001) concluded that anisotropy in the turbulent stresses was very important, and therefore the RSM was far superior to two-equation eddy-viscosity models for this class of problems.

All of the ribbed-passage numerical studies discussed above used a steady framework. However, the detached shear layer aft of a rib will naturally become unstable and result in small-scale (slightly larger than the scales of turbulence), semi-deterministic, unsteady motion. Several researchers, including Saha and Acharya (2003) and the present author in a paper by McDowell et al. (2003), proposed that resolving the unsteady flow field might be a key in the accurate prediction of heat transfer. Two types of unsteady simulations may be employed, neglecting a Direct Numerical Simulation, which is far too computationally intensive for the application. These methods are Unsteady RANS (URANS) and Large-Eddy Simulation (LES).

The obvious solution is to simply “turn on” the unsteady term in a RANS simulation. However, most common turbulence models are so diffusive that all physically realistic oscillations in time are damped out, and a steady solution results. This was seen by the present author and documented in the paper by McDowell et al. (2003), which discusses an unsuccessful attempted to get unsteady behavior with URANS closed by the standard and realizable versions of the k-ε model in a simulation of a channel with rounded ribs on top and bottom walls. Unsteady motions in a URANS simulation may be sustained with the aid of very-high order discretization schemes, at a very high computational cost, which was done by Saha and Acharya (2003). Instead, McDowell et al. (2003) employed a novel unsteady turbulence model developed in Clemson University’s ACRL to allow the realistic unsteadiness to occur. The predicted area-

averaged, time-averaged Nusselt number at the highest studied Reynolds number was within 20 percent of measured, as compared to almost 50 percent underprediction with steady RANS, and this result highlights the significance of the unsteadiness on wall heat transfer.

Saha and Acharya (2003) employed URANS and LES to study fully-developed flow and heat transfer in a rotating channel with ribs on opposite walls using a streamwise periodic boundary condition. While there were differences in the unsteady flow structures between the two approaches, both heat transfer predictions were fairly close to each other. URANS gave about a 10 percent overprediction in area-averaged heat transfer when compared to experimental data, while LES showed a slightly larger discrepancy. Although it should be stated that the numerical model did not fully match the experimental setup, and, for example, the simulations employed square ribs, while the experiment utilized rounded ribs. The URANS approach was extended to study the effect of channel aspect ratio by Saha and Acharya (2004). Watanabe and Takahashi (2002) exclusively employed LES with a standard and dynamic Smagorinsky subgrid turbulence model to study fully-developed heat transfer on a wall of a channel with transverse ribs at a relatively high Reynolds number of 107,000. The predictions with the dynamic subgrid model were in fairly good agreement with experimental results obtained by the same authors, and the unsteady physics enhancing heat transfer were shown.

Tafti (2003) used LES to investigate fully-developed (via streamwise periodic boundary condition) flow and heat transfer in a narrow channel with square ribs on the bottom wall. The author claimed that popular subgrid-scale models could be unstable or too dissipative (damping small-scale unsteadiness), and therefore no subgrid model was

employed, meaning that the scales of turbulent and/or unsteady fluctuations smaller than the grid size were not modeled or resolved. Heat transfer predictions fell about 20% below measured data from a similar experiment, but reproduced all of the qualitative trends. Heat transfer coefficients were seen to be highest just upstream of the rib due to highly unsteady vortices in this area, and another local peak in heat transfer was located just upstream of reattachment about a little more than 3 rib heights aft of the rib. Sewall and Tafti (2004) utilized the same LES method to study developing flow heat transfer by modeling 6 ribs in the same channel. A numerical mesh of 6.2 million cells was used in the study. Results showed that the turbulence quantities and heat transfer were fully-developed after the third rib, while the mean flow stopped varying after the fourth or fifth rib. Heat transfer predictions for the ribbed wall were slightly less than experimental data. This same LES methodology was also used by Viswanathan and Tafti (2005) to study a channel with staggered, rounded ribs on opposite walls.

One additional numerical method may be used to capture unsteadiness, with a theoretical slight reduction in computational cost compared with LES. This method is hybrid RANS / LES approach called a Detached Eddy Simulation (DES). LES is employed in the regions where small-scale unsteady fluctuations are important, such as in the detached shear layer aft of the ribs, and RANS is used everywhere else. This approach was utilized by Viswanathan and Tafti (2005), with a k-ω model used for closure in the RANS regions, to simulate fully-developed flow in a channel with staggered 45^{o} ribs on opposite walls. A conventional URANS simulation was run for comparison, and LES results and measured data were also available for the matching case in a paper by Abdel-Wahab and Tafti (2004). All three simulations captured the unsteady,

helical vortex aft of the angled rib. DES performed better than LES and URANS in reproducing mean velocity profiles. Interestingly, both DES and URANS area-averaged heat transfer predictions on the ribbed walls were within 7% of measured, while the LES result was the least accurate with a 15% underprediction.

Heat Transfer in a 180^o Channel Bend

Most modern gas turbine airfoils are cooled with air flowing through internal channels making multiple radial passes through the part (see Figure 1.3), and therefore the channels have one or more 180^o turns. Since the outer surface area in a bend region is relatively large, and because of its proximity to the highly-stressed hub or tip, a number of studies of heat transfer in the channel turn have been conducted. Experimental work appearing in the literature on this subject has been fairly extensive, due to the wide application of curved channel heat transfer and the relative simplicity of the experimental setup. Numerical studies have been conducted typically to assess the performance of turbulence models in handling the effects of strong streamline curvature, and this section will examine several of these studies. Recently, several papers have been published on computational work on 180^o turns with ribs prior to and inside the turn itself, such as the LES study of Sewall and Tafti (2005). However, to remain within the context of the present work, only smooth-walled studies with small turn radii are discussed.

Numerical studies of this class of problems usually fall into two geometric groups, with the first being the sharp U-bend, a 180^o turn with a constant channel width through the turn. An early work in this class was that of Besserman and Tanrikut (1991), who found that the standard k-ε model with a wall-function approach could not reproduce the flow features or heat transfer in the strongly-curved region. Iacovides et al. (1996)

used several turbulence models to study the flow development in a sharp U-bend, and compared mean velocity profiles and turbulent stresses to measurements obtained with laser doppler velocimetry. Results showed that a high-Reynolds number k-ε model with a two-layer near wall treatment was unable to reproduce the effects of strong streamline curvature on the turbulence field, leading to large discrepancies also in the mean flow profiles. An algebraic Reynolds-stress model (ASM) better captured this effect, but was still unable to accurately predict the flow behavior just downstream of the bend. In an effort to capture the streamline curvature effect in an economical model, Amano et al. (2005) used a nonlinear low-Re k-ω model to study flow for this same case, and also employed a popular linear low-Reynolds number k-ε model for comparison. The nonlinear model did the best in capturing mean velocity profiles in the bend, attributed to the ability of the model to resolve anisotropy in the turbulent stresses. However, neither of the models performed consistently well, and both could not reproduce trends in the turbulence quantities and in the mean profiles downstream of the bend.

The two-dimensional sharp U-bend flow (originally named a “turnaround duct” for aerospace propulsion applications) studied experimentally by Monson et al. (1990) has proven to be a good test case for assessing turbulence model performance. Numerous researchers including Monson et al. (1990), Shur et al. (2000), Rumsey et al. (2000), Fu and Qiam (2002), and Rahman and Siikonen (2005) used this case for assessing the sensitivity of turbulence models to streamline curvature. A variety of full differential Reynolds-stress models, algebraic stress models, nonlinear eddy-viscosity models, and linear eddy-viscosity models were used by the various authors. Generally, the Reynolds-stress models performed the best in prediction of mean velocity profiles, turbulence

profiles, shear stress, and pressure in the sharp bend. The complicated nonlinear eddy-viscosity models performed only slightly better than the linear models, and neither class could consistently reproduce the augmented turbulent kinetic energy near the outer (concave) wall, leading to poor prediction of the mean velocity near the outer wall.

Another configuration studied in recent years is the sharp 180^{o} turn with squared outside walls. This geometry is more realistic for turbine airfoil cooling operations, where the short wall that is normal to the bend entry and exit flow direction would be located very near the hub or tip of the airfoil. This type of setup was numerically studied by Rigby et al. (2002) using a k-ω model and a differential Reynolds stress model (RSM). The effect of grid density was also investigated. Results showed a complex flow behavior in the turn with significant secondary flow. Heat transfer predictions with the RSM on the top/bottom walls showed some major differences as compared to experimental data, and the grid density had a strong effect on the results, with the very dense grid giving the most accurate prediction. The authors suggested that discrepancies in heat transfer results were owed to the RSM's inability to accurately predict turbulence levels in regions of strong flow acceleration and impingement. A similar configuration as the previous study was simulated by Nikas and Iacovides (2003) with several Low-Re eddy-viscosity and differential Reynolds-stress models, and again the RSM-class models performed the best in the prediction of heat transfer in the bend region.

Outstanding Issues

The thorough review of the open literature reveals some issues that remain unresolved, leaving a need for additional research in the important areas on computational heat transfer for gas turbine airfoils discussed above. High-fidelity, 3-D,

conjugate heat transfer simulations for realistic turbine airfoils is still a computationally expensive effort by today's computing standards, Therefore, most, if not all, studies in the literature have either simplified the problem by artificially decoupling the internal convection (or employed correlations) or have used simple zero- or one-equation turbulence models, known to have major deficiencies. Many of the conjugate studies have no validation whatsoever, not even a comparison of heat transfer coefficients, which are well-known to be difficult to predict accurately. This lack of validation, combined with "shortcuts" in the methodology, turns many of these studies into academic exercises instead of foundations upon which to build valuable design tools.

The literature review makes it obvious that, while quite a few numerical works are published on ribbed-channel heat transfer, the results are in disagreement with experimental data and with each other. Confidence in predictive capability has not been established. Recent studies involving unsteady simulations are proving to be more accurate than steady simulations with off-the-shelf turbulence models, but even these URANS and LES simulations give mixed results. In addition, unsteady simulations are very computationally expensive, and this fact makes it unattractive to employ in a conjugate heat transfer simulation of a cooled airfoil with a large numerical grid.

When it comes to predicting flow development and heat transfer in U-bends that join the straight coolant channel sections, it is apparent that all "off-the-shelf" turbulence models fall short. This is primarily due to their inability to handle the effects of strong streamline curvature on the turbulence field. The Reynolds-stress models give better results, but at a cost of much greater computational intensity and numerical stiffness.

Modified eddy-viscosity models are showing promise, but additional effort is needed in developing economical turbulence models that capture streamline curvature effects.

Finally, absent in the literature is a comprehensive methodology for conjugate heat transfer simulations of internally-cooled turbine airfoils that includes full testing and validation. This includes the investigation into the proper methods, including turbulence models, to handle each piece of the complex problem - external flow, straight ribbed-channel and180^{o}-turn heat transfer, and coupled conduction - with the goal of highest accuracy and economy.

CHAPTER 3

OBJECTIVES AND OVERVIEW

Research Objectives

While there are many objectives to the present study, and numerous simulations to be conducted, the principle goal of this research can be stated as follows:

Develop, validate, and document a systematic computational methodology for conjugate heat transfer analysis of internally-cooled gas turbine airfoils.

Within this goal are a number of major objectives, stated below:

- Develop "best-practice" methods for conjugate heat transfer simulations starting from a commercially-available RANS-based solver infrastructure, and demonstrate this capability through systematic validation with experimental data.

- Improve the predictive capability of RANS simulations in predicting heat transfer in channels with rib turbulators and sharp 180^{o}-bends, features that are characteristic of realistic internal cooling passages in turbine airfoils.

- Test the performance of "off-the-shelf" turbulence models in all simulations, and, if these models fall short, employ novel turbulence models developed in-house and/or develop new turbulence models.

- Optimize the methodology for use in mainstream design, reducing complexity and computational expense, while maintaining accuracy.

Research Overview

The work herein is broken into several key phases, which were conducted concurrently. The first phase specifically investigates conjugate heat transfer simulations for a cooled airfoil. Because of the availability of validation-quality experiments to model, and also the difficulties in prediction of ribbed-channel heat transfer, this portion of the work will model a turbine guide vane at engine-realistic operation conditions,

including high inlet temperature, turbulence level, and passage Mach number, that is cooled by air flowing radially through a number of smooth-walled passages. Gridding methods for the conjugate problem, efficient solution initialization, the fluid-solid interface energy coupling, and convergence and grid-independence will be investigated. Turbulence model performance will also be investigated, and the need for improved modeling to include streamline curvature effects will be discussed. In this phase, the general conjugate methodology for an internally-cooled airfoil will be developed and validated.

Another phase of the research will isolate RANS simulations of ribbed-channel heat transfer, which the literature (and in-house experience) has shown to be very elusive to predict. Considering that there are no conjugate heat transfer experimental test cases available in the literature, the ribbed-channel heat transfer predictive capability is studied separately. Several different test cases based on experiments will be numerically modeled. This part of the study will heavily investigate turbulence modeling performance, both commercially-available models built-in the solver, as well as in-house models developed in Clemson's Advanced Computational Research Laboratory (ACRL) and implemented in the code through User-Defined Functions (UDF). Also, the importance of modeling the unsteady flow features on heat transfer predictions will be explored.

The final portion of the study will focus on the development and testing of a new turbulence model that contains streamline curvature (and by analogy, system rotation) effects, but retains the robustness of popular eddy-viscosity models. The need for the new model stems from two pertinent areas of the present study. The first is the potential

improvement of external heat transfer, and therefore metal temperature, predictions in a CHT turbine airfoil simulation. The second purpose is the improvement of heat transfer predictions in the sharp 180^{o}- turn regions of internal channels. Good predictive capability in this area further widens the applicability of the overall conjugate heat transfer methodology by allowing multi-pass cooling channels to be included.

With methods developed, validated, and optimized in each phase of the research, the final result will be a conjugate heat transfer methodology that may be used with confidence to predict internal metal temperature field in a gas turbine vane at operating conditions with any type of internal channel cooling design – ribbed or non-ribbed and multi-pass or single-pass. It may seem constructive to perform a simulation of an active-metal turbine airfoil with ribbed, serpentine internal passages in order to tie all phases together. However, it is not currently possible to create a pertinent validation test case because the experimental counterpart does not exist in the open literature. Fortunately, when a validated conjugate methodology is combined with accurate predictive capability for ribbed, multi-pass, channel heat transfer, then a proven general methodology is implicit. Also, based on an exhaustive review of the literature and a request for information from representatives in the gas turbine industry, there is no experiment on which to model a conjugate simulation of an airfoil with ribbed passages. Therefore, adding ribbed channels to a conjugate simulation would involve selection of an arbitrary cooling configuration, and further validation would be impossible. This simulation would be for “show” only, and would not strengthen the methods development goals of the present work.

On the Universality of the Research Program

It should be explicitly noted that the methods development work presented in this proposal are applicable to a wide variety of fluid dynamics and heat transfer problems. The author is familiar with the design process of the gas turbine industry through past experience with private-sector sponsorship of research projects in the Advanced Computational Research Laboratory at Clemson University. With knowledge of hot-section design process, it is evident that the need for and potential impact in this field of a complete conjugate numerical design tool is substantial. That is not to say that the benefit of the present work is exclusive to the gas turbine industry. While the motivation behind the present research is rooted in the gas turbine field, and the simulations represent important problems in gas turbine heat transfer, the methods and tools developed are actually generalized, and not “hard-wired” to this area. For example, the new turbulence model developed as part of this work is a general-purpose model that is designed to work for any flow in which curvature and/or rotation effects on the turbulence field may be important.

The conjugate heat transfer simulation of an internally-cooled turbine airfoil represents a stringent test-case for any methods development project, with complicated geometry, highly-compressible flow, transitional boundary layers, strong streamline curvature, and local unsteadiness in the flow field, just to name a few of the complexities. If computational methods can be validated for this problem, then it can be easily transferred with confidence to solve many other problems in thermal engineering. For example, the methodology and tools could easily be applied to the problem of thermal management of cylinder heads in internal combustion engines, a problem that involves all

of the traits listed above, except that typically Mach numbers are lower than in the turbine problem. Analysis and design of heat exchangers, which also involve two convection problems coupled through heat conduction in the solid boundaries, is another application of the conjugate methodology. Additionally, through the heat-mass transfer analogy, the conjugate method may also be readily extended to mass transfer problems that involve coupled convection and diffusion of a species within a solid or a membrane, including biomedical applications.

CHAPTER 4

GENERAL METHODOLOGY

This chapter discusses the general computational methods adopted for all simulations conducted in the present study. The computational methodology has been developed, tested, and refined by several researchers, present author included, in over a decade of experience with gas turbine CFD research in the Advanced Computational Research Laboratory (ACRL) at Clemson University. It is a systematic, “best-practice” approach, in which every effort is made to minimize errors at each step of the numerical process. When careful modeling of the problem is combined with the highest-quality numerical grid and a mature commercial solver, the only remaining “obstacle” to obtaining consistently accurate results is turbulence modeling. Recent efforts in this area have made improvements in predictive capability for gas turbine aerothermal problems, but further innovations in turbulence closure are needed.

Computational Model

The computational model serves as the foundation of the general methodology, and includes the proper domain, geometry, and boundary condition selection. It is imperative that the computational model accurately simulates the real-life problem. This seems like an obvious requirement, but countless numerical studies in the literature have involved shortcuts that caused a deviation from the original problem, and this usually results from a need to reduce computational expense. The author’s approach is to ensure that the exact problem is modeled, regardless of expense, and look for ways to optimize

the numerical process in other areas. For all of the simulations discussed in the present work, methods testing and validation is a main goal, and the geometry and boundary conditions are taken directly from an experiment documented in the literature. The Gambit software package from Fluent, Inc. is used to create the numerical domains for the simulations in this study.

Numerical Grid

The gridding phase involves filling the entire computational domain with a mesh of finite volumes, or cells, each with a grid point at its center. It is over this grid that the governing equations are discretized and solved. Gridding is often the most time-consuming and labor-intensive task in the numerical procedure, and it can have major implications on the fidelity of the final results. The present work uses a "superblock" technique, in which the domain is divided into tens, or even hundreds, of cell zones, maximizing quality and allowing the mesh to be tailored to the local conditions. The multi-topology, unstructured mesh may contain hexahedra, tetrahedra, pyramid, and triangular prism cells in three-dimensional (3D) space (quadrilaterals and triangles in 2D). The initial mesh is developed in the Gamibit pre-processor, and, in some cases, TGrid software from Fluent, Inc. is also employed in the creation of 3D grids.

Grid quality is a subjective term measured by different parameters. The traditional measure of is the overall skewness of the cells. Skewness indicates the degree of deviation from the "perfect" cell for that topology. For example, a perfect (zero skewness and highest quality) 3D hexahedra cell would have all edges meeting each other at right angles, and the perfect 2D triangle cell is equilateral with congruent interior angles of 60^{o}. In addition, the cell aspect ratio and size or density may influence the overall quality

of the grid. Cell aspect ratio is used to characterize hexahedra or prism cells, and describes the ratio of cell dimensions, such as characteristic length in x-direction compared to length in y-direction. In areas where the flow is highly two- or three-dimensional, such as in a wake or unstable shear layer, it is imperative to keep all cells at aspect ratio near unity. The cell size must also be small enough to resolve the flow structures. In regions where a certain flow direction dominates, as in the freestream, the cells may be stretched in the flow direction to reduce cell count and computational requirements. Generally, the cell spacing must be small (with high grid density) in any direction that large gradients exist, such as across a boundary layer or normal to a shear layer.

Extra care is taken to ensure high grid quality and density along solid boundaries. Layers of closely-spaced hexahedra or prism cells are placed near the wall to ensure that the full turbulent boundary layer is resolved, including the narrow viscous sublayer. Cells are typically stretched slightly away from the wall as flow gradients decrease. About fifteen to twenty grid points are located within the height of the boundary layer, and the first grid point is located at $y^+ < 1$ (deep within the sublayer). This approach works in conjunction with the two-layer, near-wall turbulence model (discussed in more detail later), and is used exclusively in the present work. A representative grid diagram is shown in Figure 4.1(a). To the right in Figure 4.1(b) is a diagram of a much less computationally expensive near-wall grid, used with the wall-function approach, in which the boundary layer is approximated with a correlation, but not resolved. This cheaper method is popular, especially in large 3D simulations. However, Ferguson et al. (1998) and other researchers have found that the extra expense to resolve the full boundary layer,

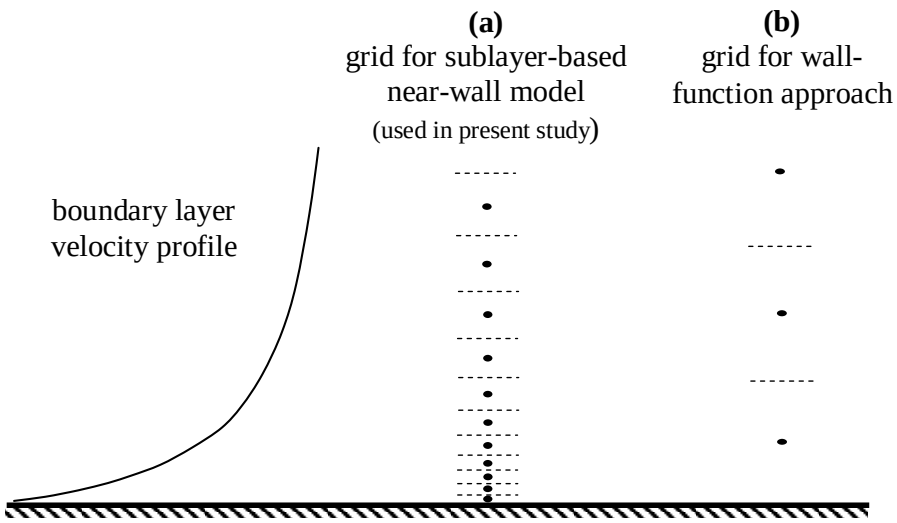

Figure 4.1. Near-wall grid requirements for (a) a sublayer-based turbulence model, such as the two-layer approach used in the present work and for (b) a wall-function approach.

including the viscous sublayer, is necessary for accurate heat transfer predictions. For this reason, this less physically-correct technique is not used in this study at any surfaces where heat transfer is occurring or is being predicted. Previous experience (York, 2000) has also revealed the importance of uniform spacing of the wall-adjacent grid points from the wall to ensure accuracy in prediction of heat transfer coefficients.

Governing Equations and Time-Averaging

Depending on the nature of the problem, the governing equations may consist of conservation of mass (continuity), conservation of momentum (Navier-Stokes), and conservation of energy. They are listed below in that order, and instantaneous dependent variables are shown with a tilde (~) overbar. The energy equation is given in terms of total energy, e_0, and total enthalpy, h_0.

$$\frac{\partial \tilde{\rho}}{\partial t} + \frac{\partial}{\partial x_j}\left(\tilde{\rho}\tilde{u}_j\right) = 0 \tag{4.1}$$

$$\frac{\partial\left(\tilde{\rho}\tilde{u}_i\right)}{\partial t} + \frac{\partial}{\partial x_j}\left(\tilde{\rho}\tilde{u}_i\tilde{u}_j\right) = -\frac{\partial \tilde{p}}{\partial x_i} + \frac{\partial \tilde{\tau}_{ij}}{\partial x_j} \tag{4.2}$$

$$\frac{\partial\left(\tilde{\rho}\tilde{e}_0\right)}{\partial t} + \frac{\partial}{\partial x_j}\left(\tilde{\rho}\tilde{u}_j\tilde{h}_0\right) = -\frac{\partial \tilde{q}_j}{\partial x_j} + \frac{\partial}{\partial x_j}\left(\tilde{u}_i\tilde{\tau}_{ij}\right) \tag{4.3}$$

The viscous stress tensor for a Newtonian fluid, τ_{ij}, is given by:

$$\tilde{\tau}_{ij} = \mu\left[\left(\frac{\partial \tilde{u}_i}{\partial x_j} + \frac{\partial \tilde{u}_j}{\partial x_i}\right) - \frac{2}{3}\delta_{ij}\frac{\partial \tilde{u}_k}{\partial x_k}\right] \tag{4.4}$$

and q_j is the diffusive heat flux vector, following the Fourier law:

$$\tilde{q}_j = -k_c\frac{\partial \tilde{T}}{\partial x_j} \tag{4.5}$$

For a perfect gas, the total enthalpy is defined as:

$$\tilde{h}_0 = \tilde{e}_0 + \frac{\tilde{p}}{\tilde{\rho}} = c_p T + \frac{1}{2}\tilde{u}_i\tilde{u}_i \tag{4.6}$$

Finally, the gas (air) is assumed to obey the ideal gas equation of state:

$$\tilde{p} = \tilde{\rho}R\tilde{T} \tag{4.7}$$

To allow a numerical solution, the instantaneous governing equations are first averaged over time. Many of the complex flows discussed in this work have varying density, due to both temperature variations and compressibility effects. Therefore, it is necessary to use a mass-weighted time averaging, or Favre-averaging, instead of traditional time averaging, or Reynolds-averaging. Note that the term “Reynolds-averaged Navier-Stokes” (RANS) is commonly used to describe solvers using either type of averaging procedure. In Favre averaging, each dependent variable is decomposed into

a mass-weighted average component and a fluctuating component. In this manuscript, upper-case is used to denote the mass-weighted average value, and lower-case indicates the fluctuating component (for example, $\tilde{u}_i = U_i + u_i$). The exception is temperature, which uses a double-prime superscript for the fluctuating component to avoid confusion with time ($\tilde{T} = T + T''$). The mass-weighted averaging is defined by the following equation for an arbitrary variable.

$$\Phi = \lim_{\Delta t \to \infty} \frac{\int_{t_0}^{t_0+\Delta t} \tilde{\rho}\tilde{\phi} dt}{\int_{t_0}^{t_0+\Delta t} \tilde{\rho} dt} \tag{4.8}$$

A time average is denoted by an overbar:

$$\overline{\tilde{\phi}} = \lim_{\Delta t \to \infty} \frac{\int_{t_0}^{t_0+\Delta t} \tilde{\phi} dt}{\Delta t} \tag{4.9}$$

The instantaneous density and pressure can decomposed into their time-averaged values and their fluctuating values (denoted by a single prime superscript): $\tilde{\rho} = \overline{\rho} + \rho'$ and $\tilde{p} = \overline{p} + p'$.

The mass-weighted averaged forms of the governing equations are given below for continuity, momentum, and energy, respectively:

$$\frac{\partial \overline{\rho}}{\partial t} + \frac{\partial}{\partial x_j}\left(\overline{\rho} U_j\right) = 0 \tag{4.10}$$

$$\frac{\partial\left(\overline{\rho} U_i\right)}{\partial t} + \frac{\partial}{\partial x_j}\left(\overline{\rho} U_i U_j\right) = -\frac{\partial \overline{p}}{\partial x_i} + \frac{\partial \overline{\tilde{\tau}}_{ij}}{\partial x_j} - \frac{\partial}{\partial x_j}\left(\overline{\tilde{\rho} u_i u_j}\right) \tag{4.11}$$

$$\frac{\partial\left(\overline{\rho} E_0\right)}{\partial t} + \frac{\partial}{\partial x_j}\left(\overline{\rho} U_j H_0\right) = \frac{\partial \overline{\tilde{q}}_j}{\partial x_j} + \frac{\partial}{\partial x_j}\left(U_i \overline{\tilde{\tau}}_{ij}\right) + \frac{\partial}{\partial x_j}\left(\overline{u_i \tilde{\tau}_{ij}}\right) - \frac{\partial}{\partial x_j}\left(\overline{\tilde{\rho} u_j h_0}\right) \tag{4.12}$$

The averaged total enthalpy is defined by:

$$\overline{\rho} H_0 = \overline{\rho} E_0 + \overline{p} = \overline{\rho} c_p T + \frac{\overline{\rho} U_i U_i}{2} + \frac{\overline{\widetilde{\rho} u_i u_i}}{2} \tag{4.13}$$

The above definition of averaged total enthalpy may be used to expand the first term on the right-hand-side of equation 4.12 as shown below.

$$-\frac{\partial}{\partial x_j}\left(\overline{\widetilde{\rho} u_j h_0}\right) = -\frac{\partial}{\partial x_j}\left(c_p \overline{\widetilde{\rho} u_j T''} + U_i \overline{\widetilde{\rho} u_i u_j} + \frac{\overline{\widetilde{\rho} u_i u_i u_j}}{2} \right) \tag{4.14}$$

The time-averaged viscous stress tensor and heat flux vector are given by:

$$\overline{\overline{\tau}}_{ij} = \mu\left[\left(\frac{\partial U_i}{\partial x_j} + \frac{\partial U_j}{\partial x_i}\right) - \frac{2}{3}\delta_{ij}\frac{\partial U_k}{\partial x_k}\right] + \left[\left(\frac{\partial \overline{u}_i}{\partial x_j} + \frac{\partial \overline{u}_j}{\partial x_i}\right) - \frac{2}{3}\delta_{ij}\frac{\partial \overline{u}_k}{\partial x_k}\right] \tag{4.15}$$

$$\overline{\overline{q}}_j = -k_c \frac{\partial \overline{\overline{T}}}{\partial x_j} = -k_c \frac{\partial T}{\partial x_j} - k_c \frac{\partial \overline{T''}}{\partial x_j} \tag{4.16}$$

Finally, the time-averaged ideal gas equation of state is:

$$\overline{p} = \overline{\rho} R T \tag{4.17}$$

Equations 4.10 through 4.17 are the set of governing equations that are solved computationally for all simulations in the present work. Note that in cases in which changes in density are small, the equations may be simplified by assuming incompressibility. Also, for incompressible problems without heat transfer (isothermal), the energy equation is not needed.

The averaging process has created the following new unknowns that must be modeled in order to "close" the system of equations: $\overline{\widetilde{\rho} u_i u_j}$, $U_i \overline{\widetilde{\tau}_{ij}}$, $\overline{u_i \widetilde{\tau}_{ij}}$, $\overline{u_i}$, $\overline{T''}$, $\overline{\widetilde{\rho} u_j T''}$, and $\overline{\widetilde{\rho} u_i u_i u_j}$. Note that the scalar term $\overline{\widetilde{\rho} u_i u_i}$ in Equation 4.13 is the trace of the tensor $\overline{\widetilde{\rho} u_i u_j}$, and therefore it is not in itself an additional unknown. The unknowns $\overline{u_i}$

and $\overline{T''}$ are averages of the fluctuating components and are negligible based on an order-of-magnitude analysis. The time-averaged viscous stress tensor and heat flux vector may then be simplified as follows:

$$\bar{\bar{\tau}}_{ij} = \mu\left[\left(\frac{\partial U_i}{\partial x_j} + \frac{\partial U_j}{\partial x_i}\right) - \frac{2}{3}\delta_{ij}\frac{\partial U_k}{\partial x_k}\right] \tag{4.18}$$

$$\bar{\bar{q}}_j = -k_c\frac{\partial \bar{\bar{T}}}{\partial x_j} = -k_c\frac{\partial T}{\partial x_j} \tag{4.19}$$

Similarly, the terms $U_i\overline{\tilde{\tau}_{ij}}$ and $\overline{u_i\tilde{\tau}_{ij}}$ may be simplified. The remaining unknowns are the turbulent stress tensor, $\overline{\tilde{\rho}u_iu_j}$, the turbulent heat flux vector, $\overline{\tilde{\rho}u_jT''}$, and the triple-correlation, $\overline{\tilde{\rho}u_iu_iu_j}$. These three terms must be modeled, and some general approaches are discussed in the next chapter.

Solution Process

The discretization process casts the averaged governing equations, which are non-linear, partial differential equations, into a set of algebraic equations for each discrete grid point. All derivatives are constructed with second-order numerical approximations, resulting in a second-order-accurate discretization scheme. Upwinding is used for the convective terms, meaning that velocity information at the cell boundaries comes from the adjacent node on the upwind side of a specific node. The multi-purpose, commercially-available Fluent 6 code from Fluent, Inc is used to solve the numerical problem. The solver employs a pressure-correction routine, based on the SIMPLE (Semi-Implicit Method for Pressure-Linked Equations) algorithm of Patankar (1980), to

physically couple the pressure and velocity fields. A dynamic multigrid convergence accelerator is also used for greater efficiency.

In the solid zones of the conjugate simulations, only the Fourier equation of heat diffusion equation is solved. Thermal conductivity is temperature-dependent. At the fluid-solid interfaces, an energy balance condition is imposed. In practice, there are at least two different methods for implementing the fluid-solid interface coupling (energy balance) in the solver, although Fluent 6 has one default method. Optimization of the interface coupling is discussed in the following chapter about the specifics of the conjugate heat transfer simulations.

Solution convergence means that the results are essentially constant from iteration to iteration, and verifying this is a critical step to achieving accurate results. Convergence is declared on the basis of the following strict criteria: (i) residuals of the governing equations, normalized by their respective inlet fluxes, fall below 0.1%; (ii) global mass and energy imbalances drop below 0.01%; (iii) the flow field is unchanging, based on observation of profiles of velocity, pressure, temperature, and turbulence quantities in critical areas; and (iv) predicted surface quantities, such as heat transfer coefficient in the ribbed channel and wall temperature for the conjugate turbine vane, are constant with additional iterations. “Constant” in this case is typically defined by a change of less than one percent at any location in the domain after several hundred additional iterations.

A final solution is reached only after grid-independence is established. This step ensures that the numerical grid does not artificially influence the result. The grid is refined in areas of large gradients of the primary variables (velocity magnitude, temperature, pressure, turbulent kinetic energy, and turbulence dissipation rate), such that

the cell count typically increases by about 20 percent for each refinement cycle. This is an efficient method of focusing the grid adaption at the critical zones where grid resolution has the greatest chance of influencing the results. The refinement process uses a hanging-node adaption technique, in which each smaller cell retains the shape, aspect ratio, and quality of the original cell. A converged solution is then obtained with the adapted grid. The solution is defined to be grid-independent when no variables in the domain change by more than two percent from the converged results obtained prior to grid refinement. Because of the high quality and resolution of the original grids in this work, more than two grid-refinement cycles are rare, and often the background mesh produces grid-independent results.

Several unsteady (URANS) simulations are to be conducted in the present study for flow and heat transfer in ribbed passages. A time step must be determined for URANS, and the choice of time step affects the minimum frequency that can be resolved in the flow. It is based on experimental data for known shedding frequencies (time scales) for these flows, such that there are at least five temporal solutions within each of the shortest periods of the unsteadiness. This is verified by monitoring variable fluctuations at critical points during the solution process. Convergence within an individual time step was achieved by using an appropriate combination of time step size and number of iterations per time step. Typically, because of the small time step size selected, 10 iterations per time step is adequate, and the residuals of the governing equations stabilized in each step.

Due to the nature of the unsteady simulations, convergence and grid-independence are monitored with slightly different criteria than for the steady cases. A

supplementary code (“user-defined function”) was created to interface with the Fluent solver and calculate a running time average of each primary variable at every node in the domain. Since the instantaneous quantities are always changing in the unsteady regions, the time-averaged data must be examined for constancy in order to declare convergence. Also, grid refinement cannot be effectively be performed by adapting cells in areas of large gradients, because these regions naturally change with time in unsteady flows. Instead, the author has found that a particularly effective method of marking cells for adaption is to refine cells based on high values of a dimensionless refinement parameter, $R = \omega l / V$, where l is the normal distance of the grid point from the nearest wall. This targets the cells in the unsteady detached shear layers, but not in the stable boundary layers. Experience has shown that unsteady simulations are much more dependent on the grid size than steady simulations, and multiple refinements resulting in large increases in cell count are not uncommon.

CHAPTER 5

TURBULENCE MODELING OVERVIEW

When all of the components of the numerical process discussed in the previous chapter are handled with prudence, the quality of the simulation results is at the liability of the turbulence model. Turbulence is a stochastic phenomenon that is not fully understood, and, therefore, effective modeling of turbulence is a difficult task. Turbulence modeling is an active research area, with new methods being proposed every year. Yet many of the simpler, time-tested models continue to serve as the workhorses in industry. Because of the importance of turbulence modeling in the present work, it is worthwhile to devote a chapter to overview the major modeling approaches and to lay the foundation for the model development effort that forms a portion of this work.

General Modeling Approaches

Recall that the last term on the right-hand side of Equation 4.11 is a new term resulting from the time-averaging process on the momentum equation. It is the gradient of the turbulent, or Reynolds, stress tensor, $\overline{\tilde{\rho} u_i u_j}$, and the term represents all effects of turbulence on the mean flow, specifically the mean transport of fluctuating momentum by turbulent velocity fluctuations. The Reynolds-stress tensor is a symmetric tensor, and it contains six unknown components (three turbulent normal stresses and three shearing stresses). As discussed previously, the addition of the Reynolds-stress term means that the equations are no longer closed, meaning that is there are now more unknowns

(turbulent stresses) than equations. It is the job of a turbulence model to approximate the Reynolds-stresses in order to solve the system of equations.

There are two general approaches to closing the RANS equations. The first category is the Reynolds stress model (RSM), and this involves solving equations to obtain the turbulent stresses, which are then used directly in the averaged momentum equations. In the full, differential RSM, exact transport equations (partial differential equations) are derived for each of the six independent components of the turbulent stress tensor. After time-averaging, several terms in these transport equations must be approximated, as they contain unknown correlations of fluctuating pressure, velocities, and velocity gradients.

In practice, the RSM involves seven equations, as a length-scale determining equation is also solved. Because of the numerous additional transport equations, differential Reynolds stress models are very computationally intense, often tripling the run-time over a comparable laminar-flow simulation. Also, the transport equations for the stresses tend to be numerically stiff, and solution divergence is common, as seen in many years of work with three-dimensional turbulent flow simulations in the ACRL.

A less expensive route is the algebraic Reynolds stress model (ASM), in which a nonlinear constitutive relationship is developed between the turbulent stresses and the mean strain rate. This approach requires a much greater degree of approximation than the differential RSM, but avoids the need for computationally-costly transport equations for the individual stresses. Yet the well-known numerical stiffness found with differential RSM does not go away fully in the simpler ASM approach. It should be noted that often

simpler one- and two-equation models in the class discussed below have their roots in an explicit ASM derivation.

The second major category of turbulence closure methods includes all models that employ the Boussinesq assumption of 1877, which relates the Reynolds stress tensor to the mean strain rate tensor through a "turbulent" or "eddy" viscosity, μ_T. The Boussinesq assumption (also called the Boussinesq hypothesis) may be written as:

$$-\overline{\tilde{\rho} u_i u_j} = 2\mu_T S_{ij} - \frac{2}{3}\delta_{ij}\left(\mu_T \frac{\partial U_k}{\partial x_k} + \overline{\rho} k\right) \tag{5.1}$$

The left hand side of above expression, the turbulent stress tensor, is related to the mean rate of strain tensor and the turbulent kinetic energy, as defined in Equations 5.2 and 5.3, respectively.

$$S_{ij} = \frac{1}{2}\left(\frac{\partial U_i}{\partial x_j} + \frac{\partial U_j}{\partial x_i}\right) \tag{5.2}$$

$$\overline{\rho} k = \frac{1}{2}\overline{\tilde{\rho} u_i u_i} \tag{5.3}$$

By analogy with the kinetic theory of gases, which gives a good estimate for molecular viscosity, the turbulent viscosity is approximated by

$$\mu_T = \rho v_T l_T \tag{5.4}$$

where v_T and l_T are characteristic velocity and length scales of the turbulence, respectively.

A turbulence model which is based on the Boussinesq assumption is commonly termed an "eddy-viscosity model" (EVM), and is classified by the number of transport equations solved. Zero-equation models are the simplest of all turbulence models, and

they employ a simple algebraic relationship for μ_T. The length and velocity scale approximations in the turbulent viscosity expression are optimized for specific classes of flows (i.e. boundary layer flow, channel flow, separated shear layers, etc.), meaning that zero-equation models are not universally suitable. Also, zero-equation models do not account for the convection and diffusion of turbulence. This shortcoming is resolved by one-equation models, which solve a single partial differential equation for the turbulent velocity scale in Equation 4.6 and use a correlation for the length scale. Typically, the transport equation is for the turbulent kinetic energy. While they perform slightly better than zero-equation models for most problems, one-equation models fall short in situations where the length scales of turbulence vary, including all of the cases in the present study.

The two-equation eddy-viscosity model has become the workhorse of RANS-based CFD due to its compromise between physical accuracy and economy. In addition to the *k*-equation, there is a transport equation for some length-scale determining parameter, and typically this is the dissipation rate of turbulence, ε, or the specific dissipation rate, $\omega=\varepsilon/k$. The eddy-viscosity is computed via the following formulas, where $C_{\mu 1}$ and $C_{\mu 2}$ are constants.

$$\mu_T = C_{\mu 1}\rho\frac{k^2}{\varepsilon} = C_{\mu 2}\rho\frac{k}{\omega} \tag{5.5}$$

The Launder and Spalding (1972) version of the *k*-ε model is considered the “standard”, and is arguably the most popular and well-known two-equation model. Nearly identical results may be obtained with the *k*-ω model of Wilcox (1988).

The exact form of the transport equation for the turbulent kinetic energy may be obtained by first multiplying equation 4.2 by $\tilde{u}_i$ and time-averaging, then multiplying

equation 4.11 by U_i , and finally subtracting the second from the first expression. The result is given below:

$$\frac{\partial(\overline{\rho}k)}{\partial t}+\frac{\partial}{\partial x_j}\left(\overline{\rho}U_j k\right)= \\ -\frac{\partial}{\partial x_j}\left(\frac{1}{2}\overline{\widetilde{\rho}u_i u_i u_j}\right)-\frac{\partial}{\partial x_j}\left(\overline{p'u_j}\right)-\overline{\widetilde{\rho}u_i u_j}\frac{\partial U_i}{\partial x_j}-\overline{\tau_{ij}\frac{\partial u_i}{\partial x_j}}+\frac{\partial}{\partial x_j}\left(\overline{u_i\tau_{ij}}\right) \tag{5.6}$$

The first term on the right-hand side of the above equation is the transport of turbulent kinetic energy by turbulent velocity fluctuations. Pressure-gradient work is represented by the second term. The third term is the production of turbulent kinetic energy by the mean strain, and this is the only exact term that does not require modeling. The fourth term represents the viscous dissipation of *k*, typically denoted by the symbol ε, and is obtained through the solution of a separate transport equation. Transport of turbulent kinetic energy by viscous stresses is the fifth and final term.

The modeled forms of the transport equations for *k* and ε are given by equations 5.7 and 5.8, respectively.

$$\frac{\partial(\overline{\rho}k)}{\partial t}+\frac{\partial}{\partial x_j}\left(\overline{\rho}U_j k\right)=P^k-\varepsilon+D_T^k+D_L^k \tag{5.7}$$

$$\frac{\partial(\overline{\rho}\varepsilon)}{\partial t}+\frac{\partial}{\partial x_j}\left(\overline{\rho}U_j \varepsilon\right)=C_{\varepsilon 1}P^k\frac{\varepsilon}{k}-C_{\varepsilon 2}\frac{\varepsilon^2}{k}+D_T^\varepsilon+D_L^\varepsilon \tag{5.8}$$

The transport terms in the above equations (denoted by the symbol *D*) are modeled algebraically. Molecular transport is modeled as viscous diffusion:

$$D_L^k=\frac{\partial}{\partial x_j}\left(\mu\frac{\partial k}{\partial x_j}\right) \tag{5.9}$$

$$D_L^\varepsilon=\frac{\partial}{\partial x_j}\left(\mu\frac{\partial \varepsilon}{\partial x_j}\right) \tag{5.10}$$

Transport by turbulence is modeled by a gradient hypothesis and typically assuming isotropic mixing:

$$D_T^k = \frac{\partial}{\partial x_j}\left(\frac{C}{\sigma_k}\overline{\rho}\frac{k^2}{\varepsilon}\frac{\partial k}{\partial x_j}\right) \tag{5.11}$$

$$D_T^\varepsilon = \frac{\partial}{\partial x_j}\left(\frac{C}{\sigma_\varepsilon}\overline{\rho}\frac{k^2}{\varepsilon}\frac{\partial \varepsilon}{\partial x_j}\right) \tag{5.12}$$

The above modeling represents a general approach to modeling the components of the Reynolds-stress tensor for an isothermal, incompressible flow. Minor modifications must be made for a compressible flow. For example, Sarkar and Balakrishnan (1990) recommend adding to the left side of equation 5.7 a compressible dissipation term,

$$Y_M = 2\overline{\rho}Ma_T^2\varepsilon \tag{5.9}$$

Where $Ma_T = \sqrt{k}/a$ is the turbulent Mach number, and *a* is the acoustic wave speed. For non-isothermal flows, the turbulent heat flux vector components must also be modeled. Typically, a gradient diffusion approximation is used, and for isotropic models, the turbulent heat flux is given by:

$$\widetilde{\overline{\rho u_i T}} = \frac{C}{\mathrm{Pr}_T}\overline{\rho}\frac{k^2}{\varepsilon}\frac{\partial T}{\partial x_i} \tag{5.10}$$

Like all basic eddy-viscosity models, the *k*-ε and *k*-ω models enforce isotropy of the turbulent stresses through the Boussinesq assumption, which can lead to some difficulties in predicting flows with preferred directions of turbulent fluctuations, or anisotropy. Additionally, the basic models do not meet the realizability constraints for the

turbulent stresses, namely the positivity of normal stresses and Schwarz's inequality for the shear stresses, expressed mathematically as:

$$\left|\overline{u'_\alpha u'_\beta}\right| \le \sqrt{\overline{u'^2_\alpha} \cdot \overline{u'^2_\beta}} \tag{5.11}$$

The lack of realizability may lead to artificially large production of turbulent kinetic energy in regions of rapid, irrotational strain. In an effort to remedy this problem, Shih et al. (1995) developed a realizable *k*-ε (RKE) model that employs a function in place of the constant $C_{\mu 1}$ in the calculation of μ_T (equation 5.5). Another modified version is the Renormalization-group (RNG) *k*-ε model of Yakhot and Orszag (1986). It was developed through a rigorous mathematical analysis of interactions across the scales of turbulence and results in new terms in the transport equations.

Modeling Turbulence Near Walls

Another aspect of turbulence modeling involves the treatment of the near-wall region. The turbulent boundary layer profile exhibits a universal character that is shown in Figure 5.1. Here, the local streamwise velocity, *u*, is normalized by the friction velocity, $u^* = \sqrt{\tau_w / \rho}$, and plotted as a function of the nondimensional wall distance, $y^+ = yu^* / \nu$. The region very close to the wall is the viscous sublayer, where the "law of the wall" holds, and a buffer zone links the sublayer to the "logarithmic layer." The cheapest computational approach to handle the near-wall zone is wall-functions, briefly discussed previously in the grid section in this chapter. Wall-functions include the effect of the wall in a modified boundary condition for the mean flow and turbulence quantities based on the typical turbulent boundary layer profile. The first grid point is normally

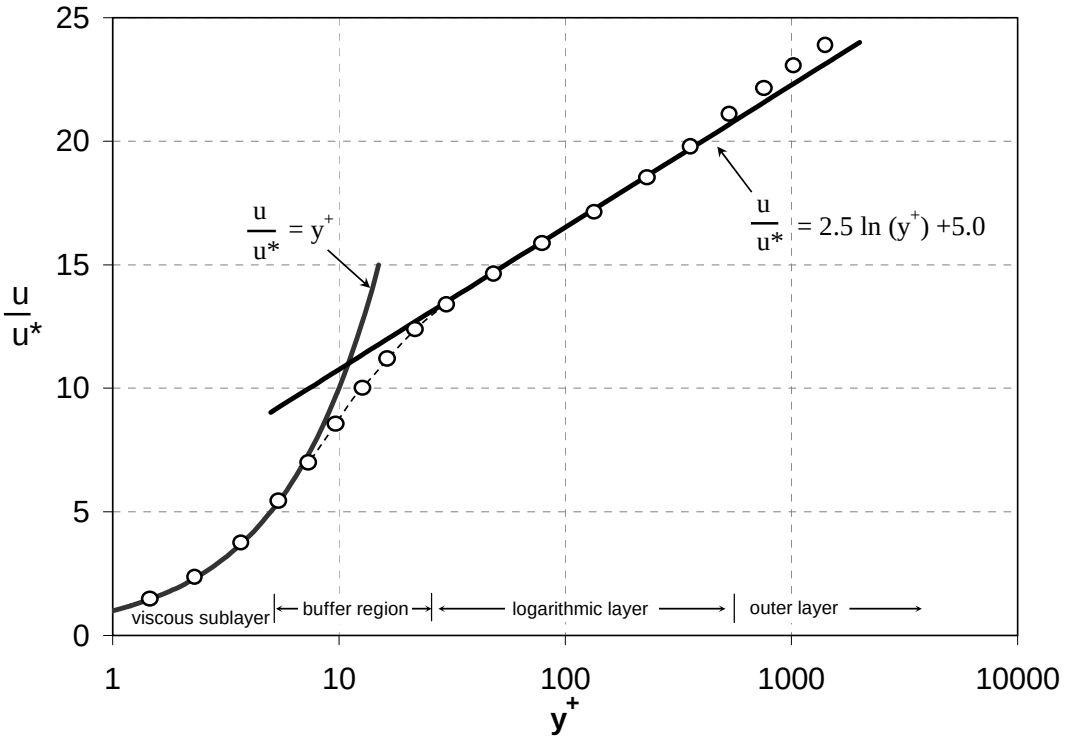

Figure 5.1. The universal turbulent boundary layer profile in wall coordinates showing the different layers. The open circles are approximate measured data from many sources. In the simulations of the present work, the flow is resolved down to the wall, including the viscous sublayer, for superior predictions of heat transfer.

located about y^+=30 (see Figure 4.1(b)). This method has been proven to be ineffective when heat transfer (or wall shear stress) is to be predicted, and in complex turbulent flows, such as recirculating flows involving separation and reattachment.

The more physical near-wall treatments are the sublayer-based methods, which resolve the flowfield all the way to the wall and employ the dense grid of Figure 4.1(a). In this category are the low-Reynolds number (the Reynolds number is that of the turbulence) eddy-viscosity models, which contain damping functions to make them applicable near walls. Another sublayer-based method is the two-layer model, proposed

by Wolfstein (1969). In this approach, a high-Re eddy-viscosity model is solved in an outer region of the boundary layer, and in the inner viscous-affected region, a single transport equation is solved for *k*. The length-scale determining transport equation is replaced in the inner region by an algebraic relation based on wall-distance. The two-layer method is more robust and less computationally expensive than the low-Re models, and testing in the ACRL has proven consistently that the two-layer treatment performs superior to other models, especially when heat transfer predictions are desired. Chen and Patel (1988) also found that the two-layer model performed as well as or better than many of the more complex low-Re models.

Modeling Approach in the Present Work

With advanced modeling, eddy-viscosity models may approach the level of physical realism contained in a Reynolds-stress model, and in some cases the advanced EVM gives superior predictions to RSM. Since numerical instability and cost are significantly less for advanced eddy-viscosity models as compared to RSM, the former are very attractive in a design environment. Therefore, eddy-viscosity models are used exclusively in the present work (except for the occasional RSM case for comparison when a converged solution is achievable). Resolution of the complete turbulent boundary layer, including the viscous sublayer, has been shown to be a critical component in achieving good predictions for heat transfer coefficients. The two-layer near-wall approach combines simplicity and low-cost with good accuracy, and it is used in all simulations of this study.

When suitable, “off-the-shelf” models packaged within the Fluent code are employed. However, in some instances, physics missing in the models becomes an

obstacle to accurate predictive capability. In these cases, efforts are made by researchers in the ACRL, present author included, to improve the modeling. Figure 5.1 shows the relative numerical costs and physical realism associated with the major classes of turbulence models, with the shaded boxes representing the approach herein. The new models developed at Clemson fall into the category of "advanced eddy-viscosity models" since effort has been made for more physics-based models that give better predictive capability.

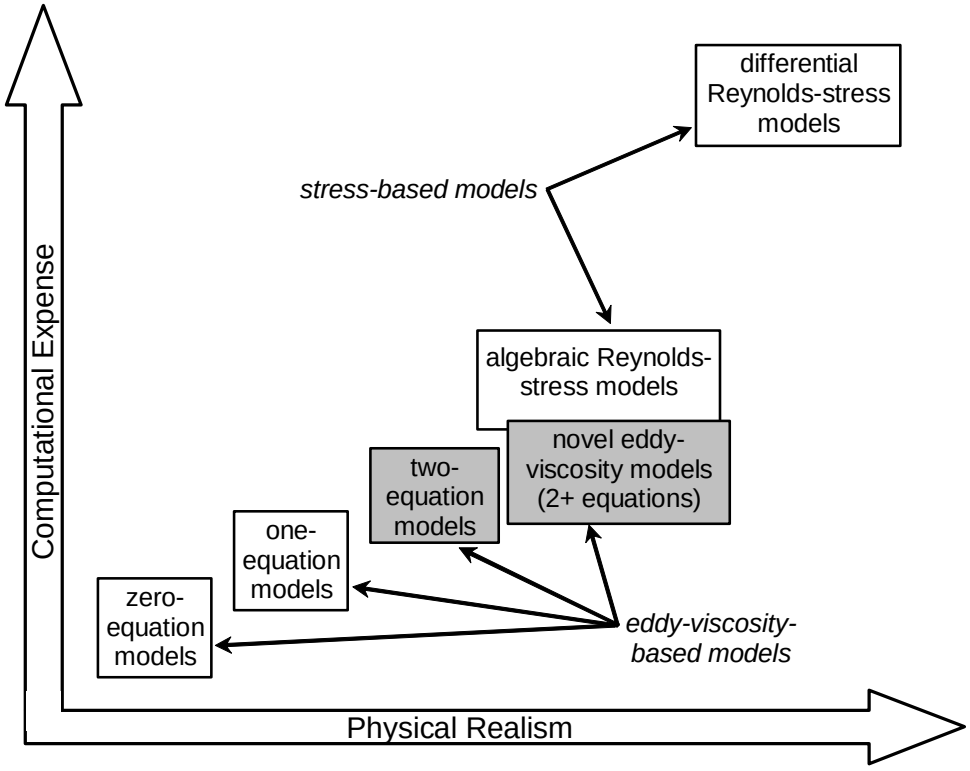

Figure 5.2. Diagram showing the relative physics content and computational expense of RANS turbulence models. The shaded boxes represent the approaches taken in the present study, which prove to be a good compromise between accuracy and cost.

CHAPTER 6

TURBINE VANE CONJUGATE HEAT TRANSFER SIMULATIONS

Conjugate heat transfer (CHT) simulations for an internally-cooled turbine vane at engine-realistic conditions are presented in this chapter. The general methodology detailed in the previous chapter is strictly followed. However, the complexity of the conjugate problem necessitates the inclusion of unique methods, such as efficient grid generation techniques, optimization of the numerical coupling at the zone interfaces, and effective solution initialization. These new "best-practice" methods are designed to be applicable to any turbine airfoil CHT simulation. Results of the validation study are presented at the end of the chapter, and the performance of the methodology is assessed.

Geometry and Conditions

At this early stage of conjugate heat transfer numerical methods development, it is absolutely critical to compare simulation results with measured data from a validation-quality experiment. Unfortunately, as discussed in Chapter 2, conjugate heat transfer experiments (those which purposely include conduction effects in the metal hardware and engine-realistic conditions) are not common in the literature, as the experimental conditions are difficult to create and control in the laboratory. In fact, only a single turbomachinery experiment fits the criteria, and this is the work of Hylton et al. (1983). This study measured wall temperatures for two different turbine vane (stator) configurations at varied, realistic engine operating conditions. The vanes studied were fabricated from stainless steel and were internally cooled by air flowing radially through

ten round cooling holes. Of the two vane configurations, the "C3X" vane was chosen to simulate in the present work because it closely replicates the geometry of a typical forward-stage, high-pressure turbine vane. The C3X vane underwent a decade of various experimental aerodynamics and heat transfer tests at Allison Engines (now Rolls Royce, plc).

The experiment consisted of a linear cascade of three C3X turbine vanes, and the center vane was the one made of stainless steel and internally-cooled. A natural gas burner upstream of the test section created engine-realistic temperatures, turbulence intensities, Mach numbers, and Reynolds numbers. The cooling setup was designed to give a fairly uniform vane external surface temperature, in order to minimize error in the calculation of heat transfer coefficients from the experimental data, and therefore the mass flow rates of air to the individual cooling channels could be controlled.

The present computations employed periodicity conditions to replicate the multiple vane passages in the experiment. All other parameters were copied exactly from the experiment. The C3X vane has a constant cross-section and no twist, and therefore the computer model was created by extruding the two-dimensional geometry through 76.2 millimeters in the spanwise (z-) direction. The vane was digitally created with a spline through points in the *x*-*y* plane supplied by Hylton et al. (1983), and it had a true chord of approximately 140 millimeters. The hot gas passage was bounded by periodic planes, which approximately followed the streamlines in the center of the vane passage, a feature that tends to lead to increased accuracy and stability. For verification, a two-dimensional, adiabatic simulation (aerodynamics-only), with the domain being a slice in the *x*-*y* plane, indicated that very little flow passed through the periodic boundaries in the

vicinity of the vane. The mainstream passage in the computational domain was split nearly in half by the full vane. The periodic planes, separated by 117.73 millimeters in the y-direction, simulated an infinite number of vanes in a linear cascade arrangement. The inlet plane of the computational domain was located one chord length upstream of the vane leading edge, which was the location of turbulence measurements in the experiment. The exit plane of the domain was located more than a chord length from the trailing edge of the airfoil in the direction of the flow (after it had been turned by the vane). The full computational domain is shown in Figure 6.1.

Two mainstream operating conditions were simulated: a subsonic case (Case 1) and a transonic case (Case 2). The two simulations had boundary conditions set to give the exact same conditions as in the experiment. Hylton et al. (1983) reported the average Mach number at a pressure rake located just aft of the vane trailing edge plane at the midspan, and that Mach number was converted to an average static pressure using isentropic flow relations. This experimental value of average pressure was matched in the simulations along that same line near the TE by adjusting the static pressure further downstream at the outlet of the computational domain. Both cases had the same Reynolds number based on true chord of $Re_c=1.9x10^6$. The operating conditions and boundary conditions for the passage for the two simulations are listed in Table 6-1. For both cases, the integral length scale of turbulence at the mainstream inlet was set at 16 millimeters, about 20 percent of the inlet height and characteristic of turbulence from a combustor. Because they varied significantly, the molecular viscosity and thermal conductivity of air were taken to be second-order polynomial functions of temperature, which were acquired

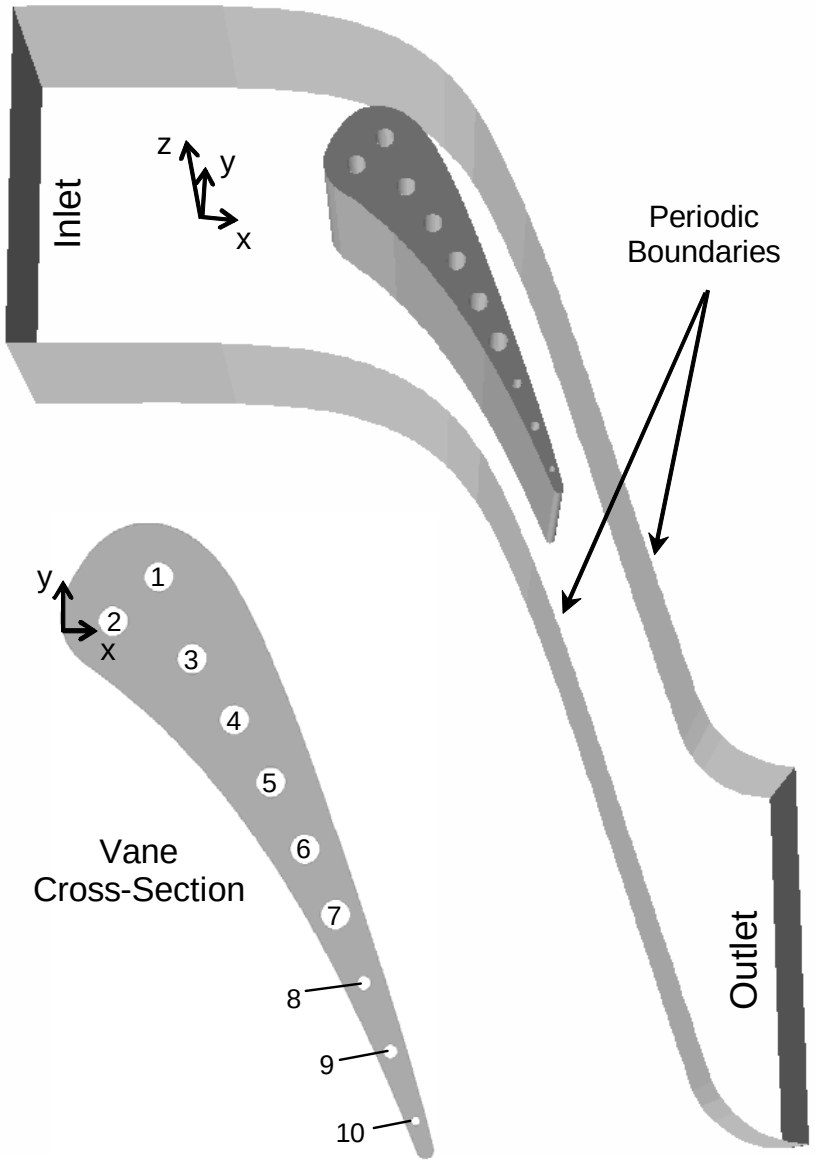

Figure 6.1 Computational domain for the three-dimensional conjugate heat transfer simulations. The transparent boundaries at top and bottom of the domain are solid walls. Periodic planes allow a linear cascade of infinite number of vanes to be simulated. Locations and numbering of the cooling channels are shown in the vane cross-section.

Table 6-1 Conditions of the passage (main) flow for the two simulated cases.

Case	Ma_{LE}	Ma_{TE}	Re	$\dot{m}$ (kg/s)	T_0 (K)	P_0 (bar)	P_e (bar)	TL (%)
1	0.17	0.88	$1.9x10^6$	1.1523	796	3.21	0.885	6.5
2	0.17	1.04	$1.9x10^6$	1.1166	796	3.08	0.508	8.3

through a best-fit of widely-available tabulated data for air at 10°C increments through the range of temperatures of the problem (300K to 800K).

The vane material was 310 stainless steel, which, according to data from Goldsmith et al. (1961), has a nearly constant density of ρ=7900 kg/m^3 and specific heat of C_p=586.15 J/kg-K over the spread of temperatures in this problem. Also based on experimental data from Goldsmith et al. (1961), the thermal conductivity, κ, for the stainless steel vane was specified by the following linear relationship with temperature over the range in the simulations:

$$\kappa = 0.020176\, T + 6.811 \quad [\text{W/m-K}] \tag{6.1}$$

Air at an inlet total temperature of T_c=300K flowed radially through ten cooling channels of circular cross-section. The channels were approximately centered on the camber line of the vane, with the exception of the two holes near the leading edge. The placement and numbering of the cooling holes are shown in Figure 6.1. The diameter of each channel is given in Table 6-2, as is the coolant mass flow rates through the channel, which was different for Case 1 and Case 2. The flow was assumed to be fully developed at the hole inlets at the hub of the vane, as there were long tubes feeding the channels in the experiment of Hylton et al. (1983), and therefore the velocity satisfied the 1/7th power law profile for turbulent flow. Because the channel flow was highly compressible,

Table 6-2 Internal channel diameters and coolant mass flow rates.

Channel Number	1	2	3	4	5	6	7	8	9	10
D (mm)	6.3	6.3	6.3	6.3	6.3	6.3	6.3	3.1	3.1	1.98
Case 1 $\dot{m} \cdot 10^3$ (kg/s)	8.89	7.64	7.28	7.87	7.96	8.12	7.58	2.71	1.66	.822
Case 2 $\dot{m} \cdot 10^3$ (kg/s)	7.71	6.21	6.20	6.58	6.61	6.86	6.36	2.25	1.37	.771

exceeding Ma=0.8 in some channels, it was necessary to prescribe total pressure profiles at the channel inlets instead of velocity. Also, since only the mass flow rates (no pressures) were measured in the experiment, the total pressure profiles had to be adjusted during the run to ensure the flow rates matched. This process involved iterating on the inlet static pressure (constant over the cross-section) and the maximum (centerline) dynamic pressure. The total pressure profile over the inlet may be defined by these two numbers, since dynamic pressure and velocity may be related, and the latter satisfied the $1/7^{th}$ power law. This seemingly tedious profile iteration process was automated as much as possible with computer scripts developed by the author. The inlet turbulence intensity for all channels was 0.2%. The coolant exited the top of the vane to atmospheric pressure.

Grid

General gridding considerations for RANS simulations discussed in Chapter 4 were followed to allow the highest quality in all regions and adequate density for grid-independent solutions. However, conjugate simulations require meshing both fluid and solid zones, sometimes multiples of each type, and therefore some specific grid generation techniques have been developed in this study. The author has found that the

following procedure results in overall best-quality, and is also highly efficient for use in a design setting when rapid turnaround is required.

The gridding procedure for the CHT airfoil problem begins by developing a two-dimensional (2D) grid for a "slice" of the computational domain on the *x*-*y* plane, which is normal to the airfoil spanwise direction (*z*-direction). The quality of the 2D mesh is carried throughout the full domain, and, for that reason, careful attention to maximizing grid quality is needed. The 2D mesh is created with Gambit software from Fluent Inc., and consists of structured and unstructured quadrilateral and triangular cells. Meshing begins with the passage fluid zone. Because of the high Mach number flow in the passage, the boundary layer on the vane is very thin, yet adequate cells must be placed within the boundary layer for full resolution. First the distance from the surface, *y*, of the first grid point is calculated, using the following definition, where y^+ is set at unity:

$$y = \frac{y^+ \nu}{u^*} \tag{6.2}$$

Turbulent flow correlations are used to obtain u^* based on the average of the freestream velocities at the leading edge and at the trailing edge. Between 15 and 20 cells are located in the boundary layer, and the stretching ratio (length of cell divided by length of previous cell) in the wall-normal direction is between 1.25 and 1.4. This fixes the height of the near-wall partition, which is created around the airfoil. The mesh in the wall zone consists completely of structured-type quadrilateral cells. Sizing of cells in the wall-tangent direction is dictated by the necessary resolution and the curvature of the surface. Upstream of the leading edge of the airfoil and in the center of the passage between airfoils, where gradients in the flow are relatively small, cells may be much larger than near the vane surface. This is accomplished with gentle stretching in partitions containing

unstructured triangle and quadrilateral cells. Next the 2D meshing of the cross-sections of the internal cooling passages is completed. In a similar method to the near-wall zone around the airfoil external surface, structured quadrilateral cells are ringed around the channel walls and were stretched toward the centerline and away from the wall. Unstructured triangle cells filled the remaining cross-sections of the channels.

The solid zone is meshed to complete the 2D grid. At the fluid-solid boundaries, the mesh must be conformal, meaning that cells on opposite sides of the boundaries exactly share edges and nodes, and are therefore the same length in the wall-tangent direction. Non-conformal boundaries, where nodes may not line up exactly and cells may be different sizes, creates difficulties in the efficient implementation of the CHT boundary coupling. This means that after gridding the fluid zones, the cell sizing in one direction is already fixed. Because temperature gradients are typically larger near the boundaries with the fluid zones, cells are smaller in the wall-normal direction at the boundaries and are stretched very slightly away from the boundaries. Partitions containing structured-type quadrilateral cells are used along the solid boundaries in the metal, and unstructured quadrilateral cells are used to fill the remaining solid zone. The completed 2D mesh for the C3X vane CHT study is shown in Figure 6.2. From the results of the simulation, a background grid of this density is found to be grid independent (or very close) except when shock waves exist in the flow. In those instances, the hanging-node-based adaptive refinement technique discussed later provides and efficient way to target and resolve the discontinuities.

Creation of the three-dimensional (3D) mesh may be conducted within the Gambit software or with the TGrid program from Fluent, Inc. The author much prefers

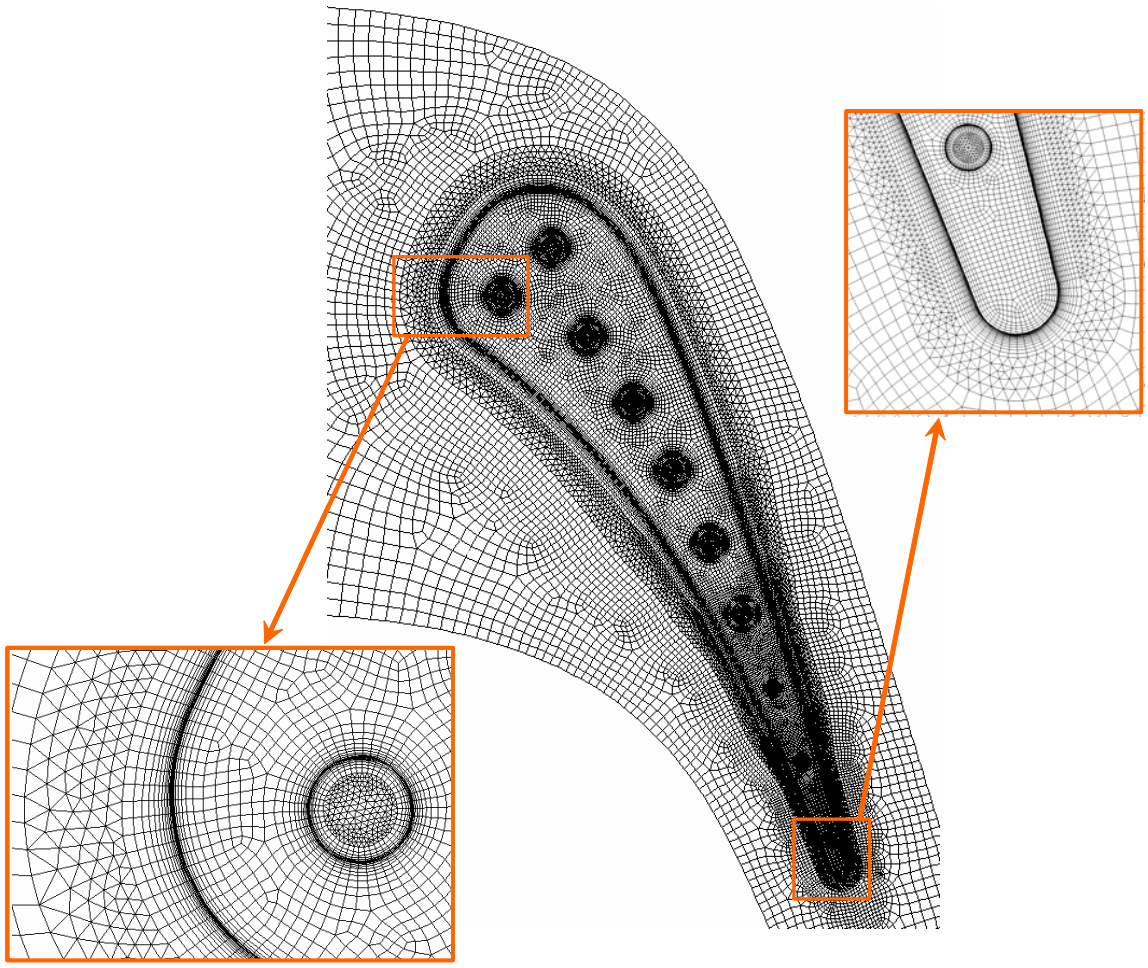

Figure 6.2. View of the computational mesh on any x-y plane showing the high quality and density of the background grid. Close-in views at the leading edge and trailing edge of the airfoil show the very high grid resolution.

the latter for its robustness. The procedure is to grow (in the spanwise, or *z*-, direction) successive layers of prism cells from the 2D mesh, which forms the bottom endwall of the domain. Within each layer, cells are a constant height, and they retain the same quality as the 2D cell they originated from. The resulting 3D grid consists of hexahedra and triangular prism cells. Because boundary layers exist on the endwalls, cell layers are grown in three blocks. In the first block, which is designed to contain the bottom endwall

boundary layer, cells are stretched away from the wall at a ratio of 1.2 to 1.3. In the C3X vane case, because endwall heat transfer was unimportant and in an effort to reduce grid size, the first cell was sized for y^+=50 and wall-functions were applied here. The cells in the middle of the span were sized to give an aspect ratio of approximately unity, meaning their length in the z-direction was the same as in the other two directions. Above the center block, as the top endwall was approached, the procedure for the bottom endwall was mirrored. The reciprocal of the stretching ratio used for the bottom block was applied. The background, or initial, mesh consisted of 6.7 million finite-volumes, with about 56 percent of those cells in the passage, 24 percent in the solid airfoil, and 20 percent in the ten cooling holes.

Fluid-Solid Interface Coupling

The real-time coupling of the fluid zones and the solid zones via energy conservation is at the heart of the CHT methodology. Though simple in concept – energy is conserved across the interfaces – it can be difficult to implement in a numerical code in a stable and efficient manner. With the design environment in mind, two methods were tested for executing the boundary coupling to investigate which would be the most efficient. The first method is simple in concept. After each iteration, the heat flux component normal to the boundary is calculated for the fluid cell and applied directly (same magnitude, opposite sign) to neighboring solid cell across the interface. This process is repeated in reverse when the solid cell variables are calculated. In theory, the heat flux should converge to the "correct" value. This method was accomplished with a User Defined Function (UDF), compiled from code in the C language containing a series of macros allowed by Fluent. This heat-flux-based boundary implementation proved to be

fairly inefficient. The solution became unstable, as the applied heat flux led to large changes in local cell temperatures in the metal, which then caused a reversal of heat flux direction on the next iteration, and so on. Convergence to stable local boundary temperatures was not possible, so a relaxation factor was applied to the heat flux being "sent" across the interface. Only when the relaxation factor was dropped to 0.1, meaning only 10% of the calculated heat flux was being transferred, could a converged solution be achieved. However, this relaxation significantly slowed the overall convergence rate of the simulation.

The second method focuses on specification of the single boundary temperature, shared by the neighboring cells on opposite sides of the boundary. This is the implementation employed within the Fluent code. During each iteration, the boundary temperature is adjusted so that the calculated heat flux on the fluid side will exactly balance the calculated heat flux on the solid side. This boundary-temperature-based implementation proved to be very stable and fairly efficient, even though it requires more calculations per iteration than the previous method. It is the method recommended by the author and adopted for use in the present study. After both methods were tested, it was reassuring to note that they gave exactly the same converged solution for wall temperature.

Solution Initialization

Since an iterative method is used to solve the RANS and energy equations simultaneously, initial values for the primary variables must be prescribed, a process called "initialization". The closeness of the initial conditions to the actual solution directly impacts the speed at which convergence is reached, or if convergence may be

reached at all. For most fluid flow problems dominated by convection-diffusion equations, the relatively short time scale of convection makes the choice of initial conditions somewhat insignificant., as long as the initialization is reasonable and doesn't induce massive instabilities (for example, prescribing a much larger pressure in the domain than the ambient pressure often results in divergence). For the present study, and several other airfoil cascade studies performed by the author, setting velocity components to zero and all other variables in the flow regions to their respective inlet values was sufficient to get a converged solution. "Improving" the initial guess for the fluid zones resulted in no appreciable reduction in number of iterations required.

It may be a different story, however, for heat diffusion in a solid. Even in a steady, implicit simulation, the heat transfer is paced by pseudo-time stepping. The time scale for conduction is much larger than for convection heat transfer, especially at the extremely high velocities studied. A time scale for heat diffusion in the airfoil is given by $t=\rho c L^2/\kappa$, where L is a characteristic length of the airfoil. For this study, this number is about five orders of magnitude larger than a pertinent time for convection, such as L/U, (regardless of the length scale in the flow, L, that is used). For this reason, the conduction is expected to slow down the convergence rate. This was verified in the initial C3X simulations, where the temperature in the metal was initialized to a constant value equal to the average between the passage and coolant total temperatures. Well after the aerothermal field in the fluid zones was essentially unchanging, the temperature field in the metal continued to develop with additional iterations. This does not pose a problem if one or two simulations are run in a benchmark-type study, but the extra iterations can be costly in a design environment.

As part of the effort to build the conjugate heat transfer methodology into a viable tool for industry, a new "enhanced initialization" function for the airfoil temperature field was developed. This new initialization is designed to make the initial "guess" for temperature close to the final converged temperature distribution. The function was written in "C"-code, provided in Appendix A, and is compiled into an "execute-on-demand" function, available to the Fluent user. It was designed to be applicable to any airfoil with radial cooling channels.

The user inputs the geometric properties of the airfoil, including span, internal and external surface areas, and cooling hole centerline coordinates and radii. Also specified are the properties of the hot gas and the coolant at their inlet total temperatures, the Reynolds number (based on chord length) for the external flow, and the mass flow rates for the coolant channels. The function starts by calculating an average heat transfer coefficient for the external flow. Good results were obtained with the following flat plate correlation for turbulent flow using chord length of the vane:

$$\overline{\mathrm{Nu}}_C = 0.037\,\mathrm{Re}_C^{0.8}\,\mathrm{Pr}^{1/3} \tag{6.3}$$

Next the average heat transfer coefficient for the cold side is found by averaging the heat transfer coefficients predicted by Dittus-Boelter correlation for each hole:

$$\overline{\mathrm{Nu}}_D = 0.023\,\mathrm{Re}_D^{0.8}\,\mathrm{Pr}^{0.4} \tag{6.4}$$

It is necessary to approximate the inside and outside temperatures of the vane surface, T_{IW} and T_{OW}, respectively. There are two ways to get this information. First, the user may specify the external wall average temperature directly. This method is useful for the actual design process when the maximum allowable wall temperature is available. The

second method, used in the present study, is to use the measured mass flow rates and fluid exit temperatures for all cooling holes to calculate the total heat flux:

$$q = \sum_1^n \dot{m} c_p \left(T_c - T_e \right) \tag{6.5}$$

With the heat flux known, the wall temperatures may be approximated. The function loops through all cells in the solid and calculates the distance from the cell centroid to the external wall (D_{OW}) and also to the nearest cooling channel wall (D_{IW}). For each cell, the initial temperature, T_i, is a linear function of the two distances:

$$T_i = \frac{T_{OW} D_{IW} + T_{IW} D_{OW}}{D_{IW} + D_{OW}} \tag{6.6}$$

Because the temperature in the metal airfoil will increase in the radial direction as the bulk temperature of the coolant increases, the initial node temperature is also made to be a function of location in the radial direction (centroid *z*-coordinate). A piecewise (two segment) linear increase in initial metal temperature with *z*-direction is applied, and it is based on a percentage increase in the coolant temperature between the same *z*-planes. Figure 6.3 shows the result of executing the enhanced initialization function, with initial temperature contours on planes at three radial locations for Case 1 of the C3X vane simulation.

To test the impact of the new initialization, the C3X simulation was started with the standard (constant metal temperature) initialization and was run until convergence was declared under the strict criteria discussed in Chapter 4. It was then run for 1000 additional iterations, and final temperatures at 25 locations within the metal at various places were recorded. Next the same case was started from the enhanced initialization, and monitors were set up to indicate when temperatures at the 25 locations came to (and

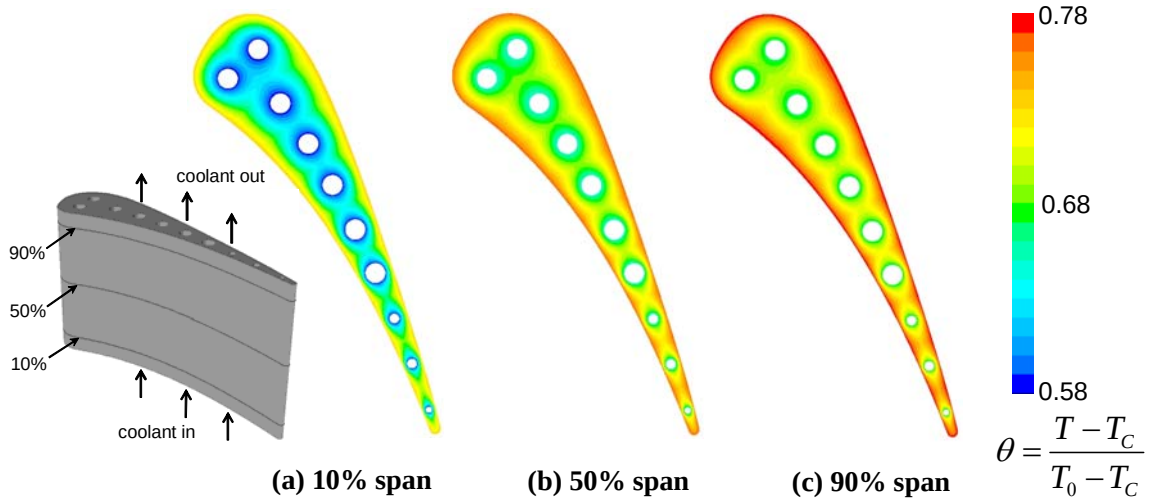

Figure 6.3. The initial metal temperature field using the "enhanced initialization" function on planes located at (a) 10% span, (b) midspan, and (c) 90% span.

remained) within 0.5% of the final values. When the last monitor indicated a temperature within the tolerance, convergence was declared. Using the standard multigrid convergence accelerators in Fluent 6, the enhanced initialization case took 2820 iterations, while the standard initialization required 3100 iterations. The enhanced initialization reduced iterations by almost 9%, a runtime savings of about 90 cpu hours. If no multigrid accelerator is used (or is unavailable, as in some non-commercial codes), the enhanced initialization was found to save up to 40% in computational cost.

Solution Details

The C3X vane conjugate heat transfer simulations initially employed two variants of the popular, two-equation *k*-ε model for comparison purposes- the standard *k*-ε (SKE) model of Launder and Spalding (1972) and the realizable *k*-ε (RKE) turbulence model of Shih et al. (1995). The RKE model reduces the excessive and non-physical production of

turbulent kinetic energy characteristic of the standard k-ε model in areas of rapid, irrotational strain, a condition that occurs, for example, at the stagnation point on the leading edge of a turbine airfoil. Walters and Leylek (2000) documented the superior performance of the RKE model in a simulation of a turbine airfoil cascade. The two-layer near-wall model of Wolfstein (1969) was employed to resolve the flow all the way to the wall. The reader is referred to Chapter 5 for additional details on the turbulence modeling and the near-wall treatment.

The present simulations were run using the Fluent 6 code from Fluent, Inc. In the fluid zones, the steady, time-averaged Navier-Stokes equations were solved, and pressure-velocity coupling was achieved with the SIMPLE algorithm. In the solid zone, only the Fourier equation for heat diffusion was solved. All equations were discretized with second-order accuracy. During the run, the vane passage exit static pressure was sequentially lowered from a value equal to the inlet total pressure to the final exit pressure (to match the experiment) for stability at the high mainstream Mach numbers of this problem.

Convergence of the solution was verified according to the stringent criteria discussed in the Chapter 4. In addition, it was verified that the temperature profiles within the metal and the vane external surface temperature did not change with additional iterations. The simulations were run on 20 parallel processors of a Sun Microsystems Ultra Enterprise 6500 computer with 10 gigabytes of RAM. Each iteration took approximately one minute of wall-clock time.

To establish grid-independence, the grid in the fluid zones was refined in areas of large gradients in the flowfield variables (U, T, p, k, and ε), such that the cell count in

each zone increased by about 20 percent in the refinement cycle. The grid in the solid zone was refined in areas of large temperature gradients to give an increase in cell count of approximately 10 percent. Due to the extremely fine nature of the background grid, the refinement resulted in no appreciable change in any variable for Case 1, and therefore the simulation was declared grid-independent with the original grid. Since a weak discontinuity occurred in the passage in Case 2, the grid in the mainstream zone was also refined in areas of large magnitude of the rate of volume dilatation, Δ, defined as

$$\Delta = \left| \frac{\partial u_i}{\partial x_i} \right| \tag{6.7}$$

The volume dilatation is a good parameter to measure the relative compressibility of the local flow and tends to be greatest in the immediate vicinity of a shock. Marking cells based on this parameter is an efficient way to cluster cells at the discontinuity for better resolution. Two successive refinements, bringing the total cell count to 7.8 million cells, resulted in well-resolved shocks and grid independence in Case 2.

Conjugate Heat Transfer Simulation Results

Results of the conjugate C3X vane simulations are presented and analyzed in this section. Data from Case 1 (subsonic passage flow) and Case 2 (transonic passage flow) are denoted as such. All experimental data presented in this section is from the study of Hylton et al. (1983). For Case 1, results for two turbulence models are given, and the acronyms SKE (for standard k-ε) or RKE (for realizable k-ε) follow the case number.

The predicted aerodynamic loading for Case 1 in the form of pressure distribution at the vane midspan is given in Figure 6.4, along with experimental data. Since loading curves predicted by the two turbulence models were essentially identical, only the RKE

result is plotted. On the suction surface (SS), or the convex side, the pressure falls very rapidly from the stagnation line toward the throat, reaching a minimum value of approximately half of the inlet total pressure by s/L_{SS}=0.25. A mild adverse pressure gradient follows this minimum, and after s/L_{SS}=0.5, a gentle acceleration occurs to the trailing edge. On the pressure surface (PS), or concave side, the pressure stays almost constant at p_0 from the leading edge (LE) to near s/L_{PS}=-0.5 and then falls off with further distance toward the trailing edge (TE). The predictions exhibit excellent agreement with the data of Hylton et al.(1983), validating the aerodynamics portion of the model. The predicted and measured loading curves for Case 2 are plotted in Figure 6.5, and again they match very closely. On the PS, the pressure distribution is nearly identical to Case1. However on the suction side, a weak discontinuity occurs at about s/L_{SS}=0.5. The pressure rises slightly aft of this mild shock, and then decreases with further distance from the LE.

The contours of Mach number on the midspan plane (z=38.1mm) for Case 1 and Case 2 are shown in Figure 6.6. Due to the shape of the airfoil, the flow sees strong acceleration along the suction side near the leading edge. For Case 1, the maximum Mach number in the vane passage is about Ma=0.9, and it occurs at a position just off the SS about 20% of the surface distance from the LE to the TE. Along the pressure surface, the Mach number remains quite low until the aft quarter of the vane, after which rapid acceleration occurs. Notice also that the maximum Mach numbers in some of the cooling channels exceed Ma=0.8, indicating that the internal flow is also highly compressible. In Case 2, the flow expands to a maximum Mach number of about Ma=1.12 along the suction surface. As in Case 1, acceleration on the pressure side in Case 2 is slow until the

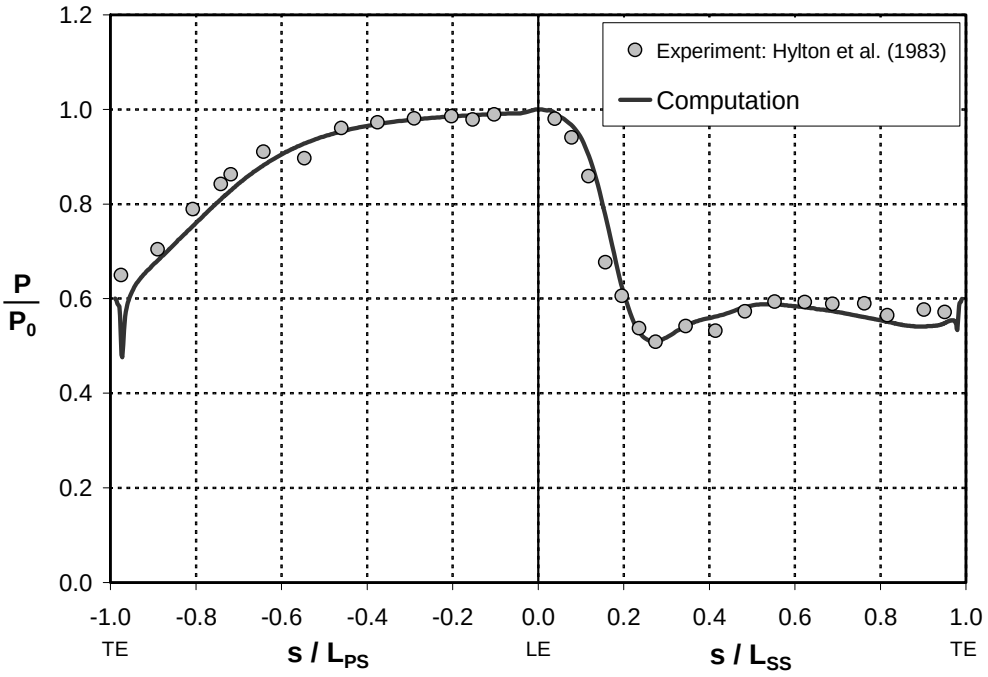

Figure 6.4 Predicted and measured aerodynamic loading (at midspan) for Case 1.

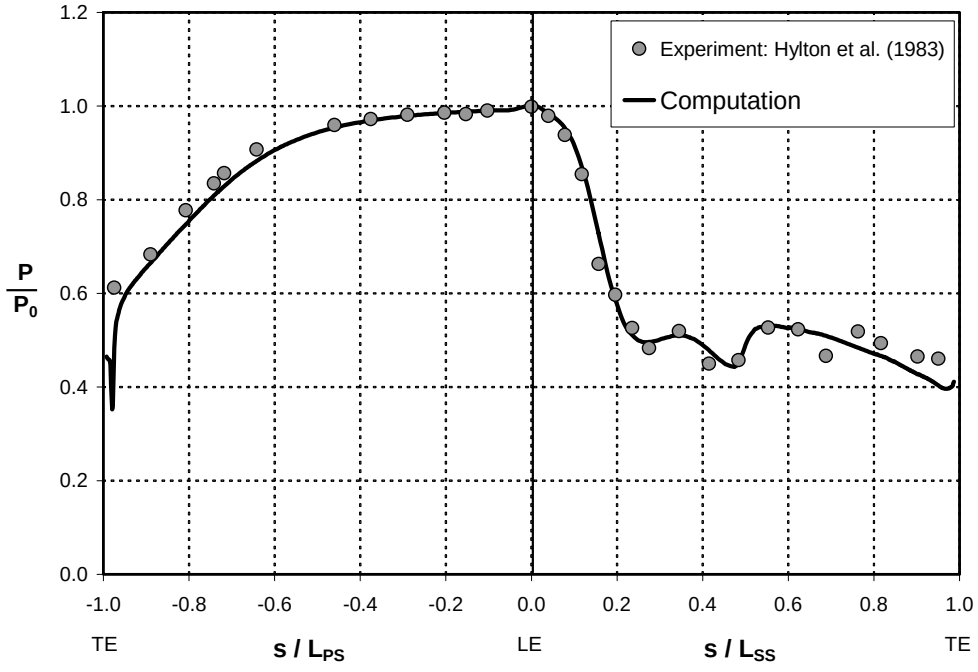

Figure 6.5 Predicted and measured aerodynamic loading (at midspan) for Case 2.

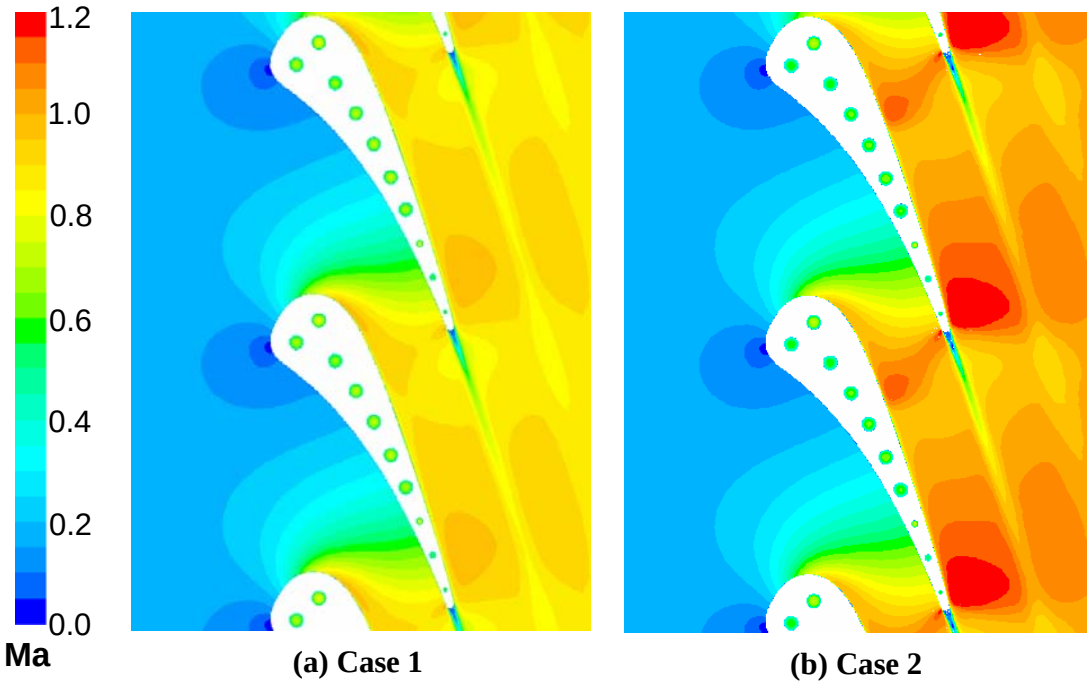

Figure 6.6 Contours of Mach number on the midspan plane for (a) Case 1 and (b) Case 2.

throat is approached near the trailing edge, where supersonic flow exists. A weak discontinuity is seen to cross the passage from about s/L_{SS}=0.5 on the SS to the trailing edge (s/L_{PS}=1) on the PS. On the suction surface, the flow expands again aft of the weak passage shock and a second, stronger oblique shock forms at the TE.

The differences in the performance of the two turbulence models is clearly seen in Figure 6.7, contours of turbulence level on the midspan plane for Case1-SKE and Case1-RKE. The standard k-ε model results in a high production of turbulence kinetic energy at the stagnation point. This is not physically accurate, as the strain at the leading edge is irrotational in nature and therefore should not result in production of k. Also, there is an extremely large turbulence level (TL), approaching 80%, in the region of the vane passage where the rapid acceleration takes place. The realizable version of the model is

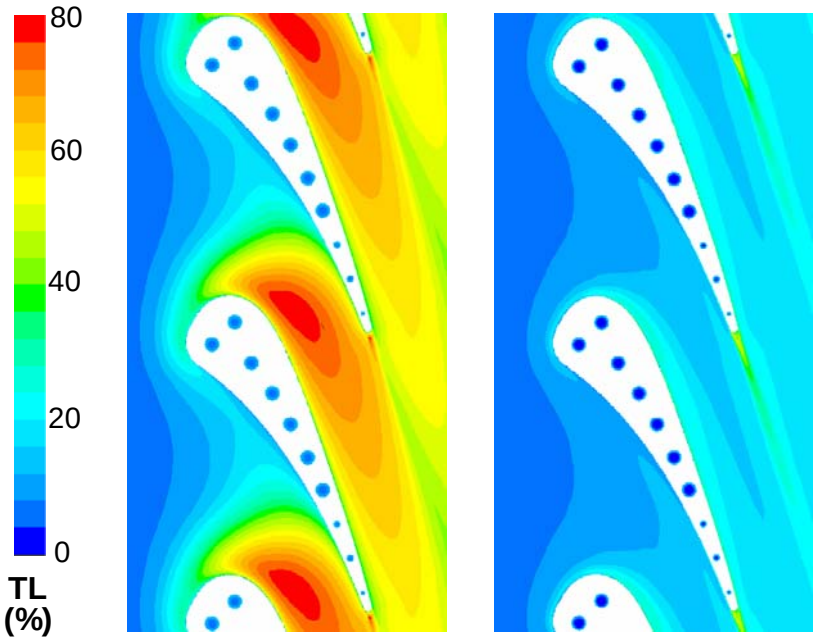

Figure 6.7 Values of turbulence level at the midspan plane for Case 1 with (a) the SKE turbulence model and (b) the RKE model.

seen to eliminate the spurious production of *k* at the leading edge and in the passage. The maximum turbulence level occurs in the airfoil wake for the RKE case. The TL in the vane passage itself peaks at about 20% in the SS boundary layer, which is a more reasonable result. Because of its superior performance, only the RKE model was employed for Case 2.

With the aerodynamics validated, the heat transfer (temperature) results may be investigated. The distribution of the dimensionless temperature,

$$\theta = \frac{T - T_c}{T_0 - T_c} \ , \tag{6.8}$$

on the vane external surface at the midspan is plotted in Figure 6.8 for Case 1. Predictions with both SKE and RKE models are included, along with experimental data. Recall that

the intent of the experiment was to achieve a uniform temperature distribution on the external wall, and in this case the average was approximately θ=0.7. The Case1-RKE result shows generally good agreement with the experiment. All trends in θ are matched by the computation, with the exception of a portion of the curve on the suction side near the LE. Here the predictions show an increase in wall temperature to about θ=0.77 at s/L_{SS}=0.2, while the experimental data actually dips slightly to θ=0.7. This location corresponds exactly to the region of very strong curvature of the airfoil surface (refer to Figure 6.4). It is well-documented that most eddy-viscosity models, including SKE and RKE, are not correctly sensitized to streamline curvature, and this discrepancy in heat transfer could be a result. The convex curvature should have a stabilizing effect on the turbulence field, but the models don't indicate any suppression of TL in the the high-curvature region of the suction surface in Figure 6.7. Excluding this segment of the suction surface, the predictions of θ with the RKE model are within 5 percent of the experimental data over the entire airfoil.

The predictions with the SKE model show a nearly constant positive offset from the RKE model. This must be a result of the much greater (non-physical) turbulence intensity in the freestream around the entire airfoil in the SKE case. The near-wall model is identical in both cases (SKE and RKE), and the value of *k* at the lower edge of the high-Re_T zone is a boundary condition for the wall-adjacent zone. In the SKE case, the elevated turbulence around the entire vane enters the near-wall region, causing the local heat transfer coefficient, and therefore the wall temperature, to increase. The wall temperature plotted in Figure 6.8 is strongly dependent on the local heat transfer coefficient, and, to a lesser extent, the local freestream static temperature.

In addition to the freestreem turbulence intensity, the heat transfer coefficient depends on the local freestream velocity and the condition of the boundary layer. The heat transfer coefficient increases as the freestream accelerates in the passage, as the boundary layers become thinner and resistance to heat transfer across the sublayer decreases. The heat transfer coefficient increases to a very large value on the suction side, and is much higher than on the pressure side where the velocity outside the boundary layer remains much lower. The result is a higher wall temperature on the SS as compared to the PS, as seen in Figure 6.8. On both sides of the vane, the temperature increases as the trailing edge is approached, and the θ curve becomes increasingly "wavy", as the internal cooling channel becomes closer to the outside surface as the metal thickness decreases.

The predicted temperature on the vane external surface at the midspan is plotted along with the experimental data for Case 2 in Figure 6.9. Results indicate a slight overprediction of the temperature over the entire airfoil, but the maximum discrepancy is within 10%. The trends in the predictions match the experiments except for on the near suction side. Here, as in Case 1, the computed temperature increases in this region of high streamline curvature, while the measurements show a small dip. Note also that the numerical results show a small increase in temperature just aft the location of the weak discontinuity on the suction side (s/L_{SS}=0.5). The freestream static temperature increases through the shock. Three-dimensional conduction in the metal is responsible for "smearing" this temperature discontinuity on the surface and lessening the magnitude. The location and effect of the shock is better seen in Figure 6.10, contours of dimensionless temperature are shown on the entire vane external surface for Case 2. The

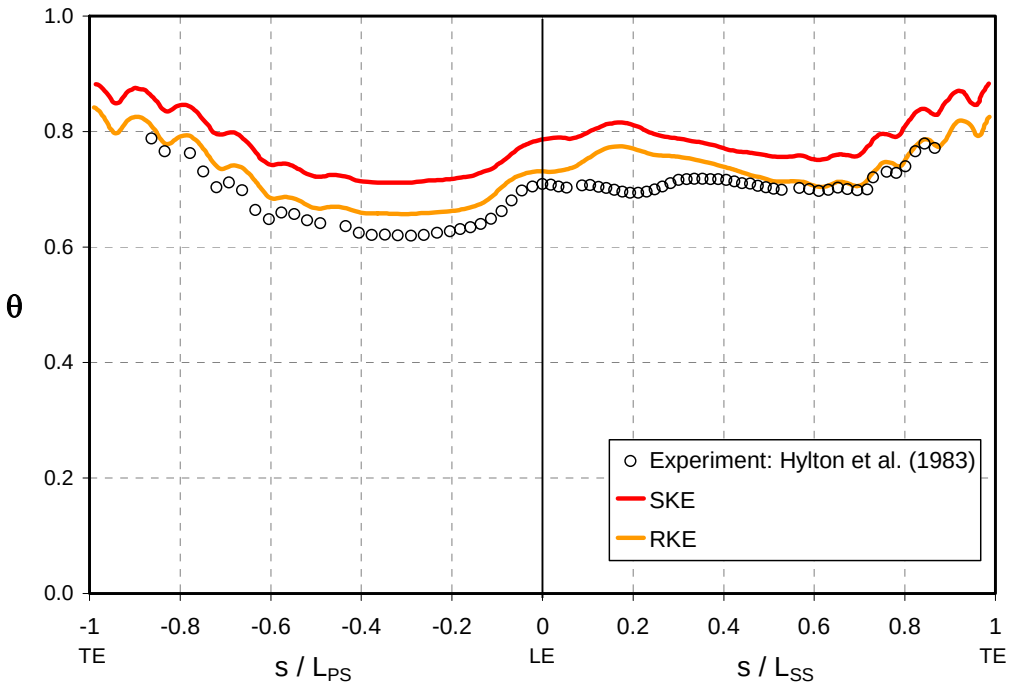

Figure 6.8 Dimensionless temperature at the vane external surface at midspan for Case 1 is plotted as a function of surface arc length fraction (from LE).

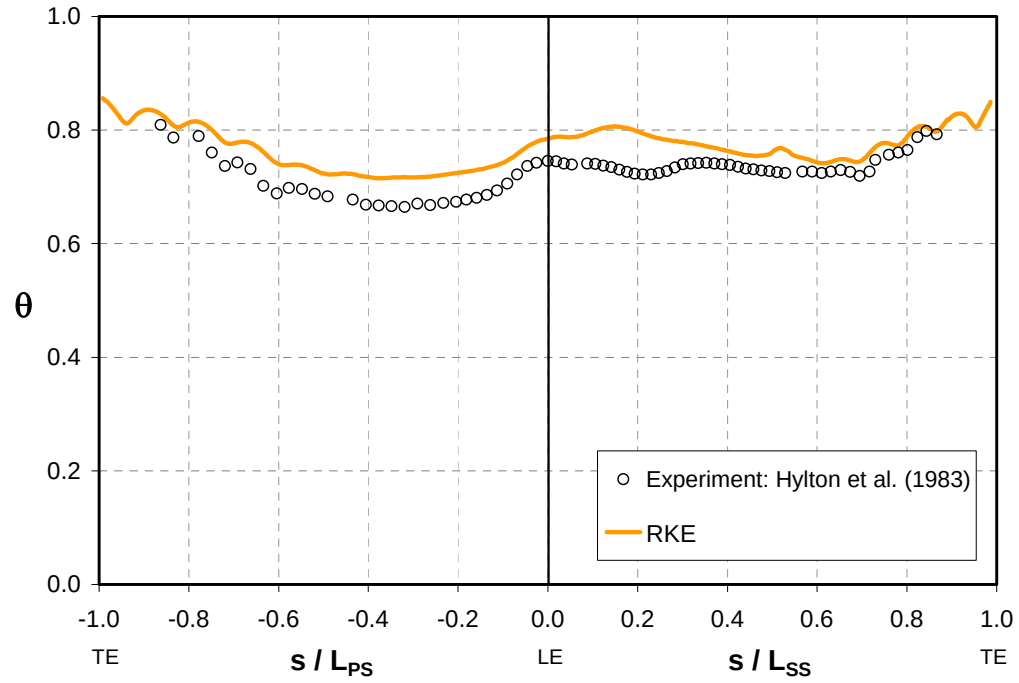

Figure 6.9 Dimensionless temperature at the vane external surface at midspan for Case 2 is plotted versus surface arc length fraction.

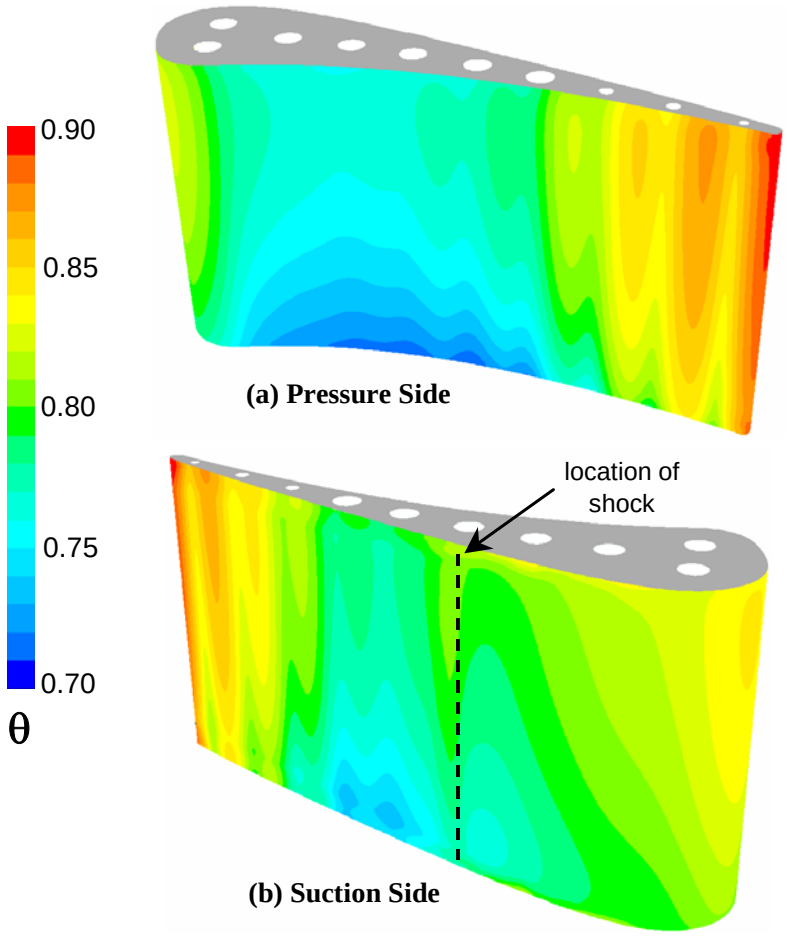

Figure 6.10 Contours of dimensionless temperature on the vane (a) pressure surface and (b) suction surface for Case 2. The location of the shock near the suction surface is denoted, and the effect of the discontinuity on surface temperature is evident.

temperature increases on the suction surface from top to bottom immediately aft of the discontinuity, which is located at the dashed line. Also evident in Figure 6.10 is the large temperature variation near the trailing edge where the cooling channels are very close to the external surface. Temperature gradients, leading to thermal stresses, are large here, and the difficulty involved in adequately cooling the trailing edge region of airfoils is clear.

The temperature distribution within the metal vane for Case 1- RKE is seen in Figure 6.11, contours of θ on three cross-section planes at 10%, 50%, and 90% span. Notice that the patterns of temperature are fairly consistent at the three spanwise locations, but the temperature increases almost linearly with spanwise distance from the hub surface (coolant inlet). This is due to higher coolant temperatures downstream as thermal energy from the mainstream is transferred to the coolant. The metal temperatures are much closer to the mainstream temperature than the coolant temperature in all planes. The maximum metal temperature occurs at the thin trailing edge, and the largest temperature gradients in the chordwise direction are also in this region.

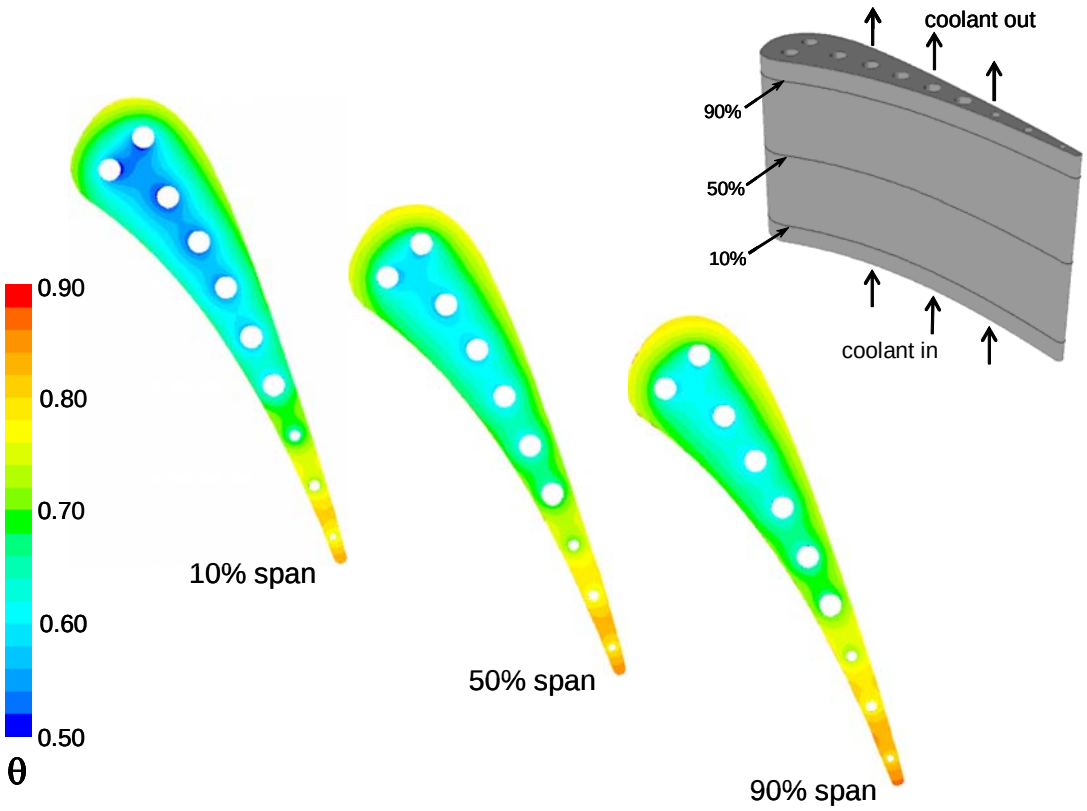

Figure 6.11 Temperature distribution in the metal vane at three planes of constant spanwise coordinate. The ability to pinpoint hotspots and high thermal gradient zones within the airfoil is a great benefit of the conjugate heat transfer method as a design tool.

It is instructive to look at the distribution of temperature on a line through the vane (including a cooling channel) from the freestream on the PS to the SS. The author arbitrarily chose a line through coolant channel 5 at the midspan plane. The dimensionless temperature is plotted versus the distance from the channel centerline in Figure 6.12. The line is nearly normal to the airfoil external walls, as shown in the inset. Notice that the vane outside wall on the SS is very near the freestream temperature, indicating a very small thermal resistance and hence a large heat transfer coefficient. The temperature difference across the pressure-side boundary layer is slightly larger than on the SS due to a greater thermal resistance. The temperature difference in the solid is small, indicating a small thermal resistance. Also, the temperature difference between the inner walls of the channel and the channel freestream is very large, signifying a much greater thermal resistance R_i, or a far smaller heat transfer coefficient, than the external convection. If one-dimensional heat conduction is assumed locally along this normal line, the approximate thermal resistances for the different heat transfer modes may be calculated, and they are listed in Table 6-3. The SS convection and the conduction in the solid have similar resistances, while the resistance of the PS convection is slightly higher. By far the greatest thermal resistance is due to the internal convection. Lower metal temperatures could be achieved by reducing R_i, which is accomplished by increasing the heat transfer coefficient in the channels. This is the reason that ribs on the channel walls are commonly employed to increase turbulence levels.

Table 6-3 Thermal resistances (m^2K/W) across vane at channel 5.

$R_{SS} = \frac{1}{h_{SS}}$	$R_{PS} = \frac{1}{h_{PS}}$	$R_i = \frac{1}{h_i}$	$R_{cond} = \frac{L}{\kappa}$
0.26×10^{-3}	1.06×10^{-3}	2.35×10^{-3}	0.32×10^{-3}

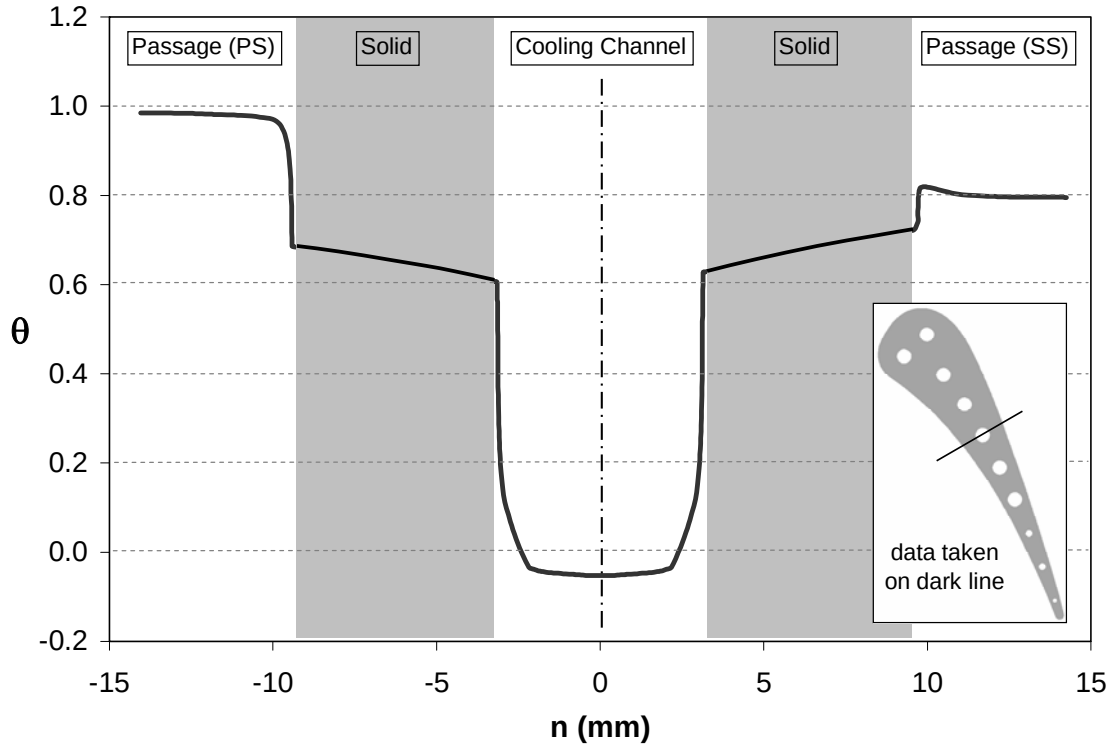

Figure 6.12 Temperature profile along a straight line at midspan cutting through the vane at hole 5 as shown in the inset.

CHAPTER 7

RIBBED CHANNEL HEAT TRANSFER SIMULATIONS

Modern gas turbine airfoils operate in a harsh, high-temperature environment that necessitates innovative cooling schemes, and most forward-stage airfoils contain some form of internal cooling. In some cases (more typically in power-generation gas turbines), the internal cooling may consist of an array of smooth-walled, radially-oriented channels, as in the C3X vane conjugate heat transfer simulation of the previous chapter. The impact of augmenting heat transfer coefficients in the passages to reduce the metal temperatures was shown in the CHT case. Heat transfer augmentation is commonly accomplished by fabricating ribs on the channel walls to increase the turbulence levels (for that reason, ribs are often called “turbulators”).

Extending the conjugate heat transfer methodology to include channels containing ribs is an important step in developing a design tool that is widely applicable to gas turbine hot-section problems. Ideally, experimental validation cases with “active” (in the heat transfer sense) metal airfoils, like the C3X vane study, would exist that include ribbed internal channels. However, an exhaustive search of the literature (and inquiries to industry representatives on the existence of unpublished, in-house data) turned up no such experiments. It is not surprising, since the cost and accuracy of experimental programs typically increase with problem complexity, and, like computations (until recently), heat transfer modes are decoupled and studied separately. Nevertheless, the conjugate heat transfer methodology can be validated for ribbed passages if a careful validation study is carried out separately. From the results of the C3X vane CHT

simulations, the coupling of boundary conditions, heat diffusion in the metal, and external and internal heat transfer coefficients are predicted well. If one can show that heat transfer coefficients for the more complicated case of straight ribbed channels (and later channels with a 180^o turn) can be accurately predicted, then it may be confidently integrated into a CHT simulation.

Ribbed Channel Test Cases

To obtain a fair assessment of predictive capability for heat transfer in ribbed channels, two different test cases were simulated. Test case "A" modeled the experimental conditions of Taslim et al. (1998). This test case consists of a channel of square cross-section with relatively large ribs of rounded edges in a staggered configuration on opposite walls. Because Taslim et al. (1998) did not provide detailed heat transfer measurements (only area-averaged heat transfer between one pair of ribs was available), and to extend the computational methods to varied configurations, a second test case was chosen. This case "B" simulated a wide channel with small square ribs on one wall, matching the experiment of Acharya et al. (1997), for which detailed measurements of the heat transfer coefficient on the ribbed wall were available for validation.

Test Case A was chosen for its realistic application to gas turbine engines, and because a variety of Reynolds numbers were studied by Taslim et al. (1998). The square channel cross-section was 177.3 centimeters long with a height and width of 7.62 centimeters. The channel was roughened on two opposite walls with ribs that were orthogonal to the flow and spanned the entire width of the channel. There were nine ribs on each of the two walls, and ribs on opposite walls were staggered. The two side walls

were smooth. Each square rib had a height and width, *h*, of 1.661 cm. The corners of the ribs were rounded with a radius of 0.317 centimeters, and the pitch of each rib, *S*, from center to center was 8.5*h*. A cross-sectional view of a portion of the computational domain, including the inlet and exit, is shown in Figure 7.1.

A constant heat flux of q"=125 W/m^2 was applied to the entire length of the bottom wall excluding the rib surfaces. This also matched the experiment, which employed a liquid crystal technique to obtain the area-averaged heat transfer coefficient between the fifth and sixth ribs on the bottom wall. At the inlet, air at a temperature of 300 K was specified to have a uniform velocity, which was varied to match the Reynolds numbers of the experiment. The air exited the channel to atmospheric pressure.

To create the computational grid, a two-dimensional (2D) grid was first created on a plane of constant lateral (z-) coordinate. Because heat transfer coefficient prediction was the goal, all wall-adjacent cells were sized to put the first grid point within a y^+ value of unity. The 2D grid was stacked in the lateral direction to create the three-dimensional grid. Steady simulations took advantage of symmetry, and only half of the width of the channel made up the domain. The half-pitch, 3D grid contained 4.4 million cells. A local view of the mesh on the midspan plane, with further detail around a rib shown in the inset, is given in Figure 7.2.

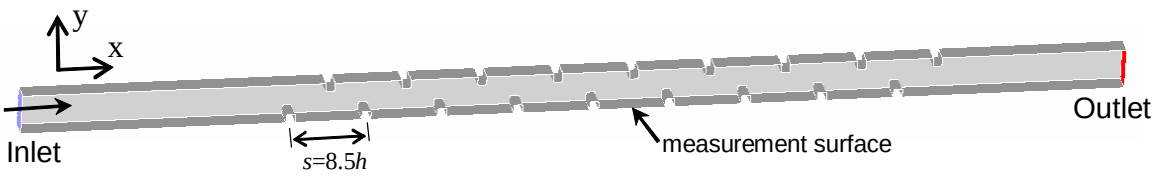

Figure 7.1 View of the computational domain for Case A showing the staggered rib configuration. Nusselt number measurements were taken on the surface between ribs 5 and 6 on the bottom wall.

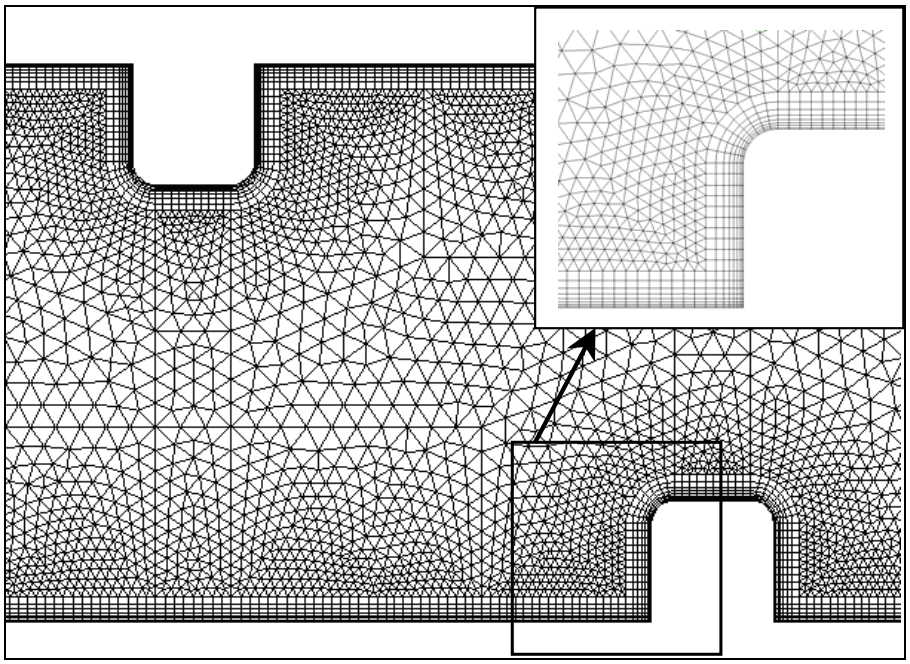

Figure 7.2 View of the computational grid on the midspan plane for Case A, including a detailed view of the near-wall mesh for resolution of the boundary layers.

The realizable k-ε turbulence model was used initially to close the steady RANS equations for Case A, and the two-layer model was used in the near-wall zone. Convergence was verified, and grid independence was established for the background grid. On eight processors of a Sun Microsystems Ultra 6500 computer, each simulation took about three days of runtime. Simulations were run for Reynolds numbers (based on channel hydraulic diameter) of 5500, 16500, and 25000.

Ribbed channel case B, based on the experiment of Acharya et al. (1997), was chosen for the availability of spatially-resolved measurements for the heat transfer coefficients over the full length of the channel, which contained eight ribs on the bottom wall. Also, the small ribs are perfectly square (no rounding on the edges), and this tends to increase gradients across the shear layer. The ribs had a height of h=0.635 cm, and

were equally-spaced at a distance of S=20h. The dimension of the channel in the cross-stream (y-) direction was 9.61h. The domain inlet was located at a distance of 15.75h upstream of the first rib, and the outlet was positioned at a distance of 23h aft of the eighth rib. The experiment had a channel width to height ratio of about 5, and all measurements were taken on the centerline in the lateral dimension. Therefore, the effect of the side walls is expected to be negligible. Steady flow near the centerline of the channel was assumed to be laterally uniform, and to take advantage of this feature, the domain for the steady simulations was two-dimensional in the x-y plane (it was assumed to be unit depth). A view of the computational geometry for Case B is shown in Figure 7.3.

Air at a temperature of T_0=300K entered through the inlet of the domain of Case B, and the Reynolds number, based on channel hydraulic diameter, was Re_D=24,000. Profiles for U, k, and ε were prescribed at the inlet. These profiles were taken from the

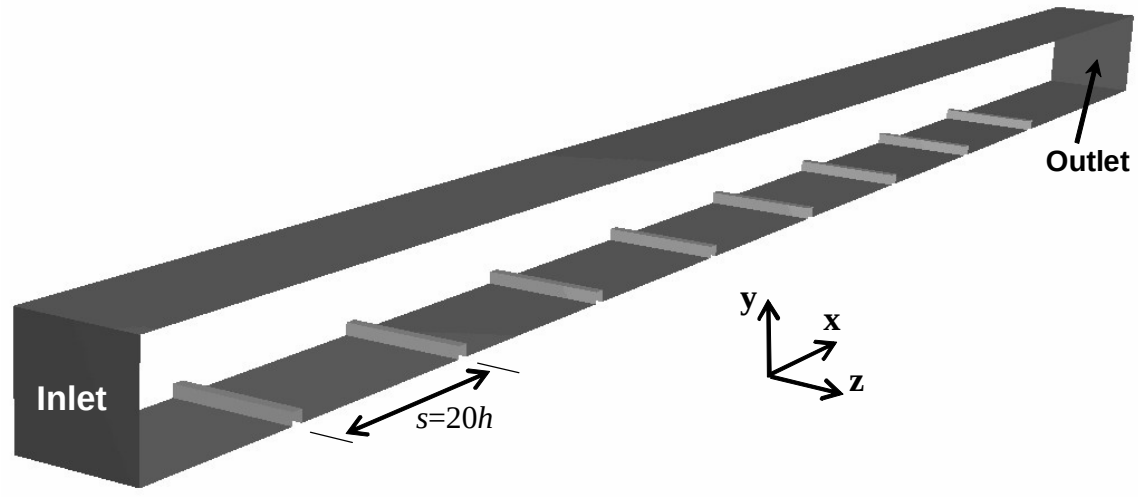

Figure 7.3 The geometry for ribbed channel Case B with eight ribs on the bottom wall only. The steady simulations employed a 2D domain by assuming unit dimension in the z-direction.

corresponding location in a simulation of the long inlet section to the test section in the experiment. In that simulation, uniform inlet velocity and turbulence was specified at the inlet (where flow entered from a large contraction in the wind tunnel). This procedure ensured that the boundary layer characteristics approaching the ribbed section would be accurately modeled, and it allowed the computational domain to be shortened for efficiency. Atmospheric pressure was specified on the domain outlet. The lateral boundaries of the domain were specified to be periodic in the z-direction to model the wide test section of the experiment. In order to calculate local heat transfer coefficients, a heat flux of q"=125 W/m^2 was specified for the entire bottom surface, excluding the ribs themselves.

As in the first case, the near-wall mesh for Case B was sized such that the first grid point adjacent to all walls was located at a $y^+ \leq 1$. Further, all cells in the regions between ribs, where shear layer breakup should occur, have aspect ratio of near unity for best resolution. The 2D mesh, consisting of 78,000 cells, was constructed using Gambit software. The steady cases were conveniently run on a single processor of a SunBlade 2000 machine, and convergence was reached in just over one hour. Simulations were run with the RKE model and a differential Reynolds-stress model (RSM) for comparison.

Steady Heat Transfer Results

For Case A, experimental data from Taslim et al. (1998) is available in the form of the area-averaged Nusselt number on the bottom surface of the channel between rib 5 and rib 6. Predictions for the same quantity are also plotted as a function of Reynolds number in Figure 7.4. Clearly, the numerical simulations, which employed the RKE turbulence model, underpredict the area-averaged heat transfer at this location. Both

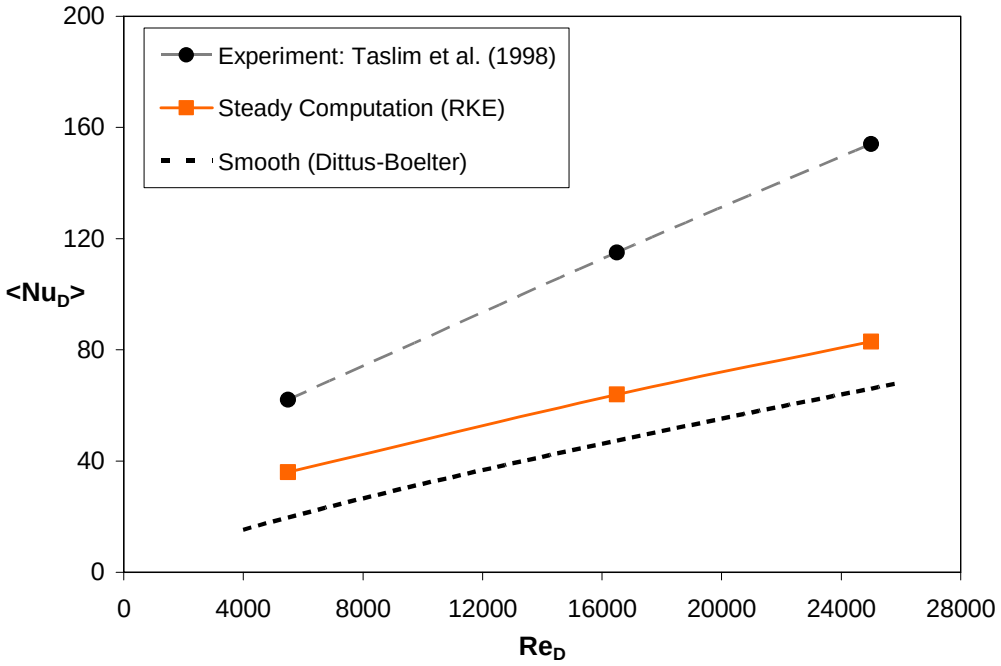

Figure 7.4 Area-averaged Nusselt number between ribs 5 and 6 as a function of Reynolds number for Case A. The computations largely underpredict heat transfer.

measured and computed Nusselt numbers show a near linear dependence on Re_D. Yet it is somewhat disconcerting that the slopes of the lines are not the same, making design decisions based on the computations difficult. The trend of the computated results follows the slope of the smooth-walled Dittus-Boelter correlation. Interestingly, the discrepancy between measured and computed heat transfer was about 45 percent for all Reynolds numbers.

For Case B, the local variation of the Nusselt number on the bottom surface at the midpitch is plotted in Figure 7.5. Measured data from Acharya et al. (1997) is included with the predictions for the two closure models. The simpler of the two models, RKE, shows a rapidly rising Nusselt number to a local maximum very close to the upstream rib. The heat transfer then falls gradually to a local minimum near the downstream rib before

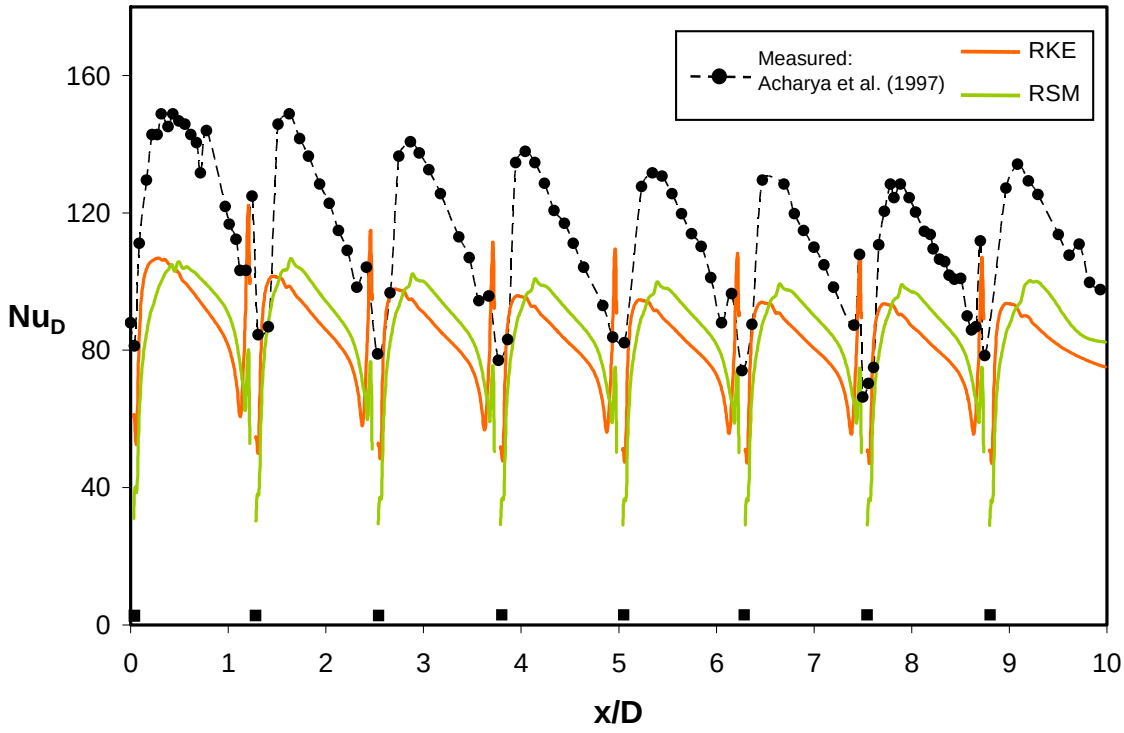

Figure 7.5 Measured and predicted variation of Nusselt number on the ribbed wall with downstream distance in Case B. The locations of the ribs are marked on the x-axis.

jumping to a peak level just upstream of the downstream rib. This peak heat transfer is due to a small, strong vortex that exists in the corner formed by the bottom wall and the rib. The RKE curve exhibits a very similar shape in the zones between all ribs. The peak and area-averaged Nu_D decrease slightly from the first through the third inter-rib zones, and become nearly constant after the third zone as it reaches a fully-developed condition, meaning the pattern is the same in all downstream inter-rib zones. Compared to experiments, it is clear that the RKE model significantly underpredicts the peak Nusselt number after each rib by about 30%. The location of the first peak in heat transfer corresponding to flow reattachment is slightly closer to the upstream rib than the experiments in all cases.

The Reynolds-stress model simulation gave a heat transfer prediction that was only marginally improved over the RKE result. In Figure 7.5, a similar pattern to the curves between each rib was seen as in the RKE case, but the first peak in Nu_D was located further downstream of each rib, and this matched the location of the experimental peak very closely. The local maximum levels were higher, and were about 20% to 25% less than the measured peaks. Another difference was that RSM predicted a smaller jump in heat transfer near the upstream face of each rib.

For both test cases, numerical results were characterized by a significant (30% to 45%) underprediction in heat transfer, regardless of the turbulence model chosen. This major discrepancy led the present author to believe that something fundamental was missing in the computational model. The rib problem is well-documented in the literature, and involves a shear layer that tends to become unstable (a Kelvin-Helmholz instability). This leads to the breakup of the shear layer into small-scale, coherent eddies. Like turbulence at slightly smaller scales, these unsteady eddies are very effective at moving thermal energy away from the wall where it is transported by the mean flow. Therefore, the unsteadiness should have a considerable effect on the heat transfer coefficient. Obviously, the steady RANS simulations do not include this effect.

Unsteady Simulations

To test the theory that resolution of small-scale unsteadiness could have a significant impact on the heat transfer predictions, unsteady RANS simulations were conducted. Fluent 6 includes the capability for time-accurate, unsteady simulations with the same turbulence models used for steady simulations. Because the unsteady

fluctuations would likely be asymmetric about the midspan plane, the computational domains for the URANS simulations for both test cases had to be modified.

For Case A, the domain for the unsteady simulations included the full width of the channel (not just a half-width with symmetry as in the steady simulations). To reduce the computational expense, which is much greater for URANS over the equivalent steady case, the channel domain was shortened to include only three ribs on each wall – the two ribs adjacent to the heat transfer measurement area and the one preceding these ribs. This clipped domain is shown in Figure 7.6. To ensure that the same conditions were modeled, profiles for velocity, temperature, and turbulence quantities at the new URANS inlet were taken directly from the steady simulations of Case A.

The domain for the unsteady simulation of Case B had a lateral (z-) dimension (unlike the 2D steady runs) in order to resolve any three-dimensionality in the instantaneous flow field because of unsteady fluctuations. Based on in-house tests verifying sensitivity limits to domain width, it was decided to make the channel width

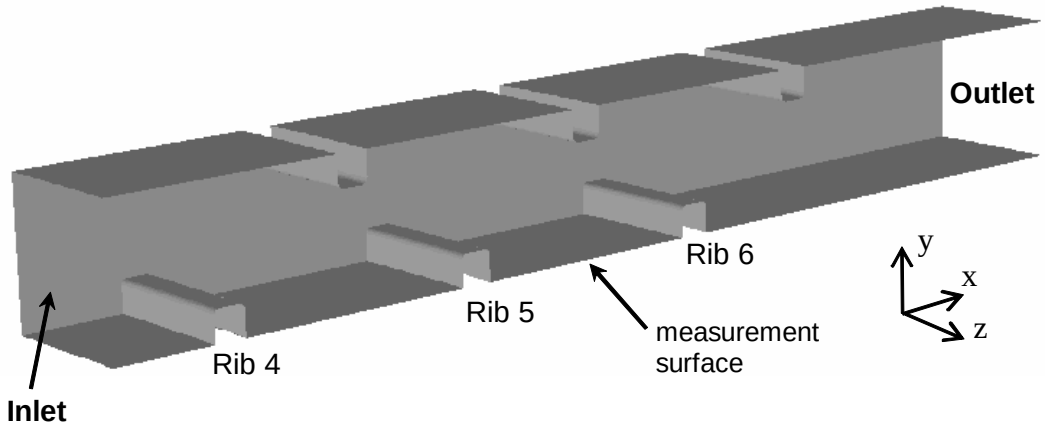

Figure 7.6. Computational domain for the Case A URANS simulations. Profiles at the inlet were taken from the corresponding location in the steady simulations.

equal to 5*h*, or five times the characteristic length or eddy size. Periodic planes (the transparent side boundaries in Figure 7.3) served at the lateral bounds of the domain. To build the 3D grid for the URANS simulation, the 2D grid was "stacked" with 40 layers of cells in the lateral direction. The background 3D mesh consisted of 3.1 million hexahedral finite volumes. High grid density and uniformity is clearly evident in Figure 7.7, a view of the background mesh on surfaces and a periodic plane near one rib.

For the time-accurate unsteady simulations, it was necessary to specify a time step. Based on known shedding frequencies for vortex shedding behind ribs, a non-dimensional time step size $U\Delta t/h = 0.2$ was selected for both test cases. Point monitors of instantaneous properties in the unsteady shear-layer roll-up zone indicated adequate temporal resolution for the actual periods of the unsteady fluctuations in the simulation.

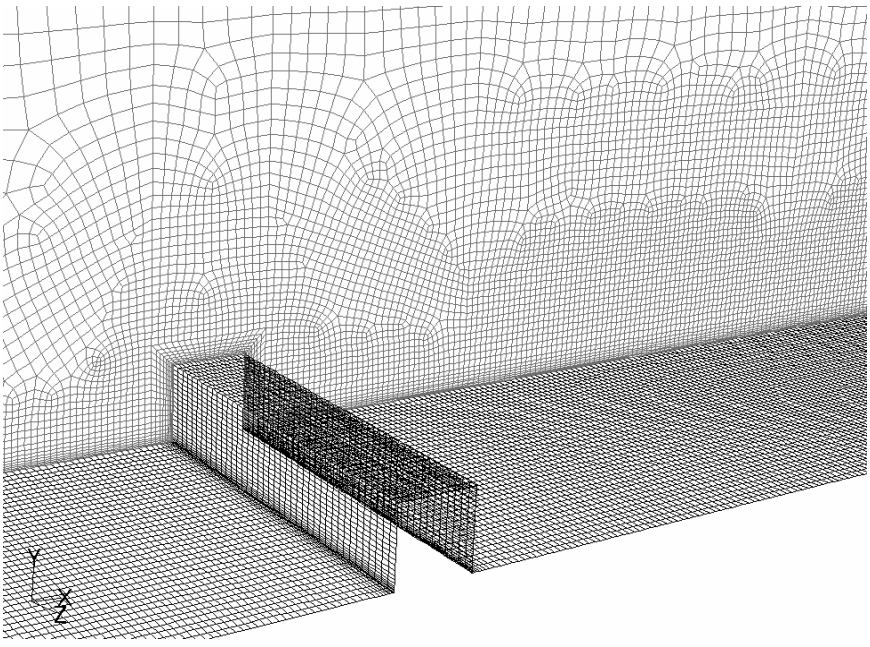

Figure 7.7 View of the surface mesh on and near one rib for ribbed channel Case B.

In addition, a time-step sensitivity study was conducted, in which increasing the time step by an order of magnitude had negligible effect on the period of the fluctuating velocity downstream of a rib and on the time-averaged heat transfer. Within each time step, ten iterations gave sufficient convergence of the solution.

For both Case A and Case B, unsteady simulations were attempted with both the standard k-ε and realizable k-ε turbulence models. During all of these time-accurate runs, all unsteadiness was damped out eventually, and the solution became steady. This result is because the conventional eddy-viscosity models are too diffusive to sustain small-scale unsteady motions. One method for encouraging small-scale unsteadiness to grow or be sustained is to force small perturbations of the variables, either throughout the domain, only at the inlet, or both. However, difficulties arise in prescribing the magnitude of these perturbations so as not to affect the solution or to introduce certain artificial frequencies in the flow. A better solution to the problem is obtained by developing a physics-based turbulence closure designed for unsteady flows.

To this end, a new turbulence model was developed in the ACRL at Clemson University. It was based initially the steady modeling work of Walters (2000), and the unsteady model was modified and documented by York et al. (2005). It is a three-equation, eddy-viscosity model that includes improved near-wall physics. In addition to k and ε transport equations, an additional partial differential transport equation for a dimensionless strain rate parameter (σ) is solved to include the effects of strain on turbulence. The model is modified to account for the effects of unsteadiness on the turbulent viscosity to form an unsteady-based model, named ACRL-EVU (Eddy-Viscosity model for Unsteady flows). To resolve the unsteady fluctuations, the

production of k in rapidly strained, non-equilibrium regions of the flowfield is suppressed by applying damping functions to the turbulent viscosity. These damping functions depend on the mean-to-turbulent time-scale ratio, Sk/ε, and the alignment of the instantaneous strain rate tensor with the time-averaged strain rate tensor. This is a novel approach that allows unsteady features of the flowfield to be resolved without the grid and computational expense of large eddy simulation (LES). More details on the model are given by York et al. (2005), and the model equations are included in Appendix B.

The in-house unsteady model was implemented within Fluent 6 via user-defined functions. Since the model required certain time-averaged quantities, additional user-defined functions were added to compute and store time averages of the variables, which updated after each time step. The time-averaged quantities were also important in defining solution convergence and refinement of the grid in the unsteady simulations, as discussed in Chapter 4. Initial results with the ACRL-EVU model were encouraging, with realistic, sustained, unsteady motions observed for both Case A and Case B.

It should be noted that, while grid independence was declared for the background grid for the steady simulations, this was not the case for the URANS cases. Specifically, the time-averaged results were very sensitive to the cell size just above the ribs, where a strong and very thin shear layer exists, and to a lesser extent to the cell size aft of the rib where shear layer instability and breakup occurs. In order to specifically target the time-averaged shear layer location, a "refinement parameter" was defined by $R = \omega y / U$, and cells were refined when this value was above a certain level. For Case B, the 8-rib case, two grid refinement cycles were conducted. The first refinement targeted cells with large values of R that were located between $1h$ upstream to $8h$ downstream of each rib and the

second refinement split cells directly over the top surface of the rib into even smaller cells. A closeup view of the refined mesh on the midspan plane near one rib is shown in Figure 7.8. After two adaption cycles, the final mesh for Case B consisted of 8.5 million finite-volumes.

The URANS simulation of Case B was run on a cluster of 6 SunBlade 2000 machines from Sun Microsystems, each with 2 processors and 8 gigabytes of RAM. Each time step required 10 minutes of wall-clock time, and approximately 2000 time steps were required for convergence of the time-averaged solution on the adapted grid (8.5 million cells). The required 14 days of run-time was an order of magnitude more time than needed for a 3D steady simulation of this problem, and about two orders of magnitude more than the 2D steady simulations.

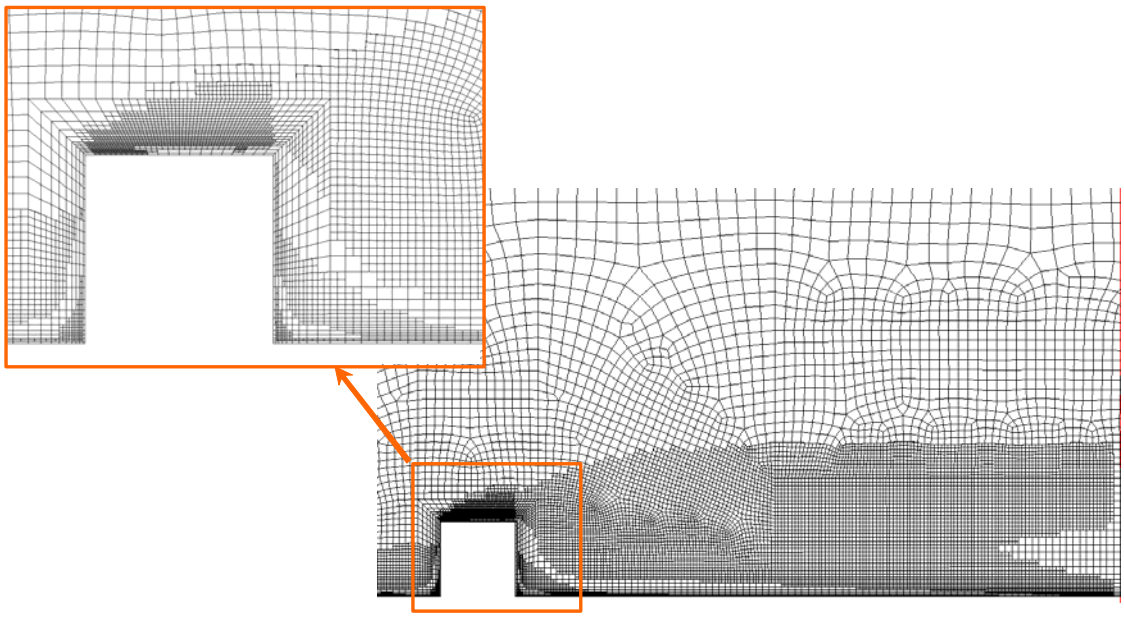

Figure 7.8 Numerical grid near a rib on the channel midspan plane after two refinement cycles. Note the high resolution over the rib and in the area of the shear layer aft of the rib.

Unsteady Simulation Results

It is clearly evident from monitoring flowfield that unsteady shear layer breakdown and roll-up is present behind all ribs. Focusing first on Case A, Figure 7.9 shows contours of normalized streamwise (*x*-) velocity overlaid with black velocity vectors on the centerline plane near ribs 5 and 6 on the bottom wall for the ACRL-EVU case. There is a difference between the instantaneous (at a moment in time) result and the time-averaged result, and coherent eddies are visible. The area-averaged, time-averaged Nusselt number between Rib 5 and Rib 6 is plotted as a function of Reynolds number in Figure 7.10, along with data from the steady (RKE) simulations and the measured data. As expected, the addition of unsteady physics improves the heat transfer prediction

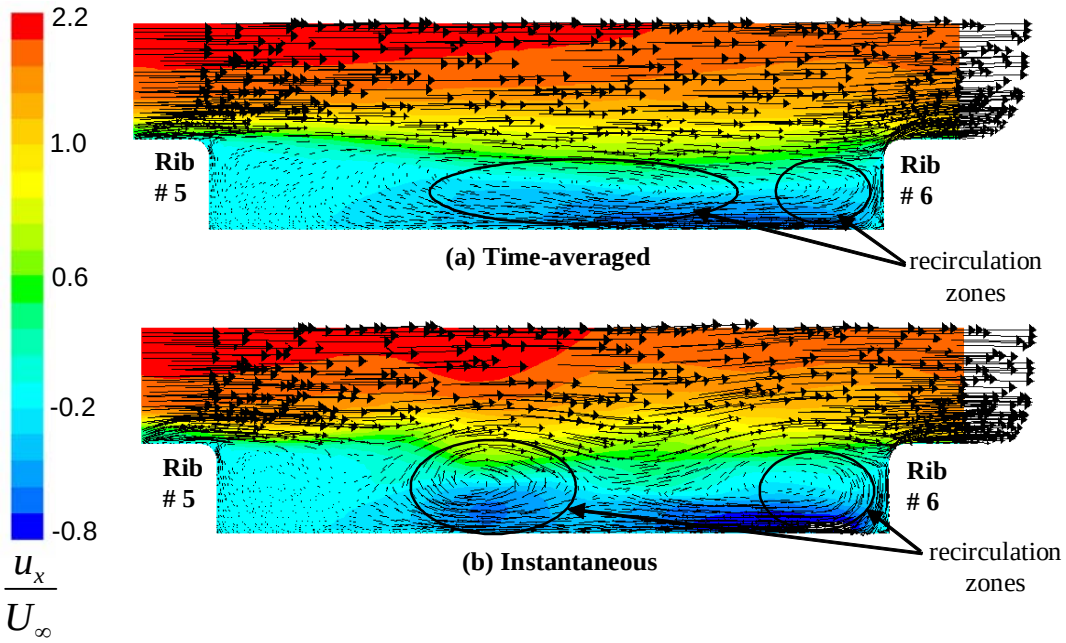

Figure 7.9 Velocity vectors overlaid on contours of normalized x-velocity on the midspan (centerline) plane. The time-averaged result is shown in (a) and a snapshot at a moment in time is shown in (b).

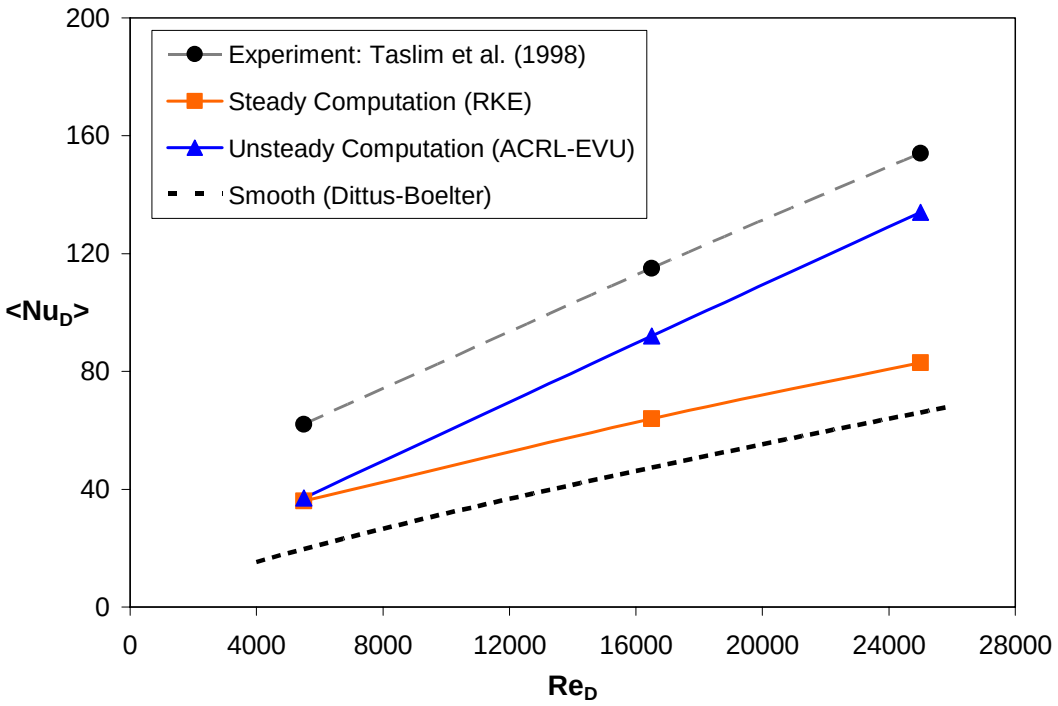

Figure 7.10 Steady and unsteady simulation predictions for area-averaged Nusselt number at three Reynolds numbers for Case A. Included are measurements and a smooth-wall correlation.

significantly, especially at high end of the Reynolds number range, where the underprediction fell from 45% to 13%.

For Case B, unsteady motions in the flow field, and its impact on the heat transfer can be seen in Figure 7.11. The instantaneous z-vorticity contours on the centerline plane near ribs 7 and 8 are shown in Figure 7.11(a), and the same view at an instant in time that is 12 time steps later is shown in Figure 7.11(b). Below the contours in Figure 7.11 are plots of the measured and predicted Nusselt number between ribs 7 and 8. Results for the RKE model (unsteady, 3D simulation) and the ACRL-EVU model (unsteady, 3D simulation) are compared in the figure. It is evident that the RKE model does not predict an unsteady flow, as the vorticity contours are the same in (a) and (b). This is seen by the

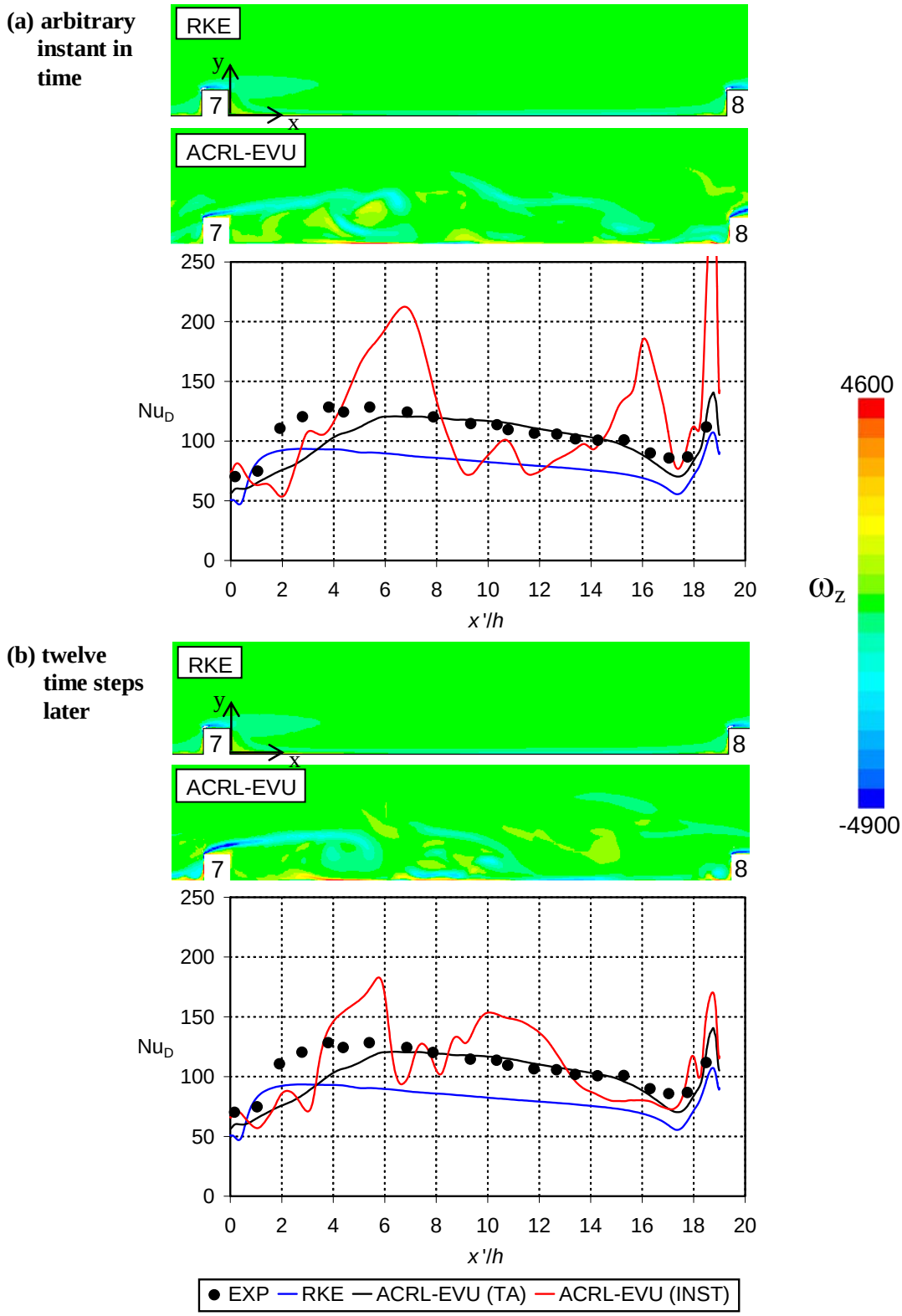

Figure 7.11 Contours of z-vorticity on the centerline plane in Case B for RKE and ACRL-EVU models at (a) an arbitrary instant in time and (b) twelve time steps later. Below the sets of contours are plots of the Nusselt number between ribs 7 and 8.

fact that the shear layer, marked by contours of z-vorticity, and the distribution of Nusselt number does not change with time. In addition to the time-averaged (TA) results from the ACRL-EVU case, the instantaneous (INST) Nusselt number curves are included. It is clear that the instantaneous amplitude in the streamwise variation of Nu_D can be quite large. This leads to large gradients of heat transfer (i.e. temperature) in the streamwise direction. The physics of the vortex structures shown in the contours above the plots can be used to explain the local peaks in Nu_D. As the shear layer rolls up and breaks down past the rib, vortices are shed off. As the vortices move downstream, the heat transfer is affected thus causing a migration of the initial peak in Nusselt number. Eventually, as the flow moves downstream, the effects of rib 7 are diminished and the presence of rib 8 is felt.

The time-averaged Nusselt number distribution over the full bottom surface from the ACRL-EVU simulation for Case B is plotted in Figure 7.12. For comparison, included on the plot are the steady solutions with RKE and RSM, presented previously. The ACRL-EVU model exhibited heat transfer predictions that were considerably different from the other two cases, and clearly the area-averaged Nusselt numbers between ribs is much closer to measured values. Aft of the first rib, the Nusselt number increased more gradually than the steady model curves to a peak located further downstream than the steady computations and the experiment showed. Heat transfer prediction in the second interrib zone was much different than the first, with a smaller peak that was closer to the upstream rib. The peak Nu_D corresponding to flow reattachment continues to move upstream in the third and fourth interrib zones. Downstream of the fifth rib, the flow is nearly fully-developed, and the ACRL-EVU

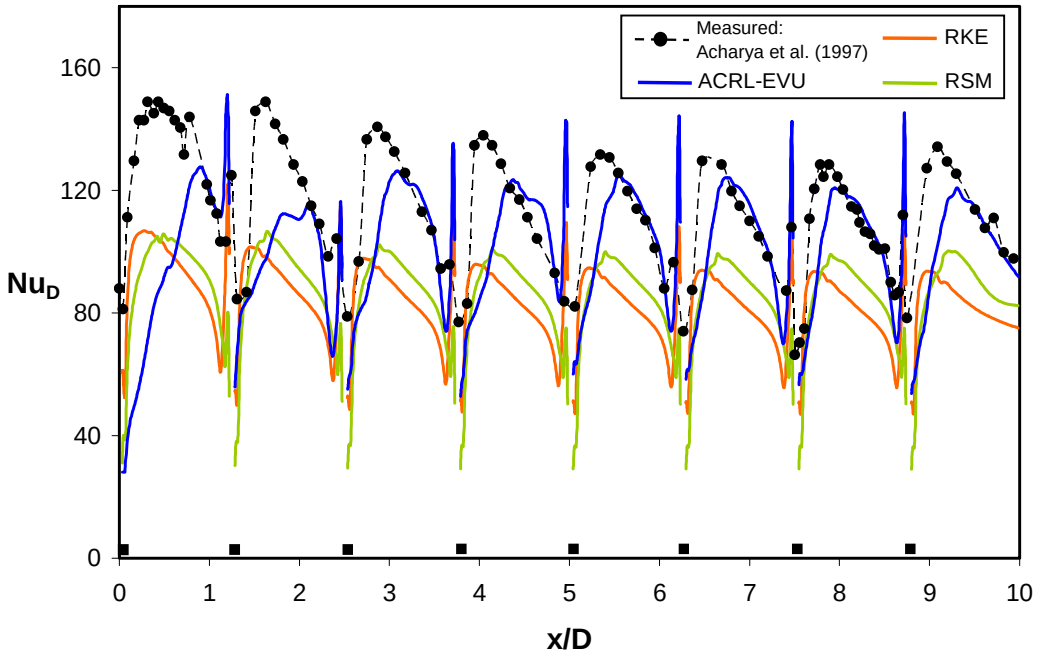

Figure 7.12 Predicted and measured Nusselt number distribution on the bottom ribbed wall at the channel centerline for Case B. The unsteady ACRL-EVU case gives improved results for heat transfer compared to the steady simulations, especially after the fifth rib.

prediction approaches the measured distribution, with less than a 10 percent difference in the local maximum value at reattachment. A very large, rapid increase in Nu_D is predicted just upstream of each rib, as the unsteady vortices that form in these corners are very strong.

In many applications of ribbed passages for augmented heat transfer, including gas turbine airfoil cooling, the passages are relatively long with numerous ribs in the streamwise direction. The designer is primarily concerned with predicting heat transfer in the fully-developed region, after initial variations have disappeared. As seen in Figure 7.12, for the experiment and all simulations, this condition is met after 4 or 5 ribs downstream of the inlet. It is instructive to focus on Nusselt number distributions

between rib 7 and rib 8 (the final interrib zone), plotted in Figure 7.13. The severe underprediction of heat transfer by the RKE and RSM models is obvious, although RSM does a reasonable job of producing the shape of the curve and the streamwise location of the first peak aft of the rib corresponding to the reattachment point. The URANS simulation does a much better job overall of predicting Nusselt number. In Figure 7.13, the ACRL-EVU curve initially has a smaller slope than the experiments and reaches a peak slightly further downstream (by about 2 rib heights), indicating an overprediction of the reattachment length. From x'/h=7 to the rib 8 location (x'/h=19), the URANS prediction is in very good agreement with the measured data.

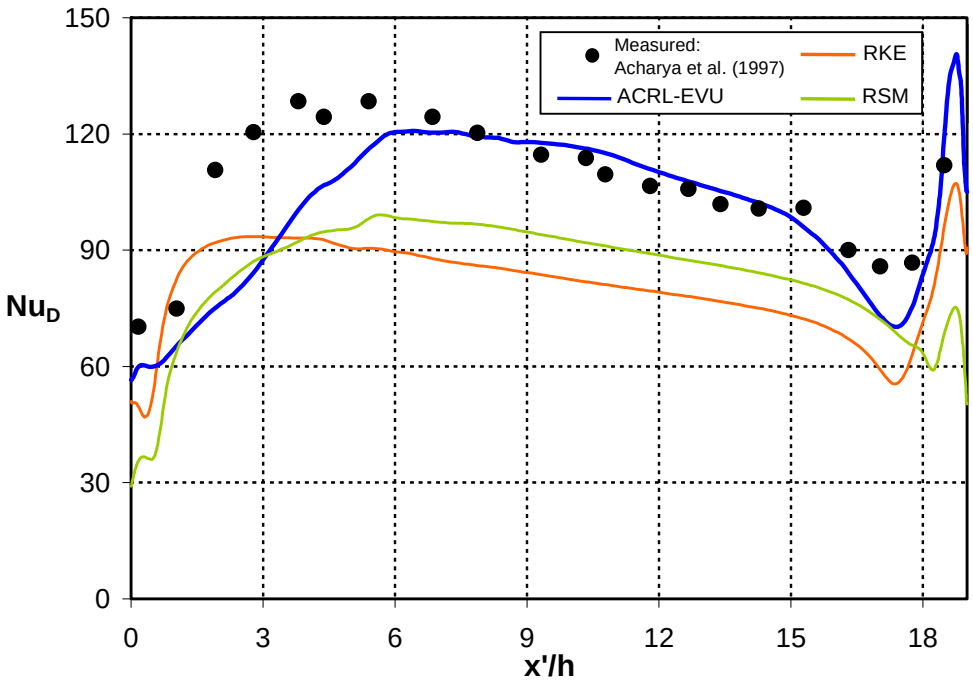

Figure 7.13 Predicted and measured Nusselt number on the ribbed wall in Case B at the channel centerline between Rib 7 and Rib 8. The streamwise distance, x', is measured from Rib 7 and is normalized by the rib height.

Since highly three-dimensional conduction eliminates many large temperature variations on the cooling channel walls inside a turbine airfoil, designers often seek an estimate of area-averaged Nusselt number for the internal cooling passages. Table 7-1 lists the area-averaged (streamwise-averaged) Nusselt number on the ribbed wall for the experiment and the three simulations of Case B. The first two columns contain results for the full channel (all 8 ribs). The realizable k-ε model and the Reynolds stress model both show an underprediction in mean Nusselt number of over 26%, while the unsteady ACRL-EVU solution results in only a 12.6% underprediction. Again focusing in the fully-developed region, the right-side of Table 7-1 contains area-averaged Nusselt numbers for the wall between rib 7 and rib 8. Again, there is a sizable underprediction in heat transfer for the RKE model and RSM. The ACRL-EVU result is a minimal 6.5% below the measured value, which is certainly accurate enough to make sound design decisions based on the unsteady computations.

Results of the unsteady simulations clearly show the importance of including the effects of unsteady shear-layer breakdown and vortices into a model for this class of problems. A drawback of the URANS method with the ACRL-EVU model, at least

Table 7-1 Area-averaged Nusselt numbers for Case B.

	Full Channel		**Between Ribs 7 & 8**	
	Mean Nu_D	**% Under-prediction**	**Mean Nu_D**	**% Under-prediction**
Experiment: Acharya et al. (1997)	113.5	---	106.2	---
RKE	83.6	26.3	80.5	24.2
RSM	83.9	26.1	81.6	23.1
ACRL-EVU	99.2	12.6	99.3	6.5

in a design function, is the large computational expense. Additionally, experience indicates that the unsteady simulations of ribbed channels require extensive grid-independence studies, as the time-averaged (unsteady) results are much more sensitive to the grid resolution than a steady solution. Meshes after several levels of refinement can put the URANS simulation in the range of a large eddy simulation in terms of computational requirements. The next section discusses an alternative to the costly, time-accurate simulation in the form of a turbulence model developed recently in the ACRL by Holloway (2005).

Unsteady Effects in a Steady Simulation

The previous work confirms the author's initial hypothesis that the small-scale unsteadiness plays a major role in the heat transfer on ribbed walls, and therefore it must be included in a numerical model for accurate predictions. The in-house ACRL-EVU model allows small-scale unsteady motions to be resolved in a time-accurate simulation. However, it is very computationally intensive to run time-accurate simulations, since often thousands of time steps are needed for accurate averaging. Additionally, in some situations, the domain for the unsteady simulations must be expanded because of non-symmetry or three-dimensionality in the unsteady motions that do not exist in a steady solution to the same problem.

Consider Case B, the wide channel with 8 ribs on the bottom wall. Since the sidewalls were reasonably expected to be negligible on the centerline heat transfer, the steady simulations employed a 2D domain containing 78,000 cells. With about 3000 iterations required for convergence, and at 2 seconds per iteration on a single CPU, about 100 wall-clock minutes or 100 cpu-minutes were required. Next consider the unsteady

simulation for the same problem. Because the unsteadiness may exhibit motion in the lateral direction, it was necessary to expand the domain a finite width in this dimension. The resulting 3D mesh contained 3.1 million cells, which expanded to 8.5 million cells after two requisite refinement cycles. To reach convergence, the simulation required 2000 time steps, with 10 iterations per time step. Run on 12 processors, each *iteration* took about one minute, so the run-time was 20,000 wall-clock minutes or 240,000 cpu-minutes. The unsteady simulation cpu-time requirement was more than 3 orders of magnitude greater than the steady case. This makes the URANS simulation somewhat ill-suited for a design environment where quick turnaround is expected.

Additional problems where shear layer unsteadiness and roller vortices turned out to be important were studied by other researchers in the ACRL, and similar increases in run-time over steady simulations were found. In an effort to fix this difficulty, Holloway (2005) developed a new eddy-viscosity-based model that was designed to include the effects of the roller vortices in a steady framework. The new in-house model was named ACRL-SDSM, for Semi-Deterministic Stress Model, since the unsteady fluctuations are partly “deterministic”, meaning they are not completely random but can be characterized by some preferred amplitudes and frequencies. In this way, unsteadiness is unlike turbulent fluctuations, which are random and must be modeled statistically. Physically, an ongoing, three-way exchange of energy exists between the mean flow, the turbulent fluctuations, and the unsteady vortices, which are of a scale slightly larger than the turbulence. The ACRL-SDSM model includes this transfer of energy between the modes.

The ACRL-SDSM model of Holloway (2005) is a three-equation model with partial-differential transport equations for turbulent kinetic energy (k), non-turbulent

kinetic energy (k_{nt}), and the specific dissipation rate of turbulence (ω). The non-turbulent kinetic energy includes the energy of roller vortices, and its transport equation is modeled similarly to the turbulent kinetic energy equation. The model calculates a total effective viscosity, consisting of molecular, turbulent, and non-turbulent contributions (the latter two from transport equations). Through this effective viscosity, the effects of vortex shedding are accounted in a steady simulation. The reader is referred to the thesis of Holloway (2005) for a more detailed description of the model, including the equations. The ACRL-SDSM model, like ACRL-EVU, is implemented in Fluent 6 with user-defined functions.

The ACRL-SDSM model was applied to ribbed channel Case B. Since the model is for use in a steady simulation, the problem could be modeled as two-dimensional, reducing the mesh size back to 78,000 cells. Because of the additional transport equation, the ACRL-SDSM simulation took about 15% longer to run that RKE, but this was still two orders of magnitude less time than URANS.

Figure 7.14 shows the prediction of Nusselt number on the bottom (ribbed) wall for Case B with the ACRL-SDSM model. The RKE and ACRL-EVU (unsteady) results are also plotted for reference. Overall, the new semi-deterministic stress model gives very good predictions for heat transfer, even better than when fully-resolving the vortex shedding in the URANS simulations. The heat transfer pattern predicted by ACRL-SDSM is very similar between each adjacent pair of ribs. Behind each rib, the location and magnitude of the peak Nu_D, corresponding approximately to the reattachment point, closely matches the measurements of Acharya et al. (1997). Downstream of this peak, the new steady model slightly underpredicts the local Nusselt number. Figure 7.15 shows the

Nusselt number variation between rib 7 and rib 8. The superior performance of ACRL-SDSM is clearly evident, especially compared to the realizable *k*-ε model result. The turbine airfoil conjugate heat transfer methodology benefits greatly from the ability to obtain economic and fairly accurate predictions for heat transfer coefficients in ribbed channels.

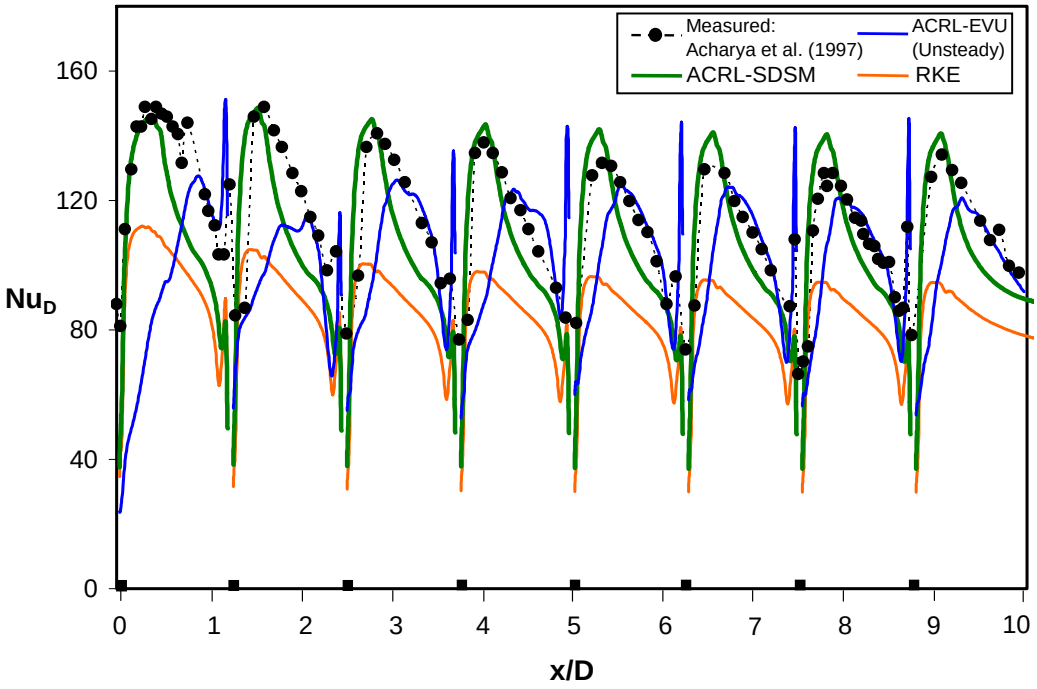

Figure 7.14 The economical ACRL-SDSM model gives good predictions for local Nusselt number on the ribbed wall in Case B.

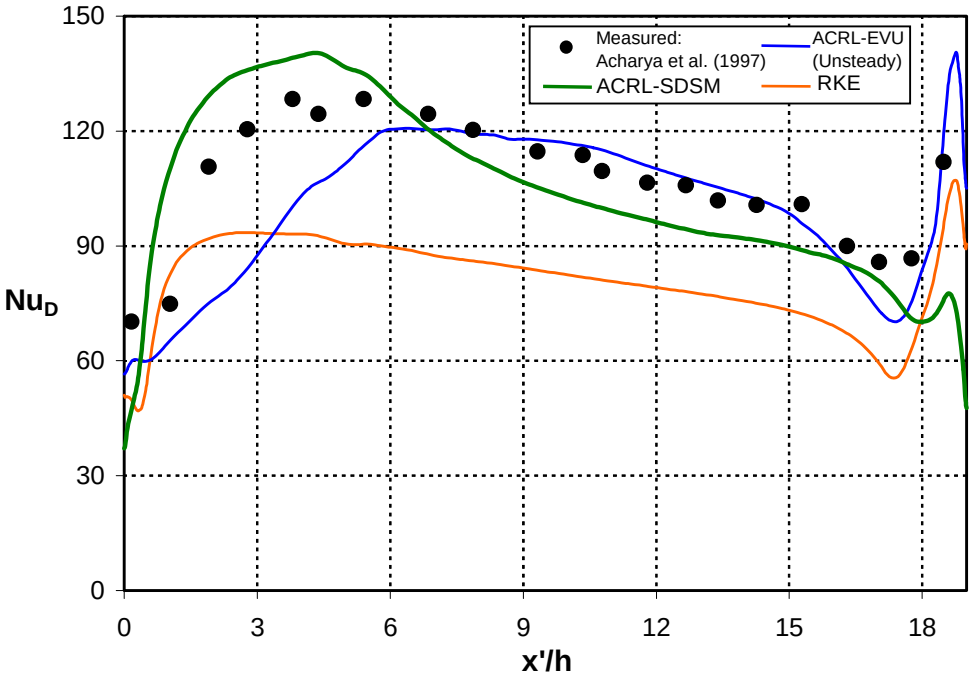

Figure 7.15 Predicted and measured Nusselt number on the ribbed wall in Case B at the between Rib 7 and Rib 8. The ACRL-SDSM model result matches the measured trend.

CHAPTER 8

DEVELOPMENT OF A CURVATURE-SENSITIVE TURBULENCE MODEL

The need for a new turbulence model that can incorporate the effects of streamline curvature on the turbulence field was discussed in Chapter 6. Specifically, the external wall temperature in the conjugate heat transfer turbine vane case was overpredicted significantly on the leading portion of the suction surface, and the alarming feature was that the trend in the predictions did not match the measurements where strong convex curvature of the airfoil existed. This author hypothesized that the observed discrepancy was due to the inability of the turbulence models to correctly account for the stabilizing effect of convex curvature, which would tend to reduce turbulent kinetic energy in this region, lowering the heat transfer coefficients and therefore the wall temperature.

Inaccurate predictions for heat transfer coefficients can lead to errors in the internal temperature of the metal. Even a few degrees error in metal temperature can mean large inaccuracies in the life prediction for the part. Therefore, a new model for streamline curvature effects is necessary for the conjugate methodology to be employed in a gas turbine design environment. Additionally, most complex internal cooling schemes incorporate channels that make multiple passes through the airfoil, requiring multiple 180^{o} turns. A secondary benefit of developing the new turbulence model for streamline curvature effects should be more accurate predictions for heat transfer coefficients on the channel surfaces near the turns, further extending the scope of the conjugate methodology.

This chapter details the development of a new eddy-viscosity model that includes sensitivity to streamline curvature effects. The model is a two-equation, eddy-viscosity-model, developed via a physical analysis and designed to be implemented easily into any general-purpose, structured or unstructured solver. In order to check the performance of the new model, a series of test cases are conducted and presented. Evaluation of the new model performance for the complex conjugate vane problem and the three-dimensional 180^o channel turn is reserved for the following chapter.

New Model Development

The new model is designed to include the effects of streamline curvature on the turbulence structure, and, by analogy, will also contain the effects of system rotation. As stated earlier, the approach taken in the present work is based on the Boussinesq approximation, which has the advantages of linearity with respect to the mean strain tensor, tensor invariance, and reference frame indifference (when the eddy-viscosity definition is also frame indifferent). Additionally, this approach is simple to implement and generally stable during the solution process for nearly all problems.

The anisotropy tensor, b_{ij}, whose components indicate the magnitude of departure from isotropic turbulence, is defined as:

$$b_{ij} = \frac{\widetilde{\overline{\rho u_i u_j}}}{\overline{\rho} k} - \frac{2}{3}\delta_{ij} \tag{8.1}$$

The turbulence model is then used to construct the anisotropy tensor. Using the Boussinesq assumption (Equation 5.1) for the Reynolds stress tensor, the anisotropy tensor may be written as:

$$b_{ij} = -\frac{\mu_T}{\overline{\rho} k}\left(\frac{\partial U_i}{\partial x_j} + \frac{\partial U_j}{\partial x_i}\right) + \frac{2}{3}\left(\frac{\mu_T}{\overline{\rho} k}\frac{\partial U_k}{\partial x_k}\right)\delta_{ij} \tag{8.2}$$

Typical eddy-viscosity models have no sensitivity to streamline curvature, but Reynolds-stress-based models do contain this feature. Therefore, development starts from an algebraic stress model (ASM), which is derived from the Reynolds-stress transport equations, given below for a rotating or non-rotating reference frame:

$$\frac{D\overline{u_i u_j}}{Dt} = T_{ij} + P_{ij} + \pi_{ij} - \varepsilon_{ij} - F_{ij} \tag{8.3}$$

Rodi (1980) simplified the above differential equation to an algebraic equation with some modeling and assumptions. The left-hand-side is simplified as:

$$\frac{D\overline{u_i u_j}}{Dt} = \frac{\overline{u_i u_j}}{k}\frac{Dk}{Dt} \tag{8.4}$$

On the right-hand-side, the diffusive transport term is assumed to be:

$$T_{ij} = \frac{\overline{u_i u_j}}{k} T^k \tag{8.5}$$

The contraction of equation 8.3, multiplied by 0.5, results in the transport equation for the turbulent kinetic energy of the form:

$$\frac{Dk}{Dt} = T^k + P^k - \varepsilon \tag{8.6}$$

Then equations 8.3 through 8.6 may be combined to give the following algebraic expression:

$$\frac{\overline{u_i u_j}}{k} = \frac{P_{ij} + \pi_{ij} - \varepsilon_{ij} - F_{ij}}{P^k - \varepsilon} \tag{8.7}$$

The production term is exactly given by:

$$P_{ij} = -u_i u_1 \frac{\partial U_j}{\partial x_1} - u_j u_1 \frac{\partial U_i}{\partial x_1} \tag{8.8}$$

Additional modeling is required to develop a final form of the ASM. Gatski and Speziale (1993) modeled the dissipation tensor by assuming isotropic dissipation:

$$\varepsilon_{ij} = \frac{2}{3}\varepsilon\delta_{ij} \tag{8.9}$$

The pressure strain term serves to redistribute the turbulent stresses, and is modeled by Gatski and Speziale (1993) with a linearized form:

$$\begin{aligned}\pi_{ij} = &-\left(\frac{C_1}{2}\right)\varepsilon b_{ij} + C_2 k S_{ij} + \left(\frac{C_3}{2}k\right)\left(b_{ik}S_{jk} + b_{jk}S_{ik} - \frac{1}{3}b_{mn}S_{mn}\delta_{ij}\right) \\ &+ \left(\frac{C_4}{2}k\right)\left(b_{ik}W'_{jk} + b_{jk}W'_{ik}\right)\end{aligned} \tag{8.10}$$

where W'_{ij} is the absolute rate-of-rotation tensor:

$$W'_{ij} = \frac{1}{2}\left(\frac{\partial U_i}{\partial x_j} - \frac{\partial U_j}{\partial x_i}\right) + e_{mji}\omega_m \tag{8.11}$$

Finally, the term F_{ij} is the rotational production given by:

$$F_{ij} = 2\omega_m\left(e_{mkj}\overline{u_i u_k} + e_{mki}\overline{u_j u_k}\right) \tag{8.12}$$

where ω_m is the angular velocity of the reference frame relative to an inertial frame. In order to achieve a solution for the anisotropy tensor, the assumption of "quasi-equilibrium" is invoked. A structural parameter, β_{ij} is defined by:

$$\beta_{ij} = \frac{\overline{u_i u_j}}{k} \tag{8.13}$$

Mathematically, the condition of quasi-equilibrium is given by,

$$\frac{D\beta_{ij}}{Dt} = 0\ , \tag{8.14}$$

and physically this means that the turbulence structure responds instantaneously to the mean strain rate.

Using the above modeling and assumptions, Gatski and Speziale (1993) derived the following ASM formulation for the anisotropy tensor through rigorous mathematical manipulation:

$$b_{ij} = \frac{\left(\frac{4}{3} - C_2\right)}{\left(C_3 - 2\right)} \cdot \frac{6}{3 - 2\eta^2 + 6\zeta^2} \cdot \left[S_{ij}^* + \left(S_{ik}^* W_{kj}^* + S_{jk}^* W_{ki}^* \right) - 2\left(S_{ik}^* S_{kj}^* - \frac{1}{3} S_{kl}^* S_{kl}^* \delta_{ij} \right) \right] \quad (8.15)$$

where

$$\eta^2 = S_{ij}^* S_{ij}^* \quad (8.16)$$

$$\zeta^2 = W_{ij}^* W_{ij}^* \quad (8.17)$$

$$S_{ij}^* = \frac{1}{2} g \frac{k}{\varepsilon} \left(2 - C_3\right) S_{ij} \quad (8.18)$$

$$W_{ij}^* = \frac{1}{2} g \frac{k}{\varepsilon} \left(2 - C_4\right) \cdot \left[\Omega_{ij} + \frac{\left(C_4 - 4\right)}{\left(C_4 - 2\right)} e_{mji} \omega_m \right] \quad (8.19)$$

and

$$g = \left(\frac{1}{2} C_1 + \frac{P^k}{\varepsilon} - 1 \right)^{-1} \quad (8.20)$$

Note that Ω_{ij} is the relative rate-of-rotation tensor:

$$\Omega_{ij} = \frac{1}{2} \left(\frac{\partial U_i}{\partial x_j} - \frac{\partial U_j}{\partial x_i} \right) \quad (8.21)$$

Though Gatski and Speziale (1993) refer to their formulation as an explicit ASM, the above expression is actually semi-implicit since the production of *k*, contained in equation 8.20, is dependent on the anisotropy tensor. Note that the inclusion of the frame

rotation rate, ω_m, in the term W_{ij}^* (equation 8.19) is intended to sensitize the turbulence structure to rotation.

Walters (2000) explained that the influences of flow rotation and streamline curvature are not accurately represented in the above ASM (or any ASM from the literature). Additionally, the condition of frame indifference was shown to be violated by fully-implicit or semi-implicit algebraic stress models, and this is due to one assumption used to simplify the differential Reynolds-stress transport equations to their algebraic form. Walters (2000) presented a new derivation of the algebraic stress equations that rectified these deficiencies, and the result (a new ASM) forms the basis of the new eddy-viscosity model developed in the present work.

A distinction must be drawn between rotating flows and rotating reference frames. In the literature, they are often discussed as if they are the same, but they are not. Any flow may be described in terms of a rotating frame, as if it is viewed by an observer rotating at a finite angular velocity, but that does not imply that the flow itself is rotating. The flow does not care what the observer is doing, and the invariants of the flow should remain independent on the reference frame. In turbulent flow, two invariants are the turbulent kinetic energy and the scalar dissipation rate. The production of k must then also be frame indifferent. For homogeneous, incompressible flow, the production of k is expressed by:

$$P^k = -\overline{\rho} k \left(b_{ij} + \frac{2}{3}\delta_{ij} \right) S_{ij} \tag{8.22}$$

Since all of the terms comprising the right-hand-side of the above equation, except for the anisotropy tensor, are by definition frame indifferent, it is clear that the expression for b_{ij}

should also be frame indifferent to be physically accurate. The modified rate-of-rotation term in W_{ij}^{*} (equation 8.19) is:

$$\Omega_{ij} + \frac{(C_4 - 4)}{(C_4 - 2)} e_{mji}\omega_m \tag{8.23}$$

Except in the limit that C_4 goes to infinity, the above expression is not frame indifferent. Therefore, in the Gatski and Speziale (1993) model, there is an explicit dependence of b_{ij} on the rotation of the reference frame, a non-physical result.

Usually, when rotation is discussed it is the rotation rate of a fluid particle about its own axes that is being referenced. Mathematically, this quantity is defined in Equation 8.21. Experimental studies, such as the work of Johnson et al. (1972), have shown that turbulence exhibits a sensitivity to "flow rotation" that is uniquely different from the "fluid rotation" defined above. Consider a simple two-dimensional channel flow in which the channel is attached to a plate rotating at a constant angular velocity (such as a merry-go-round). The flow rotation is simply equal to the rotation rate of the plate everywhere in the channel, and it is obviously independent of the local fluid rotation rate. However, in general, the flow rotation rate is not so obvious. It is necessary to find a method to resolve the flow rotation rate in terms of local parameters only, and the approach must be Galilean invariant and frame independent. These requirements are met by the use of the Lagrangian rate-of-rotation of the mean strain-rate tensor in an inertial frame.

A flow with curved streamlines in an inertial frame may also exhibit a flow rotation rate. Consider two-dimensional flow along a streamline with constant radius-of-curvature, R. When viewed in an inertial (Cartesian) frame, the mean strain rate tensor is rotating at a rate U_t/R, where U_t is the tangential velocity of a particle moving along the

streamline. This implies that the curved streamline flow in an inertial frame exhibits flow rotation, and an analogy may be seen between curved flows and rotating flows. However, it is important to note that not all flows with curved streamlines exhibit flow rotation. An example of a flow with zero flow rotation is two-dimensional stagnation point flow, despite the fact that the streamlines are curved in the vicinity of stagnation.

With a new definition for the flow rotation, Walters (2000) derived an alternate form of the algebraic stress model that is frame indifferent and correctly includes the influence of rotation and curvature on the turbulence field. The starting point is the same as for the Gatski and Speziale (1993) model, with the exception that the assumption of proportional convective transport (equation 8.4) is not utilized. The governing turbulence equations are cast into a reference frame rotating at the same rate as the local flow rotation. It is in this rotating frame that the condition of quasi-equilibrium (equation 8.14) must be invoked in order to obtain a frame indifferent result. Through the same solution method of Speziale and Gatski (1993), Walters (2000) was able to obtain the following new ASM formulation for b_{ij}:

$$b_{ij} = \frac{\left(\frac{4}{3} - C_2\right)}{\left(C_3 - 2\right)} \cdot \frac{6}{\left(3 - 2\eta^2 + 6\zeta^2\right)} \cdot \left[S_{ij}^* + \left(S_{ik}^* W_{kj}^* + S_{jk}^* W_{ki}^*\right) - 2\left(S_{ik}^* S_{kj}^* - \frac{1}{3} S_{kl}^* S_{kl}^* \delta_{ij} \right) \right] \quad (8.24)$$

where,

$$\eta^2 = S_{ij}^* S_{ij}^* \quad (8.25)$$

$$\zeta^2 = W_{ij}^* W_{ij}^* \quad (8.26)$$

$$S_{ij}^* = \frac{1}{2} g \frac{k}{\varepsilon} (2 - C_3) S_{ij} \quad (8.27)$$

$$W_{ij}^{*} = \frac{1}{2} g \frac{k}{\varepsilon} (2 - C_4) \left[\Omega_{ij} + \frac{(C_4 - 4)}{(C_4 - 2)} e_{mji} \omega_m \right] \tag{8.28}$$

It is important to note that the relative rotation rate tensor, Ω_{ij}, is calculated in a reference frame that is rotating at the local flow rotation rate, ω_m, and not in an arbitrarily rotating frame as in the Gatski and Speziale (1993) model. The influence of flow rotation, from either system rotation or streamline curvature, therefore enters the model via the term W_{ij}^{*} (equation 8.28).

The algebraic stress model discussed above may be adapted into an eddy-viscosity-based model with some additional modeling assumptions and mathematical manipulation. Since the Boussinesq assumption is to be employed, the anisotropy tensor must be expressed by a linear relationship to the mean rate-of-strain tensor. This can be accomplished by eliminating the higher order terms in equation 8.24, to give:

$$b_{ij} = \frac{\left(\frac{4}{3} - C_2 \right)}{(C_3 - 2)} \cdot \frac{6}{\left(3 - 2\eta^2 + 6\zeta^2 \right)} \cdot S_{ij}^{*} \tag{8.29}$$

Equations 8.27 and 8.20 can be used to substitute for S_{ij}^{*} in the above equation, resulting in the following expression for the anisotropy tensor:

$$b_{ij} = \frac{4 - 3C_2}{\left(3 - 2\eta^2 + 6\zeta^2 \right) \left[\left(\frac{C_1}{2} - 1 \right) + \frac{P^k}{\varepsilon} \right]} \cdot \frac{k^2}{\varepsilon} \cdot S_{ij} \quad , \tag{8.30}$$

where η^2 and ζ^2 are defined as in equations 8.25 and 8.26. Recall from Chapter 5 that the turbulent viscosity, μ_T, for a k-ε model is given by

$$\mu_T = C_\mu \rho \frac{k^2}{\varepsilon} \quad , \tag{8.31}$$

and for the "standard" model, C_μ is a constant. Substituting the Boussinesq formulation for b_{ij} into the above equation and rearranging, a function may be developed for C_μ :

$$C_\mu = \frac{k\left(4-3C_2\right)}{\left(6-4\eta^2+12\zeta^2\right)\left[\left(\frac{C_1}{2}-1\right)+\frac{P^k}{\varepsilon}\right]} \tag{8.32}$$

The above equation represents an eddy-viscosity approximation to an ASM that is sensitized to flow rotation and/or streamline curvature effects. The expression is not explicit in C_μ since the production of k appears on the right-hand-side, and production depends on μ_T and therefore C_μ. Also, the model cannot be used in the above form because there is a singularity that exists when the strain rate becomes large (increasing η^2) and rotation rate remains small.

An expression for C_μ that does not suffer from either of the problems discussed above can be obtained. The definition for production of turbulence is employed:

$$\frac{P}{\varepsilon} = \frac{\nu_T S^2}{\varepsilon} = C_\mu\left(\frac{Sk}{\varepsilon}\right)^2 \tag{8.33}$$

The parameter η^2 can also be written in terms of Sk/ε, which is the ratio of the strain rate to the turbulent time scale. Similarly, ζ^2 can be expressed in terms of Wk/ε, or the ratio of the flow rotation rate to the turbulent time scale. After some manipulation to eliminate negative terms on the right-hand-side that could result in singularities, the result is:

$$C_\mu = \frac{K_1 + K_2 C_\mu\left(\frac{Sk}{\varepsilon}\right)^2 + K_3 C_\mu\left(\frac{Sk}{\varepsilon}\right) + K_4 C_\mu^2\left(\frac{Sk}{\varepsilon}\right)^3}{K_5 + K_6 C_\mu\left(\frac{Sk}{\varepsilon}\right)^2 + K_7 C_\mu^2\left(\frac{Sk}{\varepsilon}\right)^4 + K_8\left(\frac{Wk}{\varepsilon}\right)^2} \quad , \tag{8.34}$$

where

$$S = \sqrt{2S_{ij}S_{ij}} \tag{8.35}$$

$$W = \sqrt{2W_{ij}W_{ij}} \tag{8.36}$$

$$W_{ij} = \Omega_{ij} + \frac{(C_4 - 4)}{(C_4 - 2)} e_{mji}\omega_m \tag{8.37}$$

From the ASM formulation, the constant C_4 is taken to be 0.4. As before, the mean fluid rotation tensor, Ω_{ij}, is computed in a reference frame rotating with the flow rotation rate, ω_m. While equation 8.34 it is not explicit, it is convergent, and may be computed through successive iterations. This is ideally suited for an implicit solver, but it may also be employed in a time-resolved explicit solver by adding a loop in the code to "pre-converge" C_μ.

The formulation for C_μ in equation 8.34 is, in theory, ready to be implemented into a k-ε model, and it was tested in this form by Walters (2000) with good results for a limited range of problems. In practice, however, one major difficulty remains. The flow rotation, or the rate-of-rotation of the principle axes of the strain-rate tensor, ω_m, in the definition of W_{ij} (equation 8.37) contains second (spatial) derivatives of the velocity. This term depends on the rate of change of components of the strain-rate tensor seen by a fluid particle traveling along in the flow, so ω_m is a function of the material derivative of the strain-rate tensor:

$$\frac{DS_{ij}}{Dt} = \frac{dS_{ij}}{dt} + u_k \frac{dS_{ij}}{dx_k} \tag{8.38}$$

The second derivatives of velocity are contained in the last term on the right-hand-side of the above equation. For example:

$$\frac{DS_{11}}{Dt} = \frac{D}{Dt}\left(\frac{\partial U_1}{\partial x_1}\right) = U_1 \frac{\partial^2 U_1}{\partial x_1^2} + U_2 \frac{\partial^2 U_1}{\partial x_1 \partial x_2} \quad . \tag{8.39}$$

The second derivatives enter directly in the calculation of the turbulent viscosity. This feature often causes a problem when used with a complex geometry requiring non-uniform, multi-topology, and/or unstructured meshes because the calculated second derivative fields are “noisy” (not smooth). This is a common trait of numerically-approximated higher-order derivatives, and researchers, such as Shur et al. (2000), have discussed the difficulties with second derivatives in a model in the literature. Figure 8.1 shows the cell values of the second derivative $\partial^2 U / \partial y^2$ on the midspan plane in the C3X vane conjugate heat transfer simulation. The values were taken the fully-converged solution with the realizable *k*-ε turbulence model. It is clear that, especially in the unstructured-type cell zones, values for the second derivative vary significantly from one cell to its neighbor. In fact, near the airfoil surface in the triangular prism cell zone, the variation is observed to exceed 10^7 $m^{-1}s^{-1}$ where red and blue cells are adjacent in Figure 8.1. This noise in the second derivatives can cause the unrealistic appearance of spurious turbulent kinetic energy, contaminating the results. From the experience of the author and of other researchers in the ACRL, equation 8.34 in its form above with the exact calculation of ω_m will only produce realistic results for simple two-dimensional flows with structured-type, ultra-high quality numerical grids. Any other complex flows with unstructured meshes need a smoothing function to condition the second derivatives, and the level of smoothing is very problem-dependent. Obviously this is not a desirable feature for use in a general-purpose solver intended to be applied to a variety of problems which may require multi-block, unstructured grids that are not of “perfect” quality everywhere in the domain.

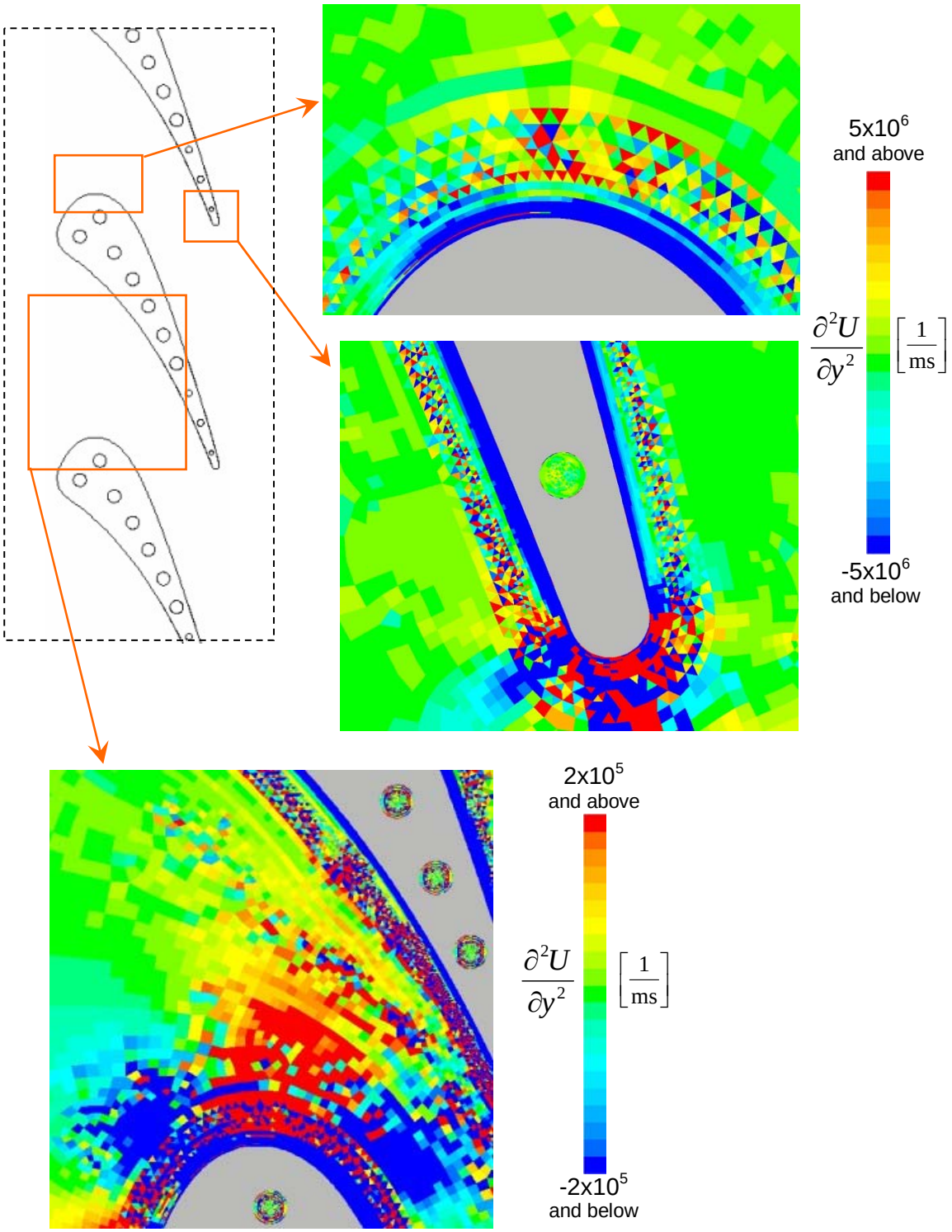

Figure 8.1 Cell values for second-derivative $\partial^2 U/\partial y^2$ on the midspan plane from the C3X vane conjugate heat transfer simulation. This is the fully-converged solution with the RKE turbulence model. The observed roughness in the second derivative field leads to difficulties when they are used in the calculation of the eddy-viscosity.

A new expression will be developed in which the flow rotation rate is approximated, rather than calculated exactly, in order to eliminate the second derivatives in the calculation of C_μ. It is assumed, for the purpose of approximating the rotation term only, that the local flow conditions correspond to two-dimensional, simple shear flow in a frame rotating with the flow. This turns out to be a reasonable assumption for most engineering flows in which curvature and/or rotation effects are important. It is applicable to most boundary-layer flows in which small gradients exist in the transverse direction, such as the C3X airfoil studied in this work, and also to many detached shear-layer flows. For this assumed condition, the velocity gradient tensor in the frame rotating with angular velocity ω can be written as

$$\frac{\partial U_i}{\partial x_j} = \begin{bmatrix} 0 & S \\ 0 & 0 \end{bmatrix} , \tag{8.40}$$

and the rate-of-rotation tensor in the rotating frame is

$$\Omega_{ij} = \begin{bmatrix} 0 & S/2 \\ -S/2 & 0 \end{bmatrix} . \tag{8.41}$$

In the inertial frame, the velocity gradient tensor for this same case is:

$$\frac{\partial U_i}{\partial x_j} = \begin{bmatrix} 0 & S+\omega \\ -\omega & 0 \end{bmatrix} , \tag{8.42}$$

where the strain-rate magnitude is equal to S in both frames. The rotation-rate tensor in the inertial frame is then given by:

$$\Omega_{ij} = \begin{bmatrix} 0 & S/2+\omega \\ -S/2-\omega & 0 \end{bmatrix} \tag{8.43}$$

The rotation-rate magnitude is

$$\Omega = \sqrt{2\Omega_{ij}\Omega_{ij}} = S + 2\omega \tag{8.44}$$

The above equation is solved for the rotation rate of the frame, which in this case is equal to the rotation rate of the principle axes of the rate-of-strain tensor, ω_m, giving

$$\omega_m = \frac{1}{2}(\Omega - S) \quad . \tag{8.45}$$

So, for the assumed condition of two-dimensional shear flow, the frame rotation rate may be found with knowledge of the rotation-rate magnitude, Ω, and the strain-rate magnitude, S, both computed in an inertial frame. Equations 8.41 and 8.44 are substituted into equation 8.37 to get W_{ij}. The magnitude of this tensor is computed (equation 8.36), and the following expression is obtained for W:

$$W = \left| S \cdot \left(1 - \frac{C_4 - 4}{C_4 - 2} \right) + \Omega \cdot \left(\frac{C_4 - 4}{C_4 - 2} \right) \right| \tag{8.46}$$

Since C_4 is taken to be equal to 0.4 from the original algebraic stress model, the final form of the rotational term is:

$$W = \left| \frac{9}{4}\Omega - \frac{5}{4}S \right| \tag{8.47}$$

This simple formulation for W goes directly into equation 8.34 for computation of C_μ, and it presents no difficulties during the solution process since the rotation-rate and strain-rate magnitudes contain only first derivatives of the velocity.

The final step in the model development is the determination of the model constants in equation 8.34. The coefficient K_8 on the rotational term is related to the constant C_3 in the pressure-strain correlation (equation 8.10) of the Speziale and Gatski (1993) RSM as follows:

$$K_8 = \frac{1}{2}(2 - C_3)^2 = 3.84 \tag{8.48}$$

Reasonable ranges for the other constants may also be determined from the RSM in a similar fashion. However, to ensure the model satisfies the realizability constraints for the turbulent stresses, the constants K_1 through K_7 were tuned to match the behavior of the realizable k-ε (RKE) model of Shih et al. (1995) in a non-rotating flow. The RKE model has been proven in the ACRL to perform superior to most "standard" two-equation models, although, like other two-equation models, it does not have the correct sensitivity to streamline curvature or rotation. Therefore, by matching the RKE behavior of C_μ for non-rotating flows, the new model will take the distinguishing feature of the RKE model and add to it the missing physics for curvature/rotation. A thorough iterative procedure based on the least-squares approach led to a set of constants giving a best-fit to the RKE data for C_μ as a function of Sk/ε. The result is plotted in Figure 8.2 along with the RKE curve. Note the close agreement and that both curves asymptotically approach zero as Sk/ε goes to infinity. All model constants in equation 8.34 are listed in Table 8-1.

Table 8-1 Model constants in equation 8.34.

K_1	0.66
K_2	3.9
K_3	1.0
K_4	5.3
K_5	2.9
K_6	17.0
K_7	10.0
K_8	3.84

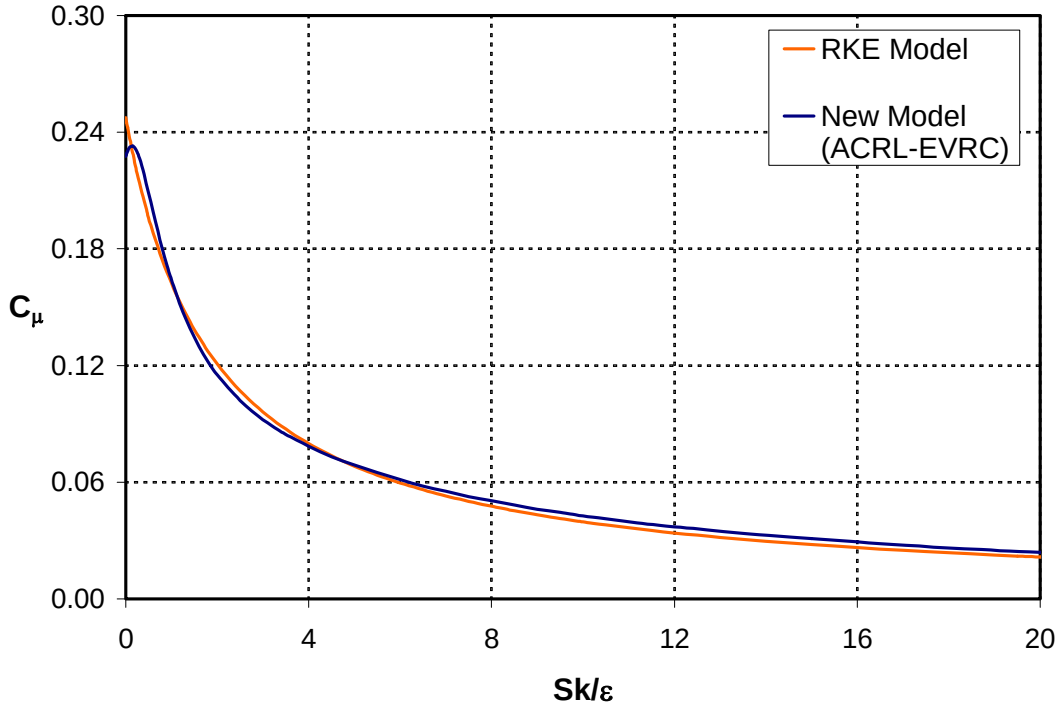

Figure 8.2 Behavior of C_μ as a function of the turbulent time-scale ratio for non-rotating flow shows the equivalence of the new model and the realizable k-ε model for this case.

To demonstrate the sensitivity of the new eddy-viscosity formulation to flow rotation, consider the simple test case of homogeneous, plane shear defined by S=1 that is rotating at a rate ω_r, as illustrated in Figure 8.3. The turbulence will develop with time starting from the initial conditions k_0=1 and ε_0=0.296. The governing equations for this problem simplify to:

$$\frac{dk}{dt} = P^k - \varepsilon = C_\mu \frac{S^2 k^2}{\varepsilon} - \varepsilon \quad , \tag{8.49}$$

$$\frac{d\varepsilon}{dt} = C_{\varepsilon 1} P^k \frac{\varepsilon}{k} - C_{\varepsilon 2} \frac{\varepsilon^2}{k} = C_{\varepsilon 1} C_\mu S^2 k - C_{\varepsilon 2} \frac{\varepsilon^2}{k} \tag{8.50}$$

Using the new expression for C_μ, the above equations may be solved for k and ε with a numerical time-marching scheme, and this was accomplished in Excel spreadsheet.

Figure 8.4 presents the evolution of turbulence for the non-rotating case (ω_r=0). Even with no flow rotation, the new model shows better agreement with the large-eddy simulation (LES) benchmark data of Bardina et al. (1983) as compared to the standard k-ε model of Launder and Spalding (1972). For this case, the new model results are almost identical to the results with the realizable k-ε model. Figure 8.5 shows the results for a positive rotation rate ω_r=0.5S. Notice that the SKE model predicts the same result as the non-rotating case, thus indicating that it is not at all sensitized to rotation. The new model, while not matching the LES data exactly, does reproduce the trend. A negative rotation rate of ω_r=0.5S is stabilizing, and results for this case are plotted in Figure 8.6. The new model correctly predicts a decay of turbulence in time.

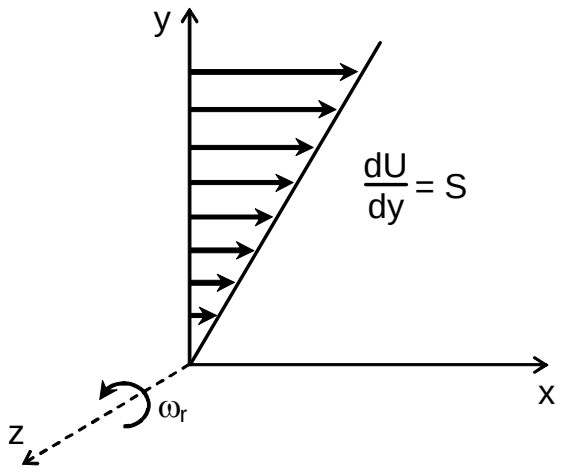

Figure 8.3 Illustration of rotating, homogeneous shear flow.

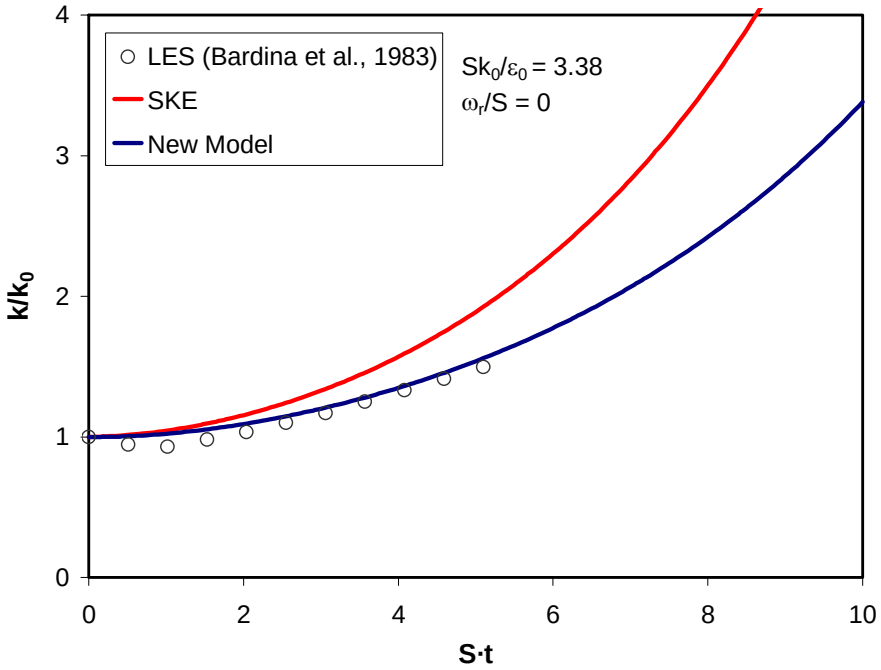

Figure 8.4 Evolution of turbulent kinetic energy in non-rotating homogeneous plane shear flow shows the improved predictive capability for the new eddy-viscosity model.

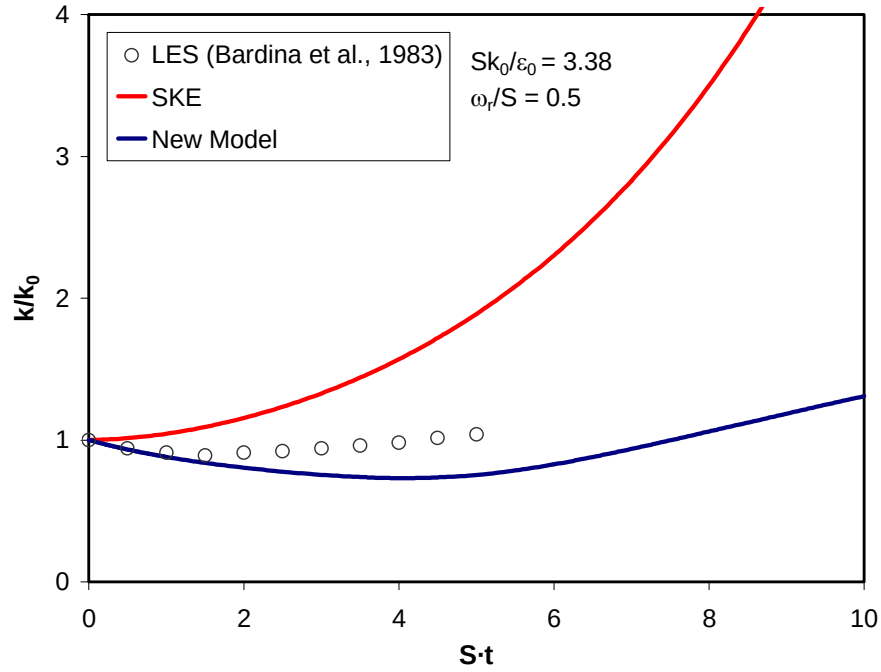

Figure 8.5 Evolution of turbulent kinetic energy in homogeneous plane shear rotating at $\omega_r=0.5S$. The energizing effect of this rotation is offset by an increase in dissipation. The behavior of the new model indicates it is sensitized to rotation.

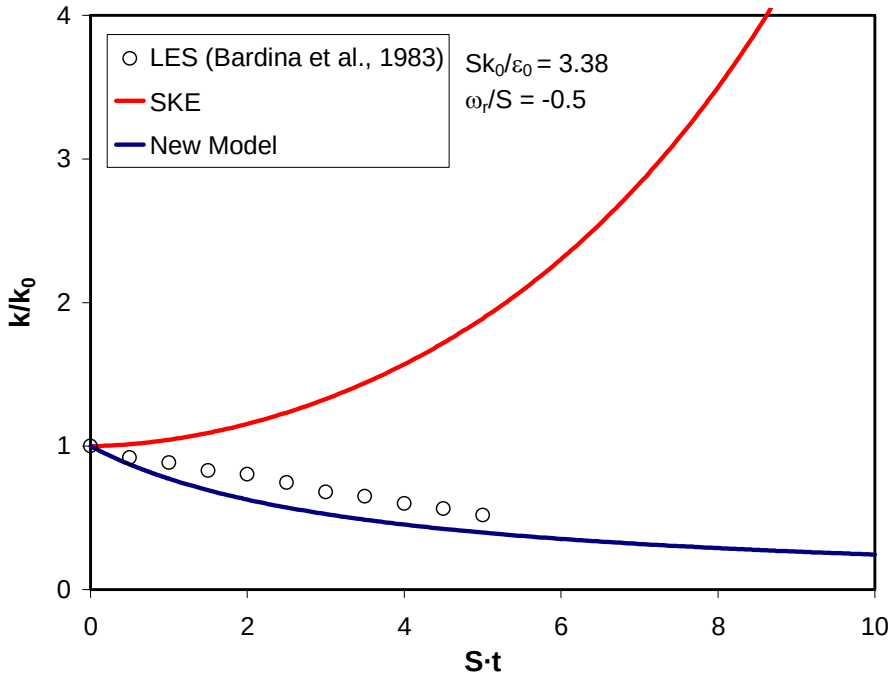

Figure 8.6 Evolution of turbulent kinetic energy in homogeneous plane shear rotating at ω_r=-0.5*S*. The new model correctly predicts a decay of turbulence due to the stabilizing effect of this rotation rate.

At this point, the new eddy-viscosity model is ready to be implemented in a general purpose code. Transport equations for *k* and ε complete the implementation, and these differential equations are exactly the same as in the standard and realizable *k*-ε models (equations 5.7 and 5.8). Note that the constants in the transport equation for dissipation of turbulent kinetic energy are unchanged from the standard model ($C_{\varepsilon 1}$=1.44, $C_{\varepsilon 2}$=1.92). The new model may be simply and efficiently implemented via user-defined functions in Fluent 6 code, and computational intensity is on the same order as the standard two-equation models. Note that the model is a "high-Reynolds number" model (where the Reynolds number is that of the turbulence), and it must be combined with a near-wall model in the wall regions. From this point forward, the new model will be

denoted “ACRL-EVRC”, with the first part representing the laboratory affiliation and the “EVRC” standing for “Eddy-Viscosity model sensitized to Rotation and Curvature.”

New Near-Wall Model

As discussed in Chapter 5, special treatment must be given to the turbulence modeling in the regions near solid boundaries since the turbulence structure is strongly affected by the presence of a wall. The two-layer model is adopted herein, because of its economy, sensible physics, and documented good performance for complex wall-bounded flows, especially when heat transfer predictions are desired. The two-layer model is used in conjunction with a grid that is very dense in the wall-normal direction (with the wall-adjacent node having $y^+<1.0$), allowing integration of all physical quantities down to the wall. The two-layer treatment developed for use with the ACRL-EVRC model is based on the original equations of Wolfstein (1969), but the present model incorporates a new “dynamic” length-scale limiter in order to adjust the near-wall zone size to the local conditions in a physically more sound way.

Recall that the two-layer model divides the flow into a far-field region, where a “high-Reynolds number” model, such as the new ACRL-EVRC, is applied, and a viscosity-affected near-wall layer. In the near-wall zone, a transport equation for the turbulent kinetic energy is solved in the high-Re form, and the dissipation rate is calculated from an algebraic relation that is a function of distance from the wall. In the model of Wolfstein (1969), the equations in the near-wall layer are:

$$\varepsilon = \frac{k^{3/2}}{l_\varepsilon} \tag{8.51}$$

$$l_\varepsilon = C_L y\left[1-\exp\left(\frac{-\mathrm{Re}_y}{A_\varepsilon}\right)\right] \tag{8.52}$$

$$\nu_T = C_\mu \sqrt{k}\cdot C_L y\left[1-\exp\left(\frac{-\mathrm{Re}_y}{A_\mu}\right)\right] \tag{8.53}$$

where Re_y is a turbulence Reynolds number for wall-bounded flows defined by:

$$\mathrm{Re}_y = \frac{\sqrt{k}\cdot y}{\nu} \quad , \tag{8.54}$$

and y is the smallest distance to the nearest wall. The constants A_ε and A_μ are taken to be 4.99 and 25.0, respectively.

Typically, the above equations for the near-wall region are applied anywhere in the flow domain where $\mathrm{Re}_y < 200$. This is the case in the Fluent code, as well as in most other commercial solvers. The approach of using a somewhat arbitrary Re_y for the cutoff may lead to difficulties in certain situations. For example, consider a region far from a wall where very small values of k exist, such as in low-speed, accelerating flow (i.e. plenum flow). In this case, the model incorrectly treats the zone as a near-wall region, and consequently the turbulent length scale is overestimated, and dissipation rate is severely underestimated. Consequently, the traditional two-layer approach leads to excessive turbulence production in these conditions. To allow the two-layer approach to be more robust for a variety of flows, a new length-scale limiter is employed to dynamically adjust the range of the near-wall zone.

From equation 8.53, the length scale of turbulence in the near-wall zone from the Wolfstein (1969) model is:

$$L_{T,nw} = C_L y \tag{8.55}$$

In the far-field, the length scale of turbulence from the high-Re form of the k-ε model is:

$$L_{T,ff} = \frac{k^{3/2}}{\varepsilon} \tag{8.56}$$

In the new two-layer model, both length scales are calculated at each grid point, and the minimum value is taken:

$$L_T = \text{MIN}\left(C_L y, \frac{k^{3/2}}{\varepsilon} \right) \tag{8.57}$$

When equation 8.55 is used for the length-scale formulation, the model recognizes that the grid point lies within the near-wall layer, and equations 8.51 through 8.53 are solved. This method seamlessly integrates the near-wall model into the high-Re model form by dynamically adjusting the cutoff length scale to the high-Re quantity, and it also eliminates anomalies where certain zones away from the wall may be incorrectly treated as a wall-layers.

A value for C_L can be obtained by assuming that turbulence variables achieve the following universal values when expressed in wall coordinates:

$$k = \frac{u^{*2}}{\sqrt{C_\mu}} \tag{8.58}$$

$$\nu^* = \frac{k^2}{\varepsilon} = \frac{u^* \kappa y}{C_\mu} \quad , \tag{8.59}$$

where u^* is the wall friction velocity and κ is the von Karman constant, equal to 0.41. In the above definitions, C_μ is taken to be equal to the equilibrium value of 0.09. To ensure that the matching between the freestream and near-wall length scale occurs in the inertial sublayer, the following is required:

$$L_T = \frac{\nu^*}{\sqrt{k}} = C_L y \tag{8.60}$$

Using equations 8.58 and 8.59, the following solution is obtained for C_L.

$$C_L = \frac{\kappa}{C_\mu^{0.75}} = 2.495 \tag{8.61}$$

To check the performance of the model, two-dimensional, fully-developed, non-rotating channel flow was simulated at two different Reynolds numbers using the ACRL-EVRC model with the new near-wall model. The Fluent 6 solver was used with streamwise periodic conditions to efficiently simulate fully-developed flow. The Reynolds number, Re_τ, is based on wall friction velocity and the channel half-height, h:

$$\mathrm{Re}_\tau = \frac{u^* h}{\nu} \tag{8.62}$$

Predictions for the velocity profiles are plotted in wall coordinates, defined by:

$$y^+ = \frac{u^* y}{\nu} \tag{8.63}$$

$$U^+ = \frac{U(y)}{u^*} \tag{8.64}$$

The first case was for Re_τ=395, and at this small Reynolds number, a relatively narrow inertial sublayer should exist. The predictions are plotted against Direct Numerical Simulation (DNS) data of Kim et al. (1987) in Figure 8.7, and good agreement is observed. Next, a high Reynolds number of Re_τ=39,500 is studied. For this case, the new model prediction, plotted in Figure 8.8, follows the universal "law-of-the-wall." The inertial sublayer is larger than the low-Re_t case, and the new model achieves the standard log-law behavior and also predicts a wake region above $y^+=10^3$. Results for this channel

Flow test case illustrate that the turbulence model with new near-wall treatment is physically realistic and is ready to be applied to more rigorous cases. Several of these more rigorous cases are simulated with the ACRL-EVRC model and discussed in the following chapter.

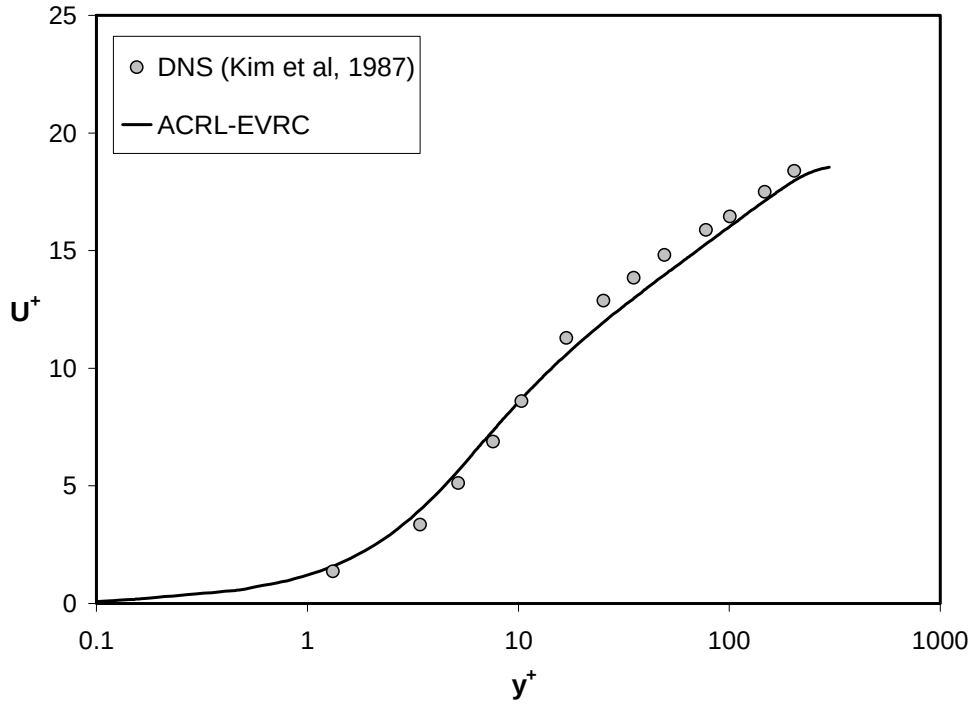

Figure 8.7 Prediction of velocity profile in fully-developed, non-rotating channel flow at Re_τ=395 using ACRL-EVRC turbulence model including new near-wall treatment. The new model shows good agreement with DNS data.

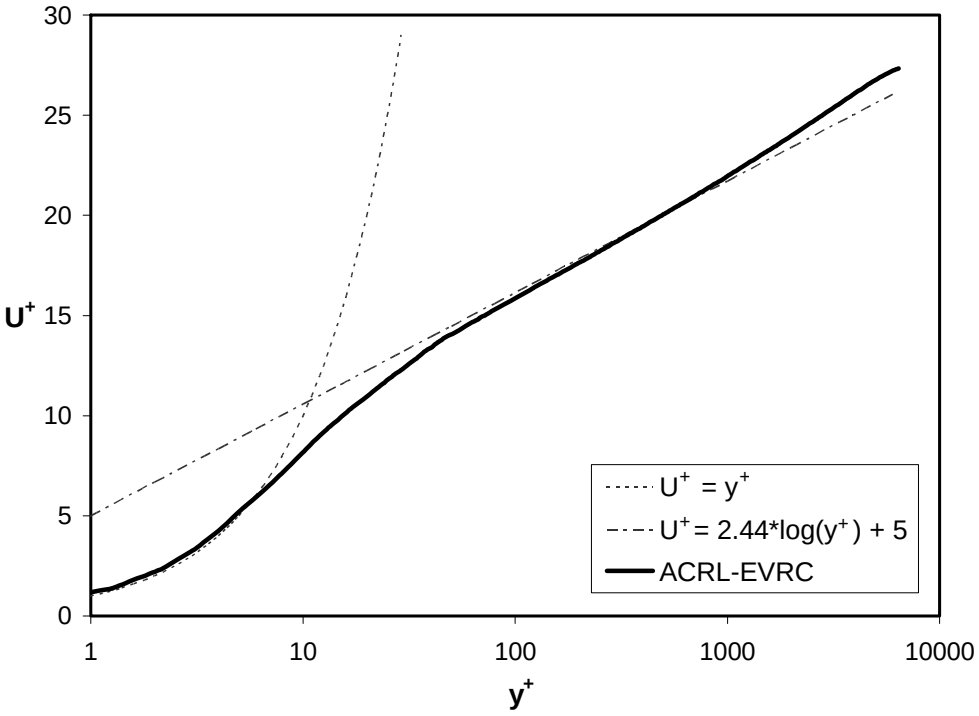

Figure 8.8 Prediction of velocity profile in fully-developed, non-rotating channel flow at Re_τ=39,500 using ACRL-EVRC turbulence model and new near-wall treatment. The new model shows good agreement with standard law-of-the-wall form.

CHAPTER 9

SIMULATIONS WITH NEW ACRL-EVRC TURBULENCE MODEL

The previous chapter detailed the development of a new physics-based, eddy-viscosity model that includes sensitivity to the effects of streamline curvature and system rotation. As originally intended, the final form of the ACRL-EVRC model is fairly straightforward and simple, prescribing the turbulent viscosity through an algebraic function of the mean strain rate magnitude and the mean fluid rotation rate magnitude, and it is implemented into the Fluent 6 solver via User-Defined Functions (UDFs). The UDFs are written in the C programming language, and contain macros supplied by Fluent, including "define variable" functions, "adjust (after each iteration)" functions, "execute (one time) on demand" functions, "user-defined scalars" (for which transport equations may be solved) and "user-defined memory" arrays. Because simulations with the new model retain the discretization scheme and the internal solver functionality of Fluent, comparison of results with "stock" models in Fluent will isolate the new model relative performance.

The present chapter discusses a series of pertinent simulations that employ the ACRL-EVRC model. The first cases – *rotating*, fully-developed channel flow and flow in a "U-bend" – are both two-dimensional and are designed to stress two different flow rotation situations. Both of these problems have applications in turbine airfoil internal cooling. The next case is the one of the most stringent test cases for a new turbulence model, and that is the revisiting of the conjugate heat transfer simulation of the three-dimensional (3D), internally-cooled C3X turbine vane at engine-realistic conditions.

Finally, to illustrate an important application of the new model in the context of the present work, a simulation is conducted to predict heat transfer in a sharp 180^o-turn of a 3D channel, characteristic of the bend in a turbine airfoil internal cooling circuit, commonly referred to as a serpentine passage.

Two-Dimensional Test Cases

The first simulation is a fairly straightforward case, but one that is very important in testing model sensitivity to flow rotation. Two-dimensional, fully-developed flow in a straight channel is subjected to a constant rotation rate, as if it was attached to a "merry-go-round." The computations were based on the exact conditions of Direct Numerical Simulations (DNS) of Kristoffersen and Andersson (1993), and a schematic of the case is shown in Figure 9.1. This problem was simulated in Fluent, and the computational domain consisted of a very short section of the channel in the primary flow direction, since a streamwise periodic boundary condition could be used for the fully-developed condition. The Reynolds number based on wall friction velocity (equation 8.53), with the

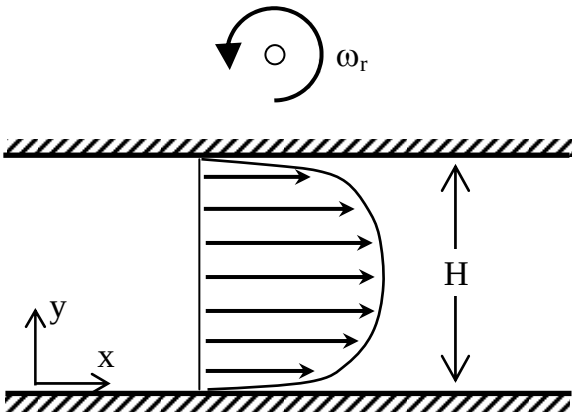

Figure 9.1 Diagram of rotating, fully-developed, turbulent channel flow.

channel half-height ($H/2$) as the length scale, was Re_τ=194 in all cases. The rotation rate is expressed in terms of a dimensionless rotation number, $Ro = \frac{\omega H}{U_m^2}$, where ω is the actual rotation rate in rad/s and U_m is the average velocity across the channel. Simulations were carried out for Ro=0 (non-rotating reference case), Ro=0.05, and Ro=0.5, using both the new ACRL-EVRC model and the standard *k*-ε model.

Velocity profiles for the reference case with zero rotation are shown in Figure 9.2. The ACRL-EVRC model shows excellent agreement with the symmetric DNS profile, even slightly better than the SKE model. This implies that the new near-wall treatment is physically accurate, since much of the channel lies in the near-wall zone at this low Reynolds number. Because the flow is fully-developed, and there is no transverse

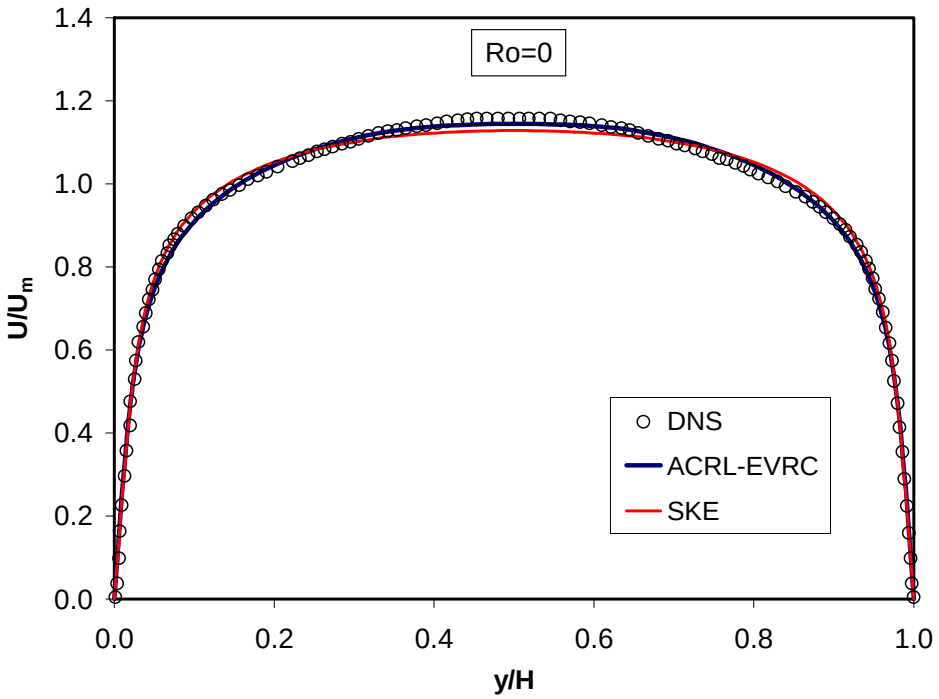

Figure 9.2 Velocity profiles for non-rotating (Ro=0) channel flow reference case.

component of velocity, there in no effect of system rotation *directly* on the mean flow. In fact, laminar, fully-developed flow will maintain a symmetric profile regardless of any imposed rotation. The turbulence is, however, affected by rotation, and any asymmetry in the turbulence across the channel will cause skewness in the mean velocity.

Figures 9.3 and 9.4 show the velocity and turbulent kinetic energy profiles, respectively, for a mild rotation rate of Ro=0.05. The turbulent kinetic energy is normalized by $k^+ = \frac{k}{u*^2}$. The DNS data shows that the velocity profile is becoming skewed with the rotation, and this is due to an asymmetric *k* profile. The ACRL-EVRC model correctly predicts the skewed velocity profile. The SKE model does not, which is not surprising since the model has no sensitivity to the flow rotation. The new model shows asymmetry in the turbulent kinetic energy, with reduced *k* near the suction surface (y/H=0) and augmented *k* near the pressure surface (y/H=1), although the turbulence level here is slightly underpredicted. Once again, the symmetric SKE profile for *k* indicates complete insensitivity to rotation.

As the rotation is increased to a relatively large level of Ro=0.5, the profiles for velocity and turbulent kinetic energy, shown in Figures 9.5 and 9.6, display strong asymmetry. The ACRL-EVRL model results show outstanding agreement with the DNS velocity profile. Qualitatively, the new model captures the skewness in the turbulent kinetic energy profile, although *k* is underpredicted near the suction surface and slightly overpredicted near the suction surface. For this case, it is very apparent that SKE is completely insensitive to rotation. Overall, the results with the new model for turbulent flow in a rotating channel are physically-realistic and encouraging.

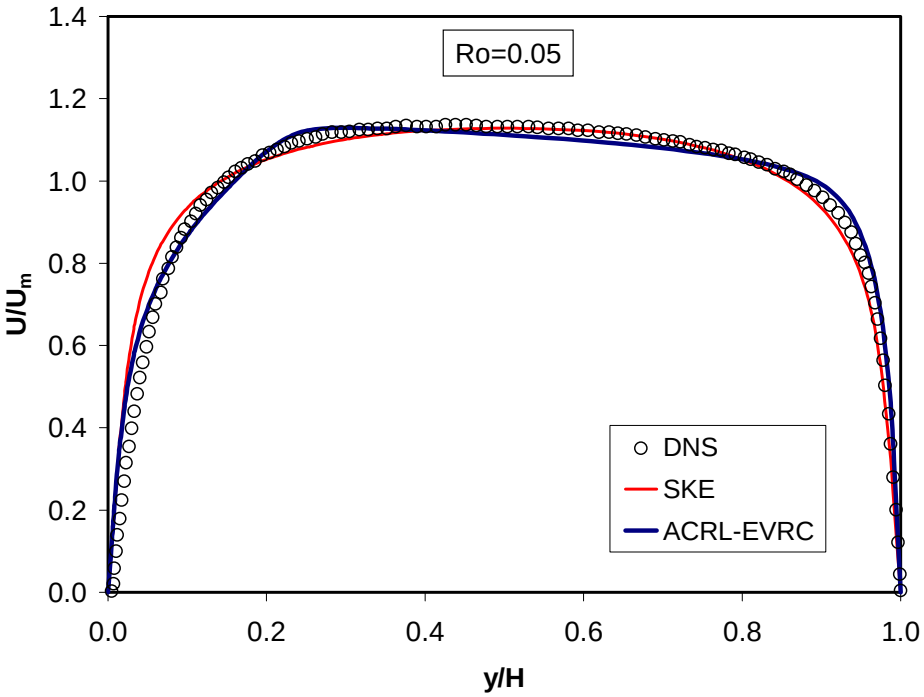

Figure 9.3 Velocity profiles for channel flow at a mild rotation rate of Ro=0.05 showing skewness accurately predicted by ACRL-EVRC.

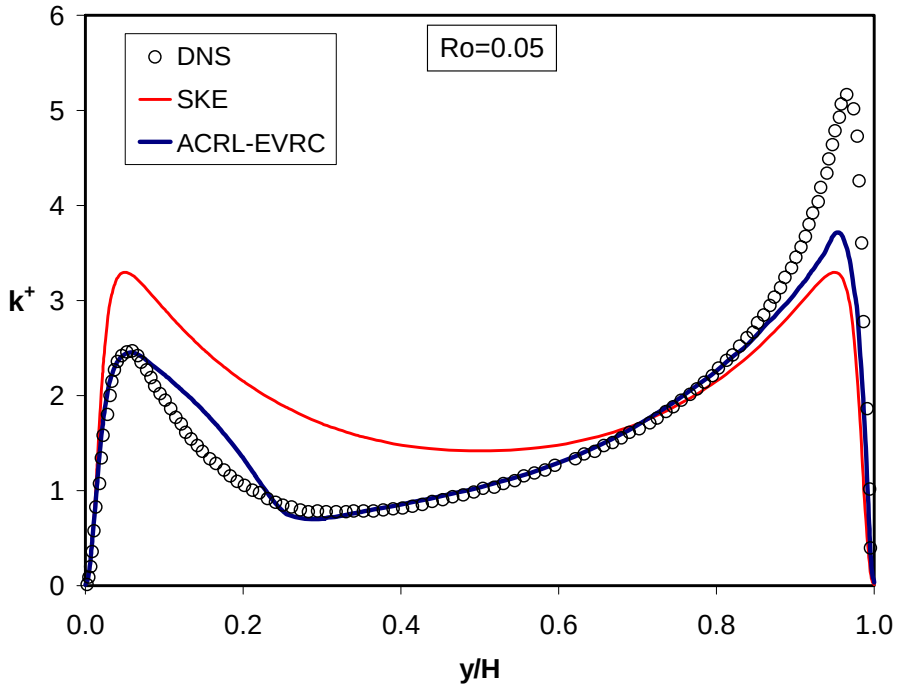

Figure 9.4. Turbulent kinetic energy profiles for channel flow rotating at Ro=0.05. The SKE model shows no sensitivity to the rotation.

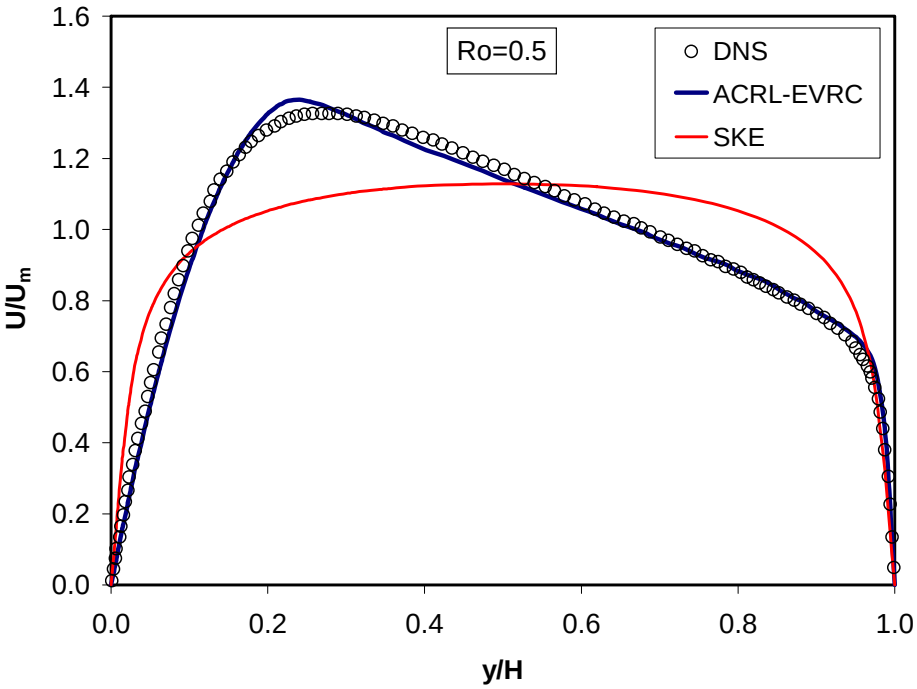

Figure 9.5 Velocity profiles for channel flow at a high rotation rate of Ro=0.5.

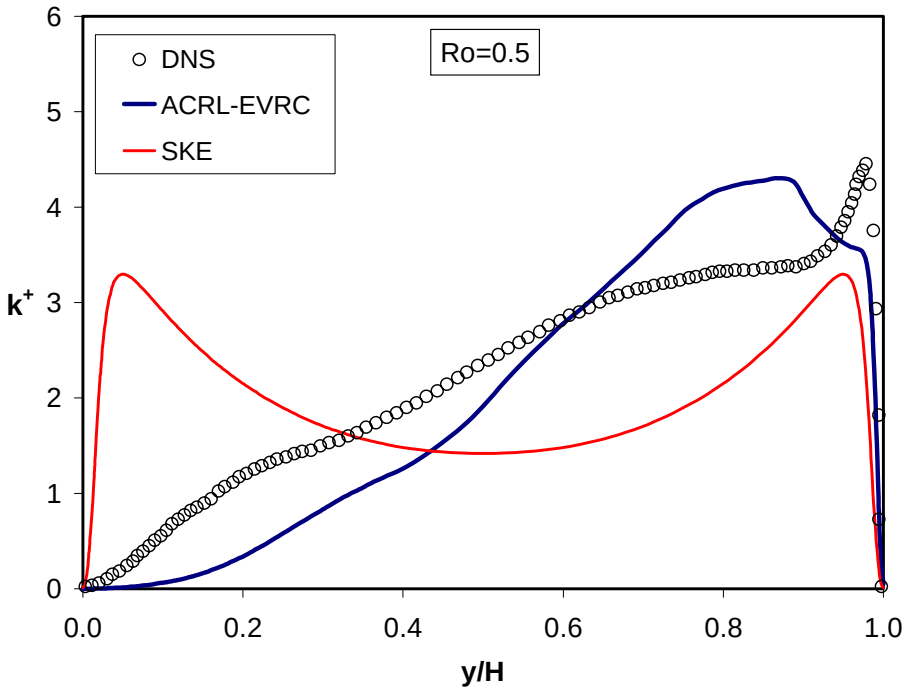

Figure 9.6 Turbulent kinetic energy profiles for channel flow with rotation number Ro=0.5.

The next simulation is designed to test the ability of the new ACRL-EVRC model to predict the effects of strong streamline curvature on the turbulence field. The problem consists of two-dimensional flow in a "U-bend" of constant channel height. In addition to the curvature, the problem includes strong acceleration, separation, and reattachment, and the somewhat simple-looking problem represents a challenging test case for turbulence models. The numerical simulation was designed to match the experimental conditions of Monson et al. (1990), which had a test section with a very large width such that sidewalls are expected to have negligible impact on the data measured at the midpitch. The radius of the turn (to the channel centerline) is equal to the channel height, H. The computational domain is shown in Figure 9.7. A view of the computational mesh in the turn region is presented in Figure 9.8.

The Reynolds number based on the mean velocity and the channel height was $Re_H=10^6$. Inlet conditions in the computation were prescribed to match the experimental profiles for mean streamwise velocity and turbulent kinetic energy at $s/H=0$, and these profiles are shown in Figure 9.9. Note that y is the wall-normal direction and is always

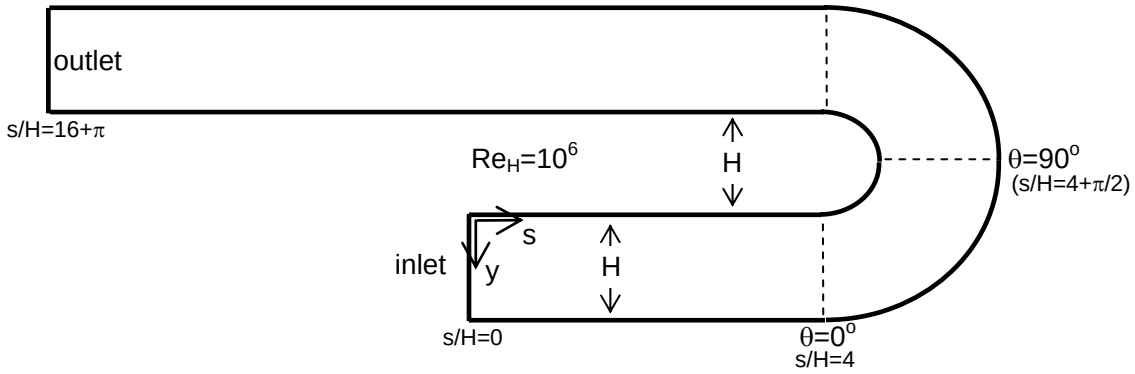

Figure 9.7 Computational domain for two-dimensional U-bend simulation.

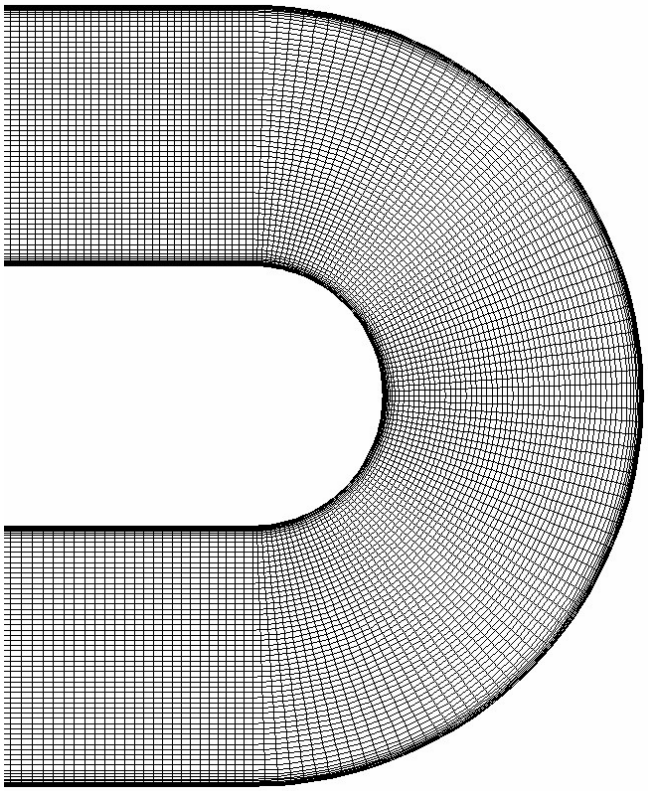

Figure 9.8 Closeup view of high-density numerical mesh in the U-bend simulations.

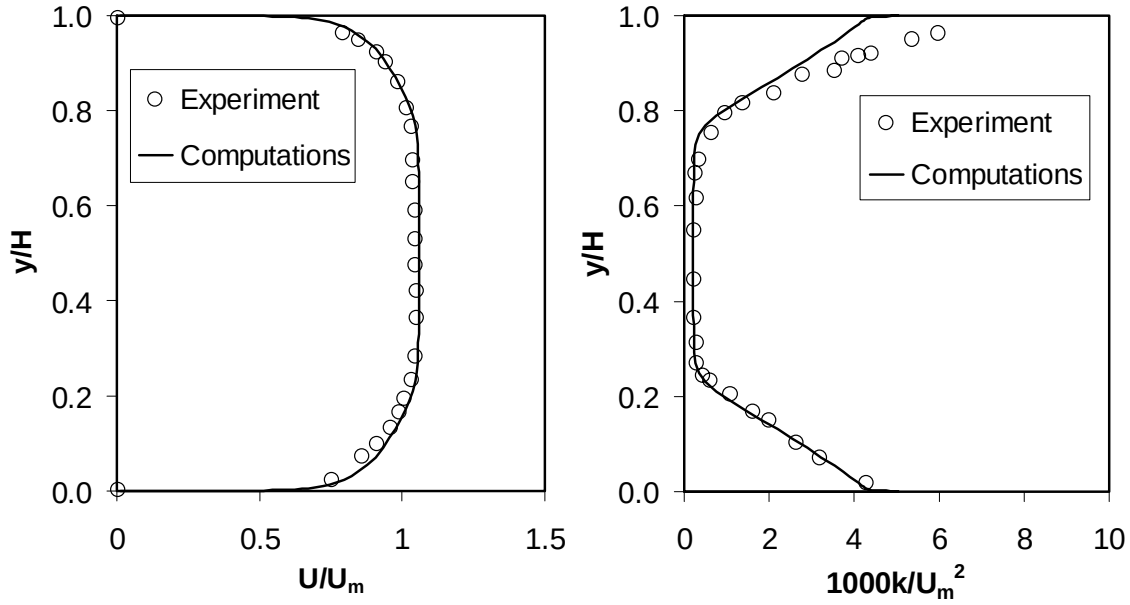

Figure 9.9 Profiles of normalized velocity and turbulent kinetic energy at the inlet of the computational domain indicating a match of the experimental measurements.

measured from the inside surface to the outside surface. It is apparent that the flow has not yet reached fully-developed conditions as it nears the bend section. Simulations were conducted for the ACRL-EVRC model, the standard k-ε model, and the realizable k-ε model. All experimental data presented for this case is from Monson et al. (1990).

Figure 9.10 shows flow development in the bend section at $\theta=90^o$ (halfway through the end) in terms of the streamwise velocity and the turbulent kinetic energy profiles, both normalized by the average velocity across the channel, U_m. Looking at the profiles for turbulent kinetic energy first, it is observed that the experiments show a significant increase in k near the outer surface (y/H=1) and a decrease in k near the inner surface (y/H=0). This is because the concave curvature has a destabilizing effect on turbulence, while concave curvature has a stabilizing effect. The behavior in response to the streamline curvature along the outer and inner walls is analogous to the response on the pressure and suction surfaces, respectively, for the rotating channel case discussed above. The SKE model shows no sensitivity to the curvature, with a nearly symmetric profile for k, while the RKE model shows only a slight response. Only the ACRL-EVRC model qualitatively predicts the profile for k, correctly matching the shape and location of the peak near the outer surface. The elevated turbulence has an impact on the mean flow near the outside wall, and only the new model predicts a "full" profile for U that matches the measured data. Both SKE and RKE fall short near the outer surface.

Figure 9.11 shows the profiles for normalized U and k at $\theta=180^o$, the exit to the U-bend section. Experiments show a flow separation zone, with negative velocity, near the inside surface. The SKE model predicts excess turbulence near y/H=0, despite the natural tendency of the convex curvature to reduce k. Because of the excess momentum

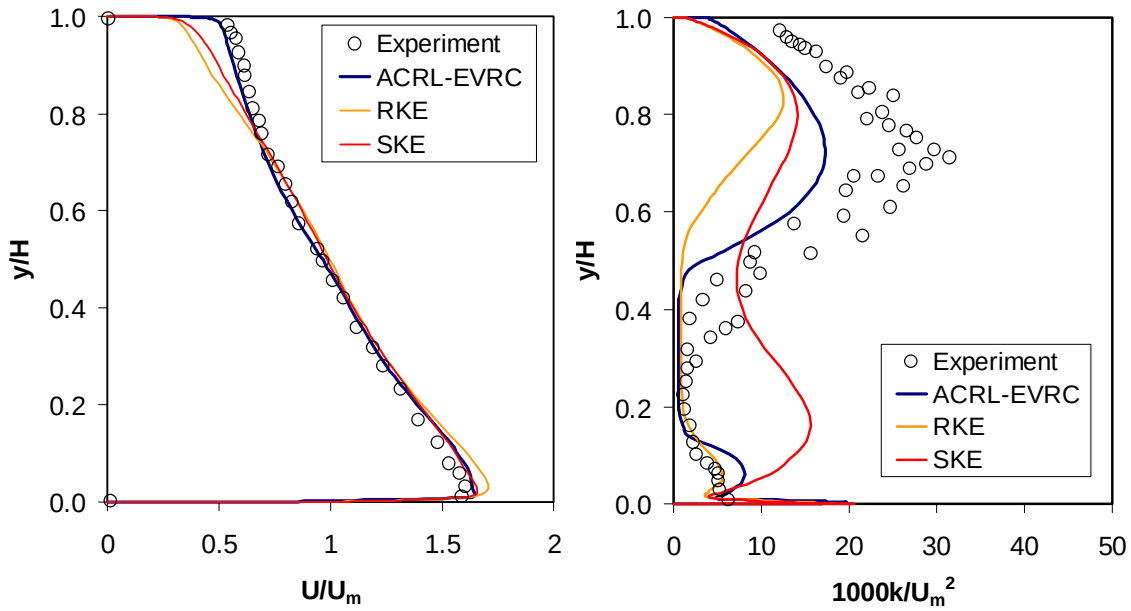

Figure 9.10 Profiles of velocity and turbulent kinetic energy at θ=90° in the U-bend show that the ACRL-EVRC model is better able to capture augmented turbulence near the outer surface and its effect on the mean velocity.

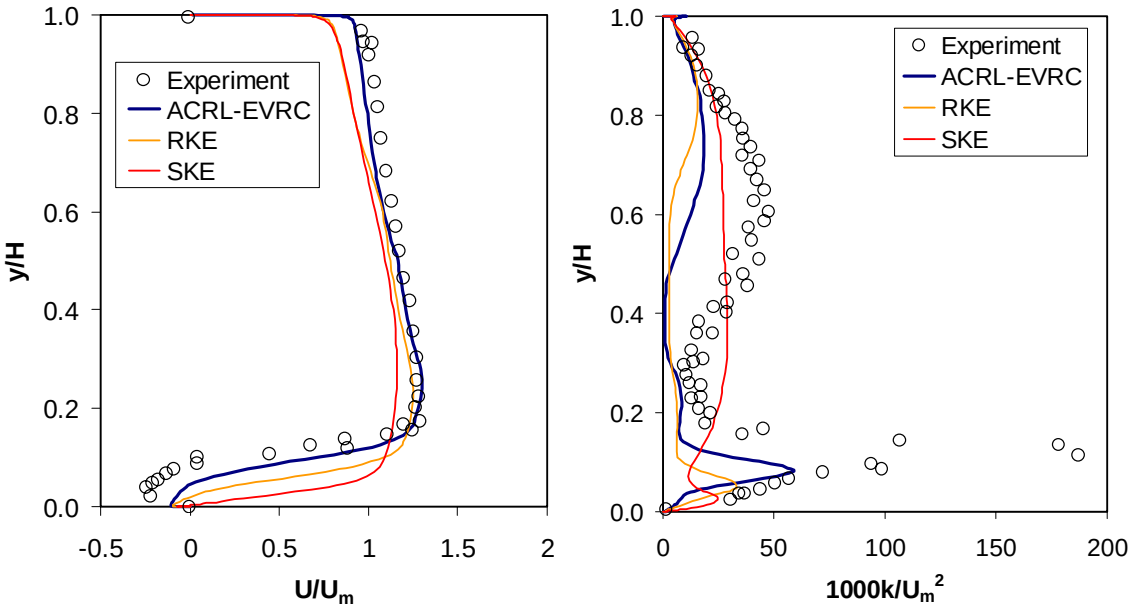

Figure 9.11 Profiles of velocity and turbulent kinetic energy at θ=180° (end of U-bend section) showing the ability of ACRL-EVRC to best capture the separated flow and elevated turbulence near the inside surface.

transport due to artificially high levels of k here, SKE indicates no separation at all. The RKE model shows a very slight separation. The ACRL-EVRC model correctly predicts separation and is closest to the measured values. A large peak in k near the inside wall corresponds to the location of the shear layer between the recirculation zone and the high-speed flow above it. The ACRL-EVRC is the only model that correctly finds the location of the peak, although all models underpredict the magnitude. The author believes that this is primarily due to the presence of unsteady effects in the experiment that are not resolved in the steady experiments, however this effect was not investigated because this was meant to be a test case focusing on curvature effects.

The response of the turbulence to the curvature is evident the contours of turbulence level,

$$TL = \frac{\sqrt{\frac{2}{3}k}}{U_m} \cdot 100 \ (\%) \quad , \tag{9.1}$$

for the three different models, shown in Figure 9.12. The ACRL-EVRC case clearly shows augmented turbulence levels along the concave outer wall, increasing through the bend as the destabilizing curvature continues. The RKE model shows a slight increase in TL along the outer surface, even though this model was not designed specifically to handle curvature. The standard *k*-ε model has no response to the curvature. The contours are characterized by high levels of turbulence across the channel by midway through the turn due to an incorrect response to the high strain rate. The high momentum transport due to this predicted turbulence delays separation on the convex side and reduces the size of the separated zone.

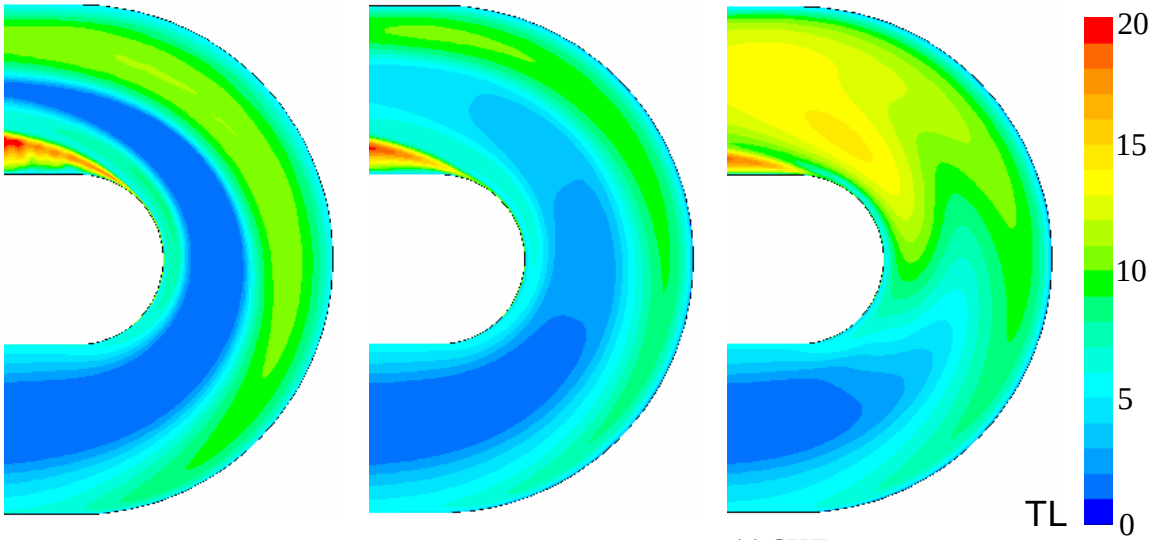

(a) ACRL-EVRC **(b) RKE** **(c) SKE**

Figure 9.12 Contours of turbulence level in the U-bend with (a) ARCL-EVRC model, (b) RKE model, and (c) SKE model. The new model responds to the destabilizing effect of concave curvature by predicting augmented turbulence production along the outer wall.

In Figures 9.13 and 9.14, predictions are presented for the skin friction coefficient,

$$C_f = \frac{\tau_w}{\frac{1}{2}\rho U_m^2} \tag{9.2}$$

for the inner and outer walls, respectively. The location of the curved section is between s/H=4 and s/H=(4+π), denoted by the dashed lines in the plots. The ACRL-EVRC model indicates a lower value for C_f on the inner wall in the bend, and this is in better agreement with the experiment than the other two models. This is an effect of the new model correctly predicting a decrease in turbulence along the inner, convex wall, which tends to reduce the wall shear stress. The opposite trend should be seen on the outer, or concave, wall, and indeed ACRL-EVRC predicts a higher skin friction in and after the bend, which

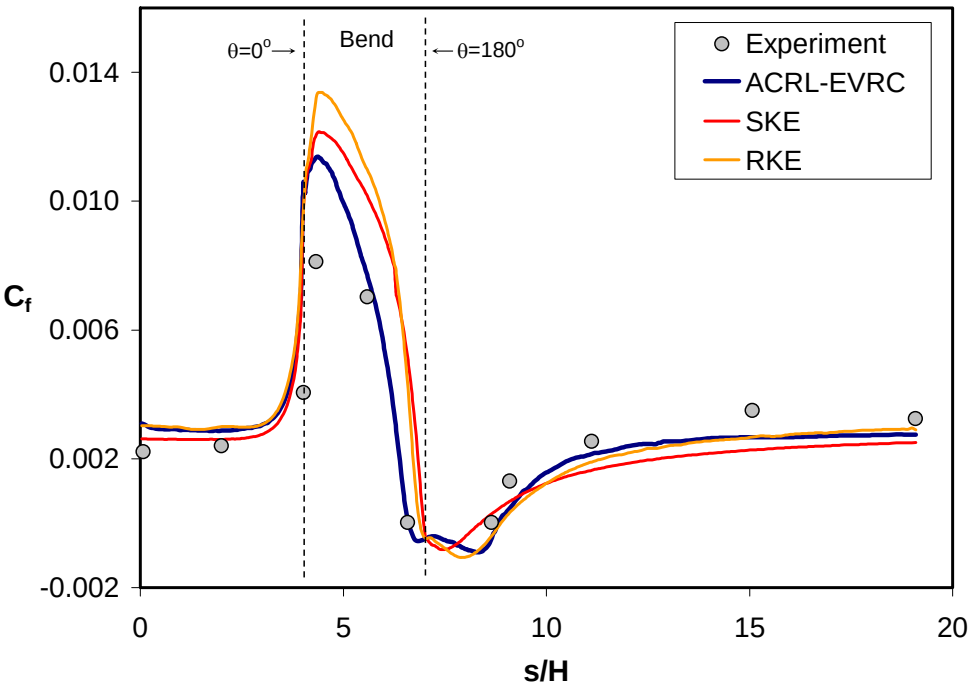

Figure 9.13 Distribution of the skin friction coefficient on inner wall of U-bend.

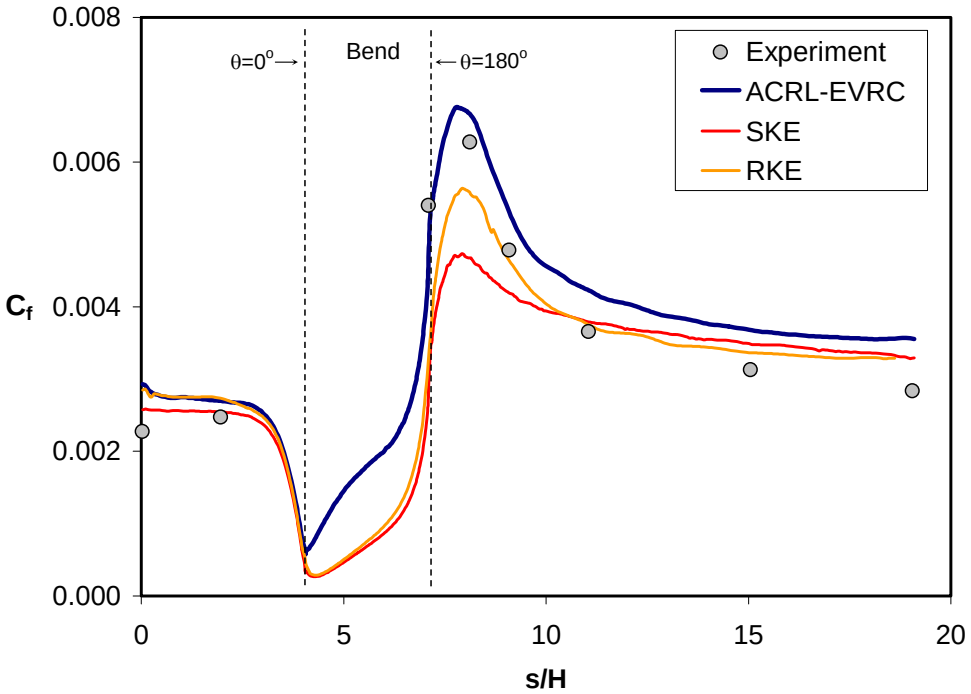

Figure 9.14 Distribution of the skin friction coefficient on outer wall of U-bend.

is in line with the measurements. The new model does slightly overpredict the friction well downstream of the bend (beyond s/H=10), and the author believes that this is due to a larger separation zone, and slower wake recovery that leads to a slightly higher velocity along the outside surface that the other models. In the experiment, the separated shear layer aft of the bend may be unsteady, but the simulations are not focused on this element. The overprediction of shear stress downstream is not a direct result of the curvature effects, as the model performs well in the turn.

Figure 9.15 and 9.16 show predicted and measured variations of the pressure coefficient,

$$C_p = \frac{p}{\frac{1}{2}\rho U_m^2} \tag{9.3}$$

on the inner and outer surfaces of the U-bend channel, respectively. All models perform well in predicting the static pressure distribution on the inner and outer surfaces through the bend. After the turn, the pressure predictions are mainly influenced by the size of the separation region. As might be expected, the SKE model shows the poorest agreement with measurements downstream, while the new model shows excellent agreement with the experiment aft of the bend on both walls.

Turbine Vane Conjugate Heat Transfer Simulation Revisited

The three-dimensional, conjugate heat transfer (CHT) simulation of the internally-cooled C3X vane, presented in Chapter 6, provided the original motivation to develop a new turbulence model capable of handling streamline curvature effects. In the author's opinion, the main deficiency of the overall CHT methods developed for internally cooled turbine airfoils was the inability to achieve accurate heat transfer predictions on the

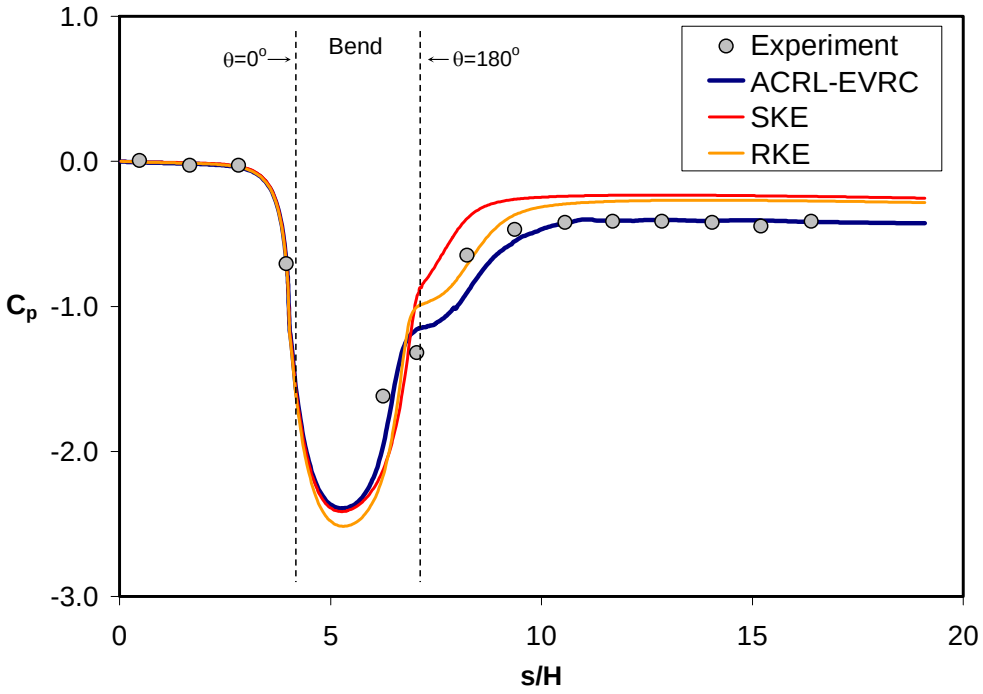

Figure 9.15 Variation of the static pressure coefficient on inner surface of U-bend.

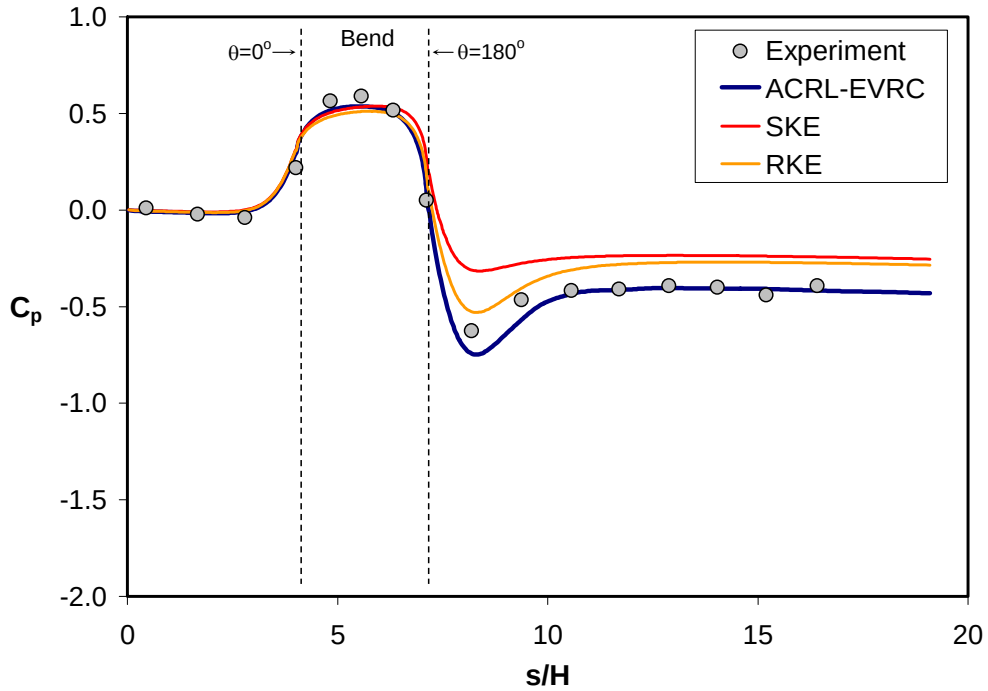

Figure 9.16 Variation of the static pressure coefficient on outer surface of the U-bend.

highly-curved suction surface, leading to errors in metal temperature predictions. In this section, the vane CHT simulation is revisited, with the ACRL-EVRC model employed. Minor modifications were made the new model in order to handle highly-compressible flows characteristic of the conditions in the vane cascade study. The subsonic, compressible "Case 1" was chosen for the test case. The geometry, boundary conditions, grid, discretization, and solution algorithms (the reader is referred to Chapter 6 for details) were all the same from the previous runs, so that the comparison isolates relative turbulence model performance. Note that this complex 3D simulation with large, multi-topology, unstructured mesh was a proving ground for the new model implementation. A converged solution was easily obtained with ACRL-EVRC, and only about 10 percent more runtime was required over the two-equations models packaged within Fluent 6.

Figure 9.17 shows contours of the turbulence level (definition based on the average velocity at the inlet plane) on the midspan plane near the very strong curvature of the suction surface for the RKE and ACRL-EVRC models. Just off the wall, the RKE model predicts turbulence levels in the freestream in excess of 30 percent. It is important to note that the convex shape of the surface should result in a reduction in turbulence locally, and that is exactly what is predicted by the ACRL-EVRC model. Turbulence levels are nearly constant away from the boundary layer. Since heat transfer coefficient often depends strongly on the freestream turbulence levels, one would expect that the heat transfer predicted by ACRL-EVRC to be lower along the highly-curved portion of the suction surface, compared to RKE. Indeed this is the case, as seen in Figure 9.18, plots of the predicted Stanton number (based on average conditions at the trailing edge plane), $\mathrm{St} = \dfrac{h}{\rho C_p U_{TE}}$ for the two turbulence models. Because the new model was

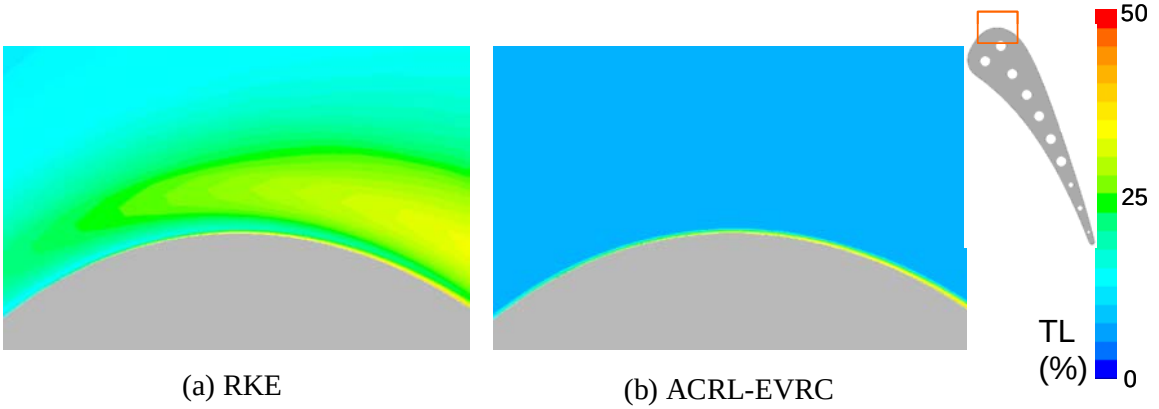

(a) RKE (b) ACRL-EVRC

Figure 9.17 Contours of turbulence level (based on inlet velocity) near the suction surface on the midspan plane of the C3X vane conjugate heat transfer simulation using (a) RKE model and (b) ACRL-EVRC model. The new eddy-viscosity model shows a reduction in turbulence where strong convex curvature of the vane surface exists.

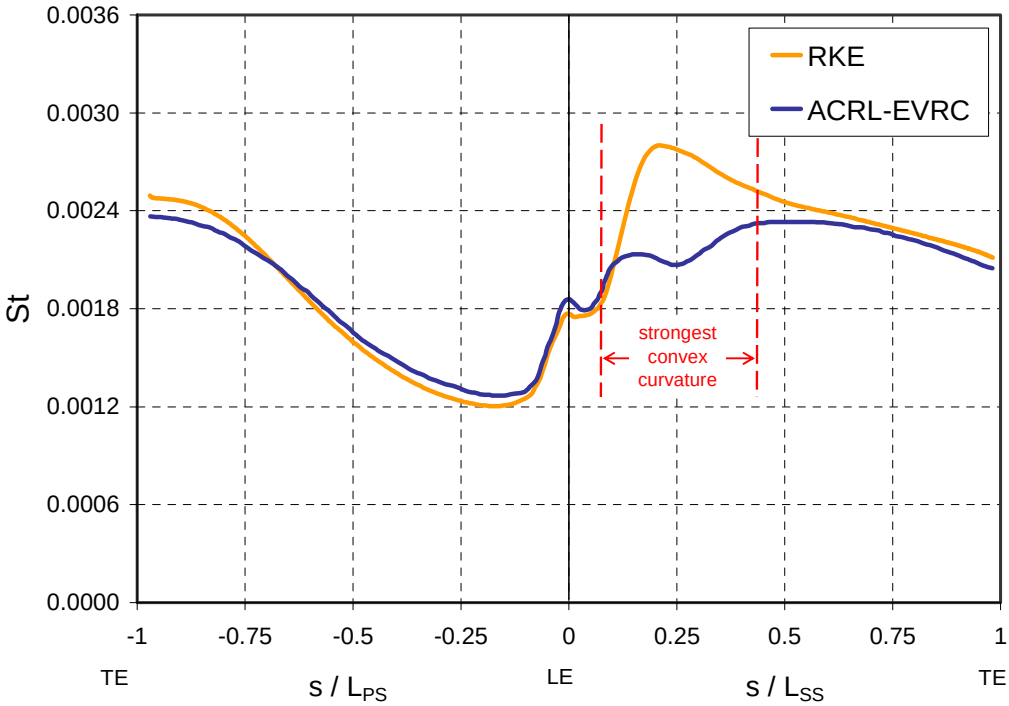

Figure 9.18 Stanton number distribution on the C3X airfoil at the midspan predicted by the RKE and ACRL-EVRC models. The major difference occurs in the region of strong convex curvature on the suction surface.

calibrated to behave as a realizable k-ε when no flow rotation (curvature) is present, it should be no surprise that predicted Stanton number is comparable everywhere except the strong convex curvature portion of the suction surface. ACRL-EVRC does predict a small increase in heat transfer, a result of turbulence augmentation, on the leading two-thirds of the pressure surface, which is characterized by mild concave curvature. Qualitatively, the trends in the turbulence and heat transfer predictions with the new model are correct.

The predictions of normalized static temperature (θ) distribution on the vane external surface at the midspan are plotted in Figure 9.19, along with the measured data of Hylton et al. (1983). Generally, wall temperature directly depends on the local external heat transfer coefficient (and the local fluid static temperature). The RKE model, which performed far superior to the standard k-ε model, produced reasonably good results for wall temperature over the vane surface, with the exception of the strong curvature portion of the suction surface. The overprediction in temperature by RKE corresponds to the location of the peak in the Stanton number on the suction surface. The new ACRL-EVRC model fixes this shortcoming of the other k-ε models. Due to lower predicted heat transfer coefficients on the suction surface where curvature is the strongest (centered about s/L_{ss}=0.2), the ACRL-EVRC wall temperature curve falls near the level experimental data in this region. With that improvement, the computed wall temperature follows the trend of the measurements over the entire vane. Recall that the surface temperature variation forms the basis of the validation for this complex problem, and therefore the new turbulence model increases the capability of the overall conjugate methodology, especially when applied to curved airfoils.

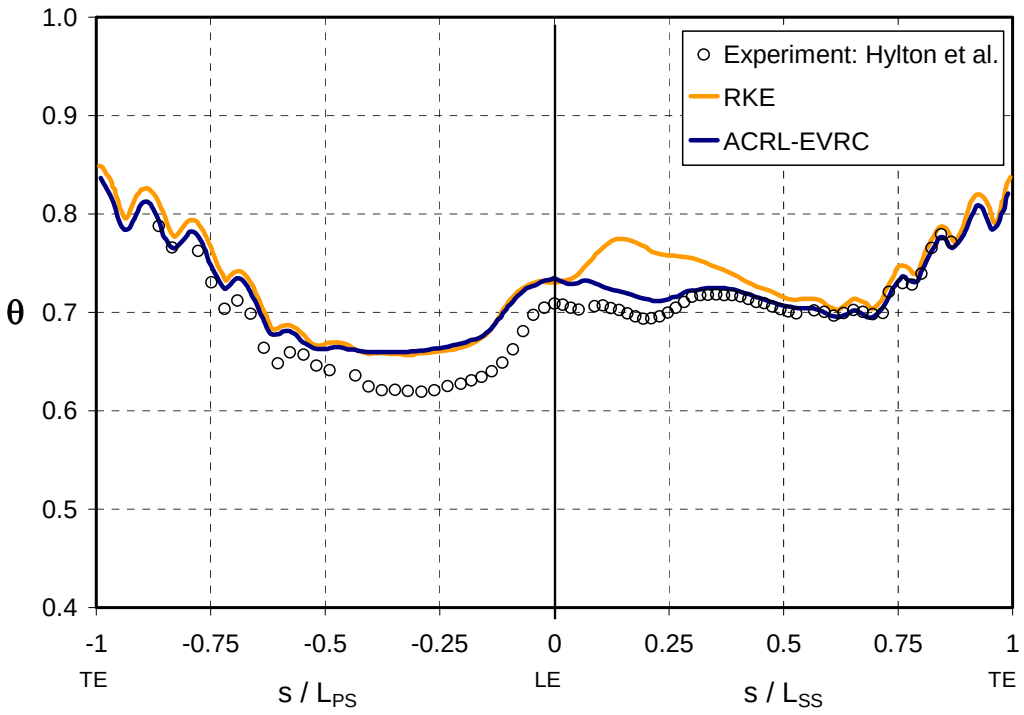

Figure 9.19 External vane surface temperature at midspan for the conjugate heat transfer simulations. The new ACRL-EVRC model improves predictions significantly on the suction surface, making the conjugate methodology more robust.

Three-dimensional Channel Turn Simulation

The final simulation designed to test the new turbulence model is one that is very applicable to gas turbine heat transfer, and that is the prediction of heat transfer inside the 180^{o} turn region of a three-dimensional (square cross-section) channel. The first reason this case was selected is that if results are encouraging, this case extends the conjugate methodology to include airfoil cooling with realistic multi-pass, or “serpentine”, internal passages. Already, straight, ribbed channels were incorporated into the methodology with novel models and validation. With predictive capability for the heat transfer in 180^{o}-turns, virtually any internal cooling configuration may be studied confidently with the CHT methodology. The second major motivating factor behind the choice of this

problem is that it represents a very stringent test case for RANS turbulence models, since it includes strong streamline curvature, pressure-gradients, separated shear layers, multiple flow recirculation zones, and curvature-induced secondary flow. Also, like the C3X vane case, the large, unstructured grid employed in this simulation serves to further test the implementation of the new model.

The simulation was designed to match the geometry and conditions of an experiment by Han et al. (1988) that employed a naphthalene sublimation technique and the heat-mass transfer analogy to get heat transfer data in a smooth-walled channel turn. The channel had a square cross-section with sides of dimension *H*. The legs upstream and downstream of the turn were separated by a divider of width *H*/4. The short wall section of the inner wall in the turn was rounded, and the outer turn wall was squared, characteristic of actual internal cooling passages. The clearance between the divider and the outer wall was equal to the channel height *H*. Figure 9.20 shows the geometry of the channel. The Reynolds number, based on the hydraulic diameter, D_h, was Re_{D_h}=30,000. The flow was close to being, but not quite, fully-developed at the entrance to the turn section. To allow calculation of the heat transfer coefficient distribution in the computations, a constant heat flux of relatively small magnitude was applied to all surfaces.

In order to reduce the numerical expense, natural symmetry was exploited and only the bottom half of the channel was included in the computational domain, with a symmetry plane located at the channel midpitch (half-height). The background numerical mesh consisted of 1.1 million unstructured hexahedra cells. The grid was stretched away from the channel walls to ensure full resolution of all boundary layers. A view of the grid

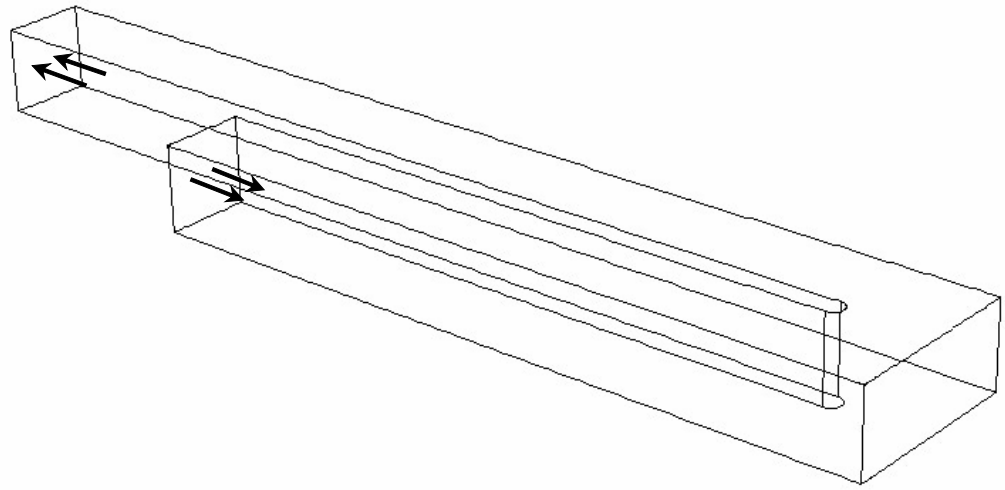

Figure 9.20 Computational Domain for the 180^o channel turn simulations.

on the midpitch (symmetry) plane is shown in Figure 9.21. Numerical predictions for heat transfer in the form of the Nusselt number, $Nu_{Dh}=h\kappa/D_h$, on the inside, outside, and bottom wall are compared with measurements of Han et al. (1988). Data is normalized by the Dittus-Boelter correlation for channel flow:

$$Nu_o = 0.024 Re_D^{0.8} Pr^{0.4} \quad . \tag{9.4}$$

All local heat transfer data is taken along lines down the middle of each surface. As shown in Figure 9.22, the data location is referenced to $x/D_h=0$ at the beginning of the turn section, where x is the local streamwise direction. Area-averaged heat transfer data is also presented, and this data is taken from sections immediately upstream (encompassing length of $3D_h$), the turn itself, and immediately downstream (length of $3D_h$). These sections are also shown in Figure 9.22. For convenience and clarity in data presentation, the normalized distance in the turn is referenced to the actual length on the centerline. This means, for example, on the inside wall the locations $x/D_h=0$ and $x/D_h=2$ are actually the same point.

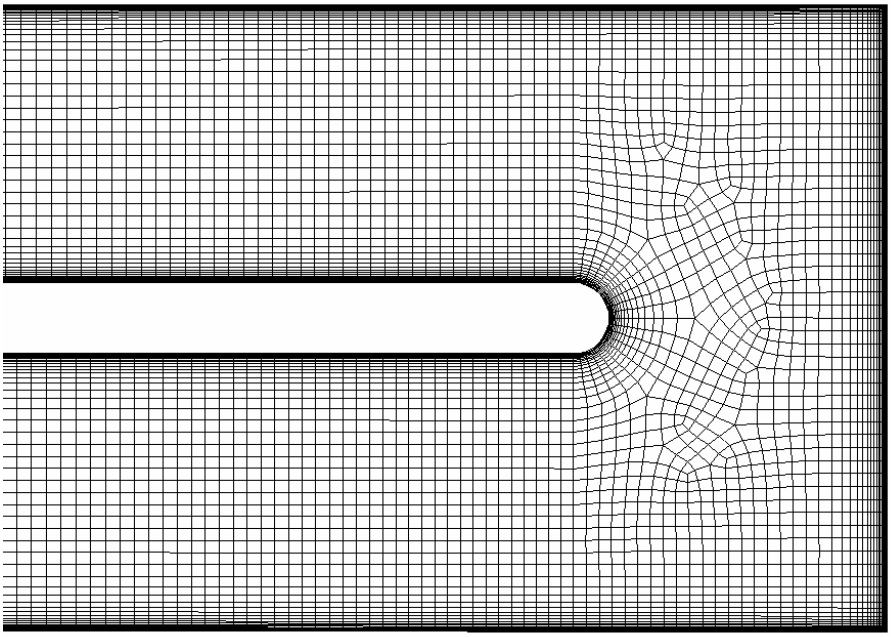

Figure 9.21 View of background mesh on the symmetry plane for the 180^{o} turn simulations.

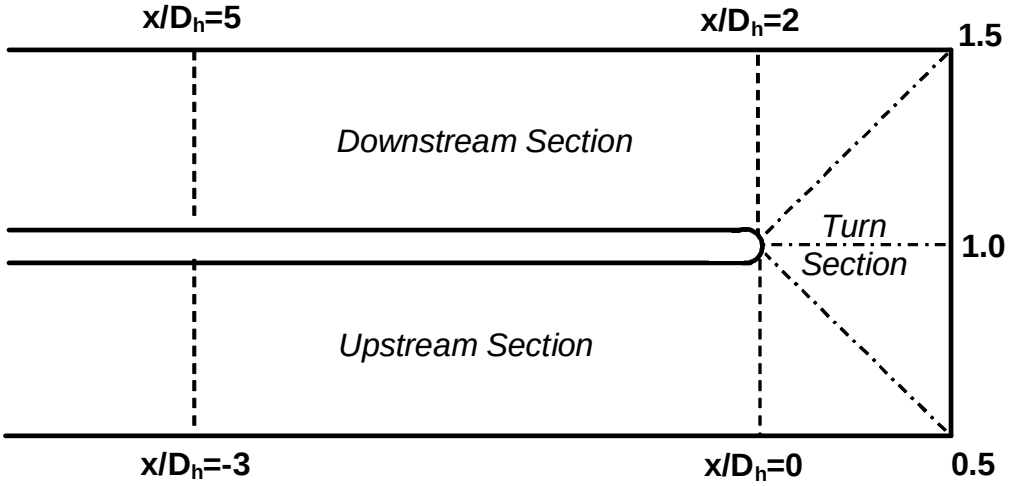

Figure 9.22 Channel cross-section showing data location and sections for data area-averaging.

The complexity of the flow in the 180^o-turn region is illustrated in Figure 9.23, contours of normalized velocity magnitude on the midpitch plane superimposed with black velocity vectors sized by magnitude. Results for all three models studied are presented, and there are slight differences in the flow predicted by the models, especially in the last half of the turn and just downstream of the turn. Along the inside wall, early in the turn, the flow separates from the highly-curved surface. The high-speed core of the flow is observed to move toward the outside wall just aft of the turn. All models predict a large, recirculation zone along the inside wall after the turn, and this low-momentum zone extends several diameters downstream. On the outside wall, small recirculation zones with low velocity magnitude exist in both of the 90^o corners of the turn. The strong curvature causes a secondary flow to develop, as seen in Figure 9.24, contours of velocity magnitude overlaid with velocity vectors on a plane oriented normal to the mean flow direction and located halfway through the turn. Clearly visible are a pair of counterrotating “Dean”-type vortices, with fluid moving toward the outer wall in the center of the channel cross-section and toward the inside of the turn near the top and bottom walls. This phenomenon is due to an imbalance of centripetal forces on fluid particles in the turn. Because of its greater speed, the fluid near the center of the channel experiences a larger centripetal force (away from the center of curvature) than the fluid near the walls. All simulations captured this mean-flow effect.

The Nusselt number distribution on the walls in and near the turn is affected primarily by the aforementioned complex flow conditions, which impact boundary layer development. To a lesser extent, the heat transfer is influenced directly by the local freestream turbulence, which augments the transport of heat from the wall to the bulk

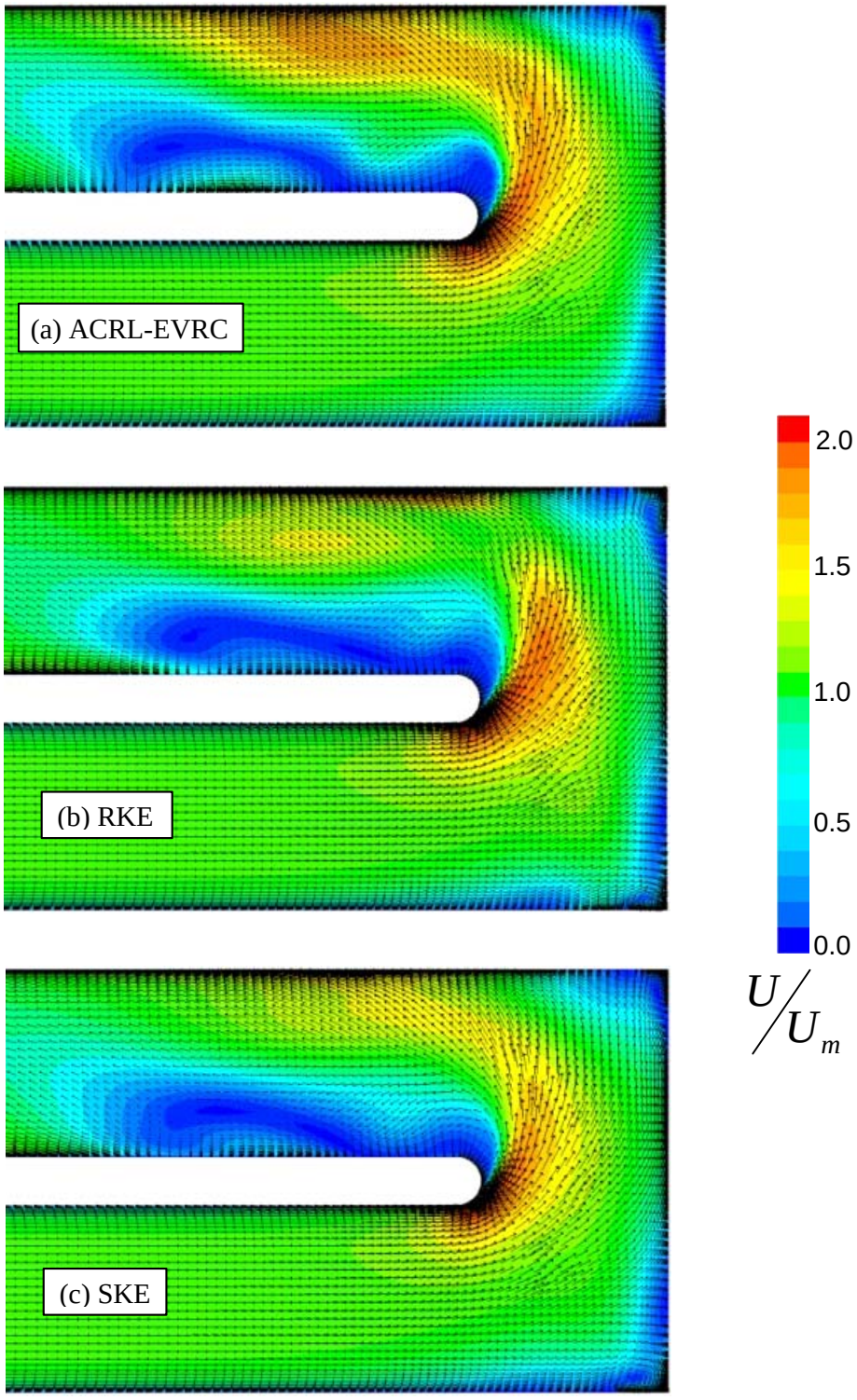

Figure 9.23 Contours of velocity magnitude overlaid with velocity vectors on the midpitch plane with (a) ACRL-EVRC, (b) RKE, and (c) SKE. Differences in turbulence predictions between the models leads to some variations in the mean flow patterns downstream of the turn. Numerous recirculation zones are evident from the vectors.

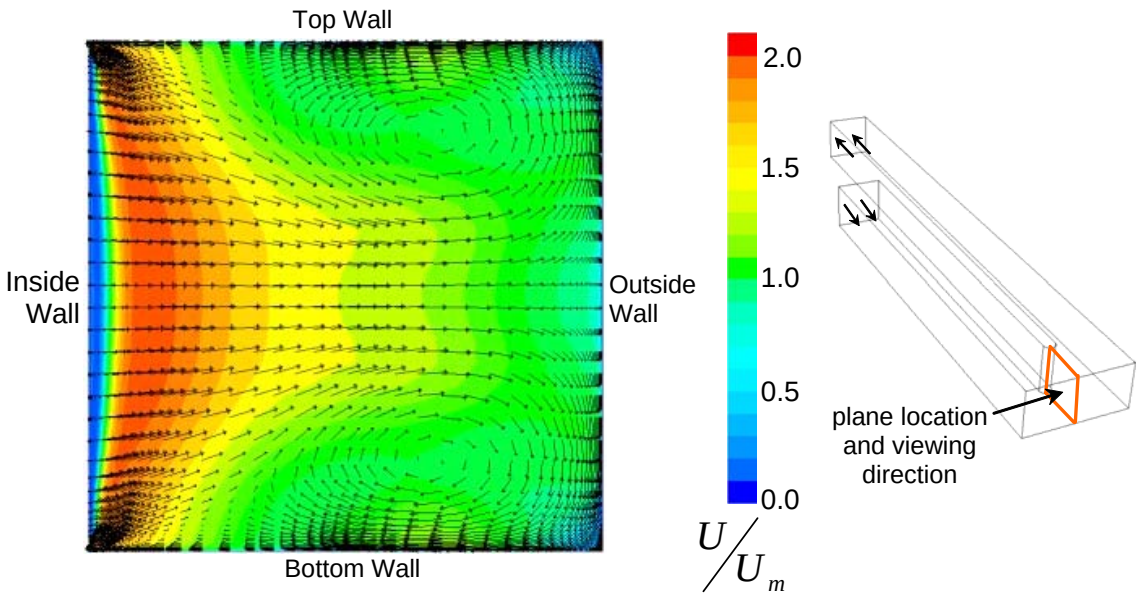

Figure 9.24 Velocity vectors overlaid on contours of normalized velocity magnitude on a plane normal to the primary flow direction and midway through the turn. Results are from the ACRL-EVRC case. The curvature results in a counter-rotating vortex pair, clearly seen in the vectors.

fluid. Then the turbulence predictions, and therefore the turbulence model, impact the quality of the Nusselt number predictions. Figure 9.25 shows predicted and measured Nusselt number variation along the midpitch of the inner wall. Clearly the new ACRL-EVRC model gives much better predictions for heat transfer than SKE or RKE immediately downstream of the turn. The peak Nusselt number near x/D_h=3.5 in the ACRL-EVRC case is very close to the experimental maximum. The high heat transfer here is due to flow reattachment after a fairly long recirculation zone.

The Nusselt number distribution on the outer wall, plotted in Figure 9.26, exhibits large variations in the bend. All models predict the same general trends. There is a slight reduction in heat transfer in the first corner near x/D_h=0.5, followed by a large increase as the high-speed flow in the center of the channel impinges against the outside surface

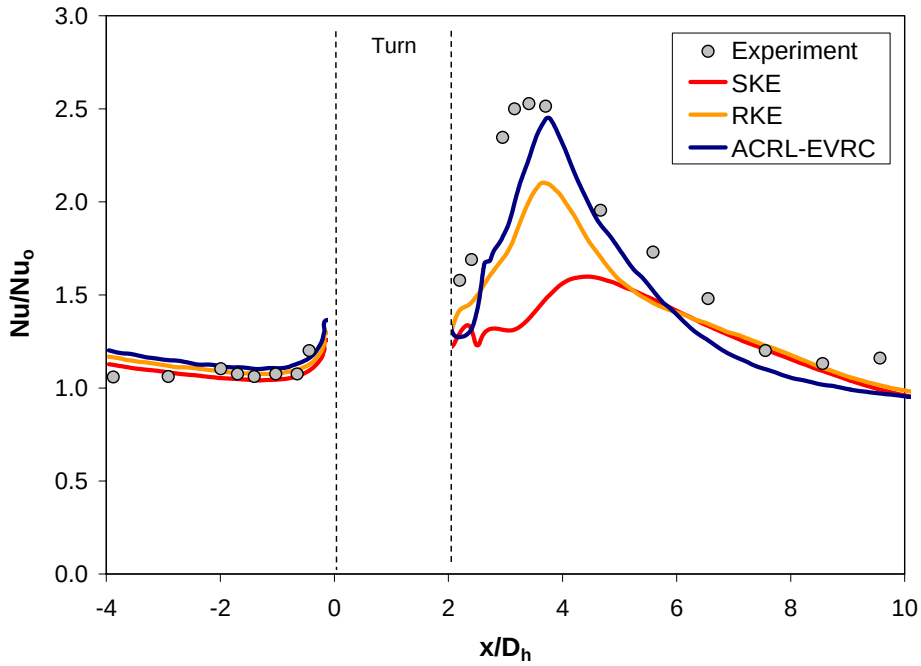

Figure 9.25 Predicted and measured Nusselt number distribution along the midpitch of the inside wall in the vicinity of the channel turn. Clearly, the new model gives superior prediction immediately downstream of the turn.

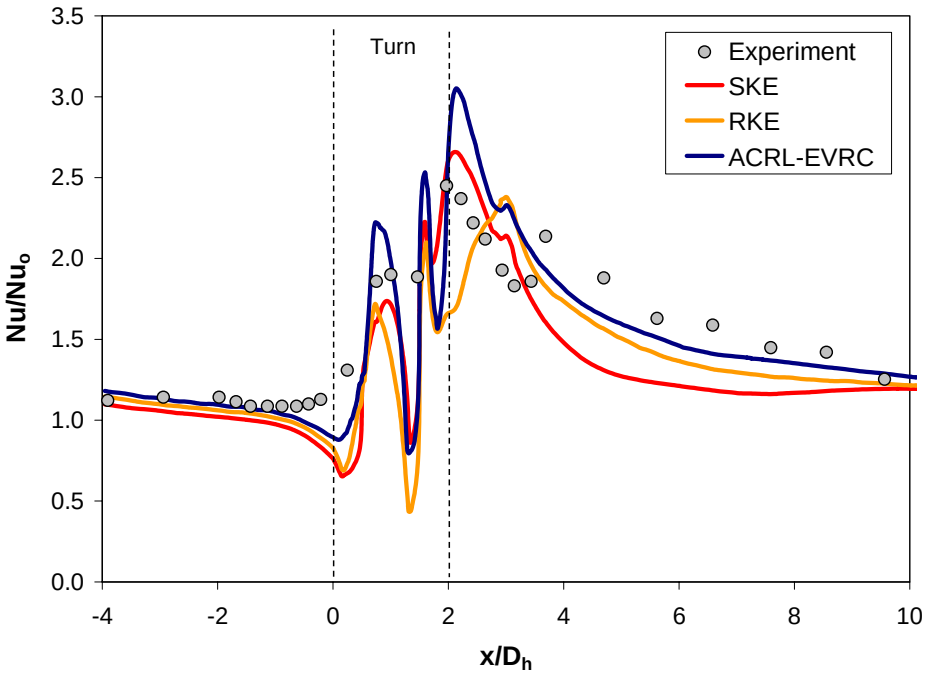

Figure 9.26 Predicted and measured Nusselt number distribution along the midpitch of the outside wall in the vicinity of the channel turn.

about halfway through the turn. Next comes a significant drop in Nu_D in the second 90^o corner where the flow is separated and low momentum fluid resides. Finally, heat transfer increases as the fast-moving fluid in the core impinges against and moves along the outer wall near the exit of the turn section. The ACRL-EVRC model predicts a slight augmentation of turbulence due to the curved streamlines near the outer wall, resulting in slightly higher values for Nu_D that are right in line with the measurements. Immediately downstream of the turn, the new model predicts higher heat transfer than the measured data and the other two models, but further downstream the new model results better match the experimental trend.

The Nusselt number variation on the bottom surface, shown along the centerline between the inner and outer walls in Figure 9.27, is largely dependent on the local velocity. Both ACRL-EVRC and RKE give good predictions for local heat transfer on the bottom wall in the turn region, while SKE falls short as compared to measurements. Immediately downstream of the turn, past x/D_h=2.5, ACRL-EVRC is the only model that reproduces the shape of the experimental results curve (a double peak), and clearly the new model gives good prediction for bottom-surface heat transfer through the entire downstream leg of the channel, while the other two models, especially SKE, significantly underpredict Nu_D.

As in the ribbed channel heat transfer simulations of Chapter 7, the ability to confidently include channel turns in a conjugate heat transfer simulation is dependent on the accurate prediction of “small-area” averaged heat transfer coefficients on the channel surfaces. Local variations in heat transfer coefficients are relatively insignificant due to the three-dimensional heat diffusion taking place inside the solid. Therefore it is

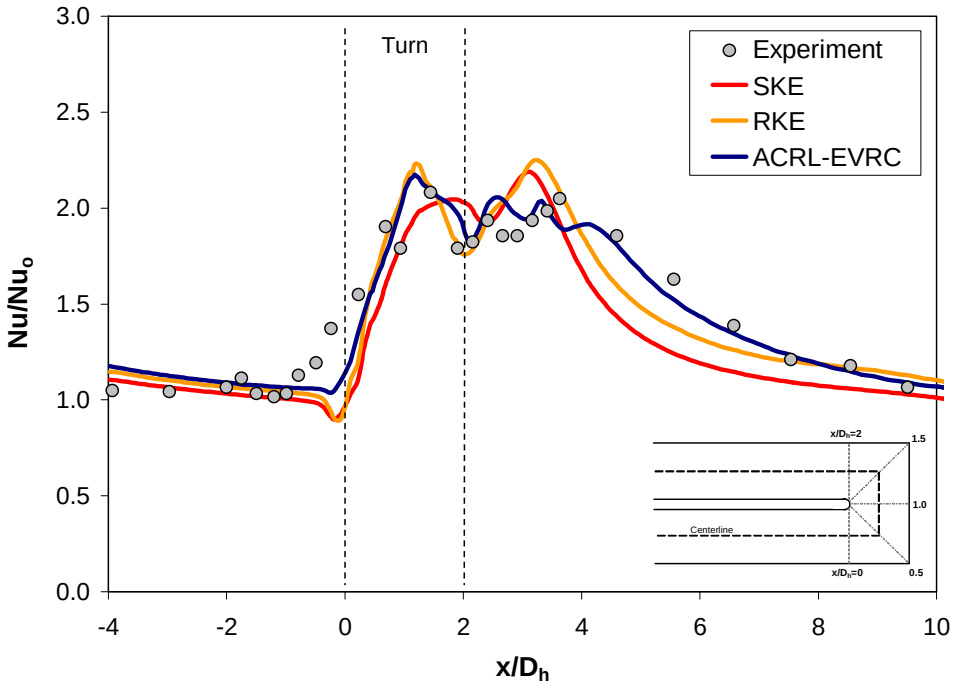

Figure 9.27 Predicted and measured Nusselt number distribution along the centerline (dashed line on inset) of the bottom wall in the vicinity of the channel turn.

instructive to examine the local area-averaged Nusselt number prediction for different zones, marked in Figure 9.22, on the inner and outer walls in the 180^o-turn region. For the inside wall, area-averaged Nusselt numbers are plotted in Figure 9.28. Note that because of the very sharp turn (no measurements on the end of the rounded divider), there is no "turn"-region data – only upstream and downstream, each averaging region consisting of the full wall over a streamwise length of 3 diameters. All models give good predictions when compared to the experimental data for the upstream zone. In the downstream zone of the inner wall, the ACRL-EVRC model gives a prediction for average heat transfer that is less that 10 percent below the measurement. The standard k-ε model performed relatively poorly with nearly a 25 percent underprediction.

The area-averaged Nusselt numbers on the outer wall are plotted in Figure 9.29. Note that, per the practice of Han et al. (1988), the "turn" region consists of all surface between x/D_h=0 and x/D_h=2, making a squared "U" shape zone. Again, all models give good predictions for average Nusselt number on the upstream wall section. In the turn itself, the ACRL-EVRC model prediction is within the experimental uncertainly to the measured data, while the other two models underpredict heat transfer. For the downstream zone, ACRL-EVRC and the realizable k-ε model slightly overpredict the average Nusselt number, while the SKE model gives a small underprediction.

Summary of New Model Performance

Based on the above results from a series of test cases and several complex problems in gas turbine airfoil heat transfer, the new eddy-viscosity model was shown, in a qualitative sense, to exhibit the correct sensitivity to streamline curvature and rotation effects. In all cases, the ACRL-EVRC model was put up against the "standard" k-ε model and/or the "enhanced" RKE model. When rotation or curvature was involved, the new model consistently delivered superior predictions for turbulence, mean flow, wall shear stress, and/or heat transfer. When curvature or rotation was not important, the new model performed like the RKE model, which itself incorporates more physics than SKE.

The new model also met the original goal of being relatively simple, efficient, and easy to implement in any code, such as Fluent 6 in this case. For all simulations presented, a fully-converged solution with the ACRL-EVRC model was obtained with no additional effort compared to the two-equation models packaged with the code, and with less than a 10 percent increase in run-time. The new model represents an economical tool that brings additional physical realism into the conjugate methodology.

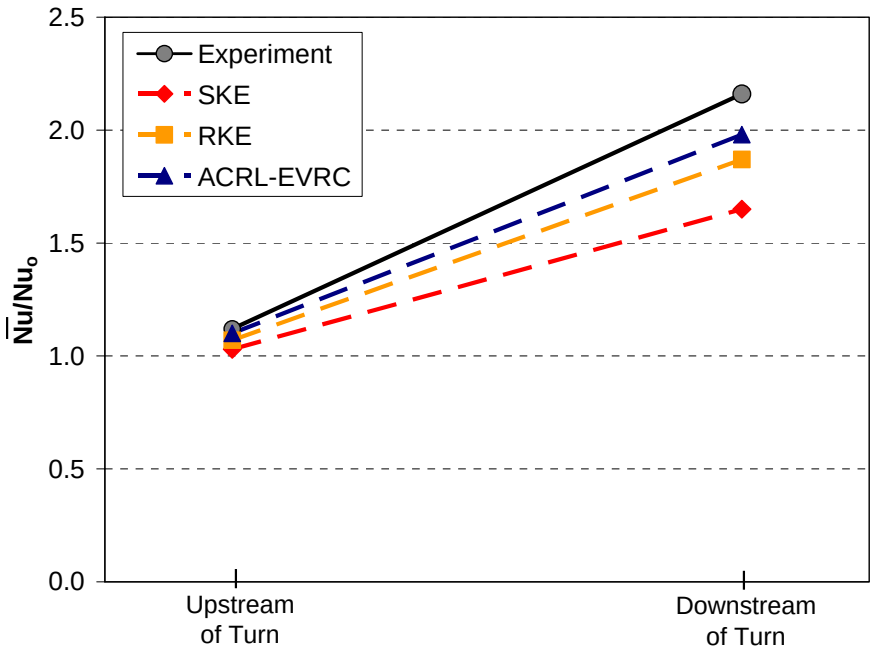

Figure 9.28 Area-averaged Nusselt number predictions and measurements for the inside wall. The zones for averaging are marked in Figure 9.22.

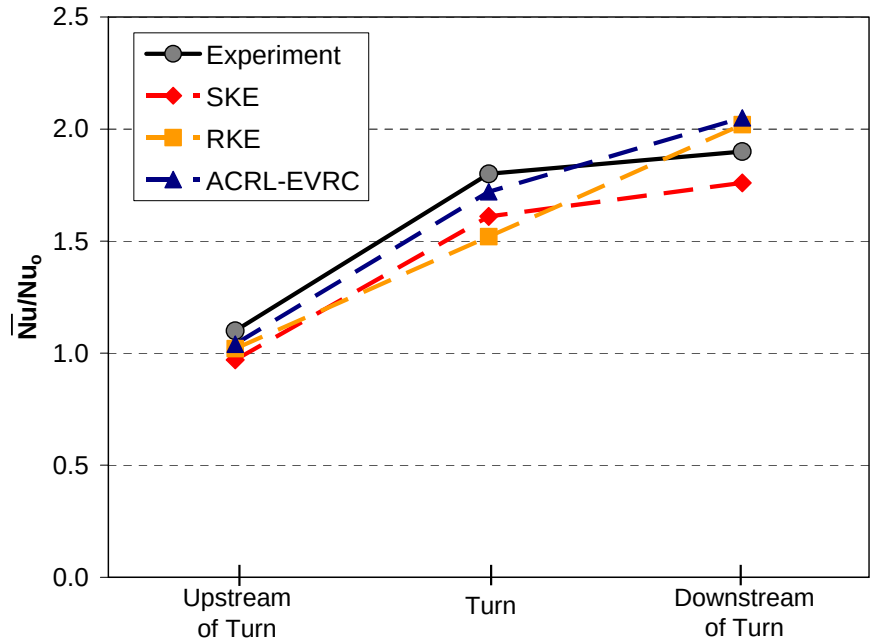

Figure 9.29 Area-averaged Nusselt number predictions and measurements for the outside wall. The zones for averaging are marked in Figure 9.22.

CHAPTER 10

SUMMARY, CONCLUSIONS, AND RECOMMENDATIONS

Summary

A comprehensive, computational methodology, based on the Reynolds-averaged Navier-Stokes equations, for conjugate heat transfer (CHT) problems has been developed and validated. The motivation for development of a robust CHT methodology was the efficient solution for the metal temperature field of internally-cooled gas turbine airfoils. Turbine airfoils operate in extremely harsh thermal conditions, and the life of the parts are largely dependent on the temperature and the temperature gradients in the metal. Consistently accurate prediction of the temperature field is a critical piece of the design process. The current industry design practice involves separate analysis of the heat transfer modes – external convection, internal convection, and conduction in the solid. The decoupled process results in lost accuracy and is time-consuming when design changes are required

The conjugate heat transfer method mimics the natural heat transfer process, employing a single CFD simulation in which the convection in the fluid regions, both internal and external, is coupled (via energy conservation at the interfaces) with the heat diffusion in the solid parts. The CHT method is more accurate and efficient in a design environment, especially for design iterations. While a CHT simulation might seem like an obvious choice for complex convection-conduction problems, it has not been widely adopted for several reasons. One reason is that, because of their greater complexity, CHT simulations typically have a high computational expense due to larger number of nodes

and slow convergence of metal temperature. As computational infrastructure advances, this obstacle will become less significant. The other resistance to the use of the CHT method is the known difficulties in accurately predicting heat transfer coefficients for extremely complex external and internal flows encountered in gas turbine applications. This difficulty is often a function of limitations in the turbulence models.

The present conjugate heat transfer methodology starts with a commercial RANS-based CFD software package, Fluent 6. The first stage of the work involved the development of a state-of-the-art numerical process specifically for CHT simulations using “off-the-shelf” technology (existing pre-processing software, solvers, and popular turbulence models). The methodology was streamlined for mainstream design by developing high-quality gridding techniques, investigating the optimal fluid-solid interface coupling, and creating an enhanced initialization scheme for the airfoil temperature distribution. The latter contribution, for example, can cut more than eight percent off run-time.

The CHT methodology was validated with data from a turbine vane cascade study conducted by Hylton et al. (1983) at engine-realistic conditions. This study involved a stainless steel airfoil that was cooled with air flowing radially in ten smooth-walled channels in the vane. This is the only experimental study that exists in the open literature that involves an active (in a heat transfer sense) metal airfoil with internal cooling. Using the measured values for comparison, the CHT simulation of the problem using the realizable k-ε turbulence model gave reasonably good predictions for the external surface temperature at the vane midspan. The only glaring exception was an area on the suction surface where the computations showed a rise in temperature where vane surface

curvature was very large, while the measurements indicated a slight dip in temperature. The standard k-ε model overpredicted the temperature distribution over the vane because of spurious production of turbulent kinetic energy where the irrotational strain was large at the vane leading edge and in the passage.

It was desired to extend the conjugate heat transfer methodology to include channels with ribs, or turbulators, on their surfaces, as this configuration is commonly used in turbine airfoils to achieve higher heat transfer coefficients on the inside surfaces and more efficient cooling. Unfortunately, as stated earlier, no conjugate experimental study exists that includes ribbed internal passages, so this phase had to be validated separately. When accurate predictions for the heat transfer coefficients are achieved with numerical simulations, then this capability can be integrated with confidence into a full CHT simulation.

Two different ribbed-channel test cases were selected and simulated with results compared to experimental data. Steady simulations with the realizable k-ε model and a differential Reynolds-stress model produced significant underprediction of the heat transfer coefficients on the ribbed wall(s). The author hypothesized that the inherent unsteady shear layer breakup into coherent, small eddies would have an impact on the heat transfer, and this mechanism is missing in the steady computations. Further, it was discovered that existing models are incapable of sustaining the unsteady shear layer roll-up and breakdown. Therefore, a new, in-house turbulence closure was employed to allow the small-scale unsteadiness to be resolved in time-accurate simulations. Results of the unsteady simulations prove that the unsteadiness behind the ribs is indeed important, and

predictions of the area-averaged Nusselt number on the ribbed wall jumped to within 15 percent of measured at realistic Reynolds numbers.

As previously discussed, the wall temperature trend on the suction surface of the vane in the CHT simulation was the remaining weakness of the methodology. The author believed that the key to better predictions here was the use of a turbulence model designed to capture the effects of streamline curvature on the turbulence field. Previous attempts to create an eddy-viscosity-based turbulence model with curvature sensitivity resulted in second derivatives of velocity in the calculation of the eddy-viscosity itself, and this led to practical difficulties in implementation in a general purpose solver. A key piece of the present work was the development of a new, robust turbulence model designed to capture the effects of streamline curvature (and system rotation, by analogy) on the turbulence field. The new model, designated ACRL-EVRC, emerged from an algebraic Reynolds-stress model formulation that included a new, physically-correct definition for the *flow* rotation rate. The Boussinesq and other assumptions and simplifications led to an eddy-viscosity formulation. Then, to eliminate the second derivatives in the algebraic equation for eddy-viscosity, it was assumed that locally the shear field was two-dimensional and homogeneous, a reasonable conjecture for the types of engineering flows studied herein. Additionally, the ACRL-EVRC model includes a new near-wall treatment based on the equations of Wolfstein (1969), but with a dynamic scale matching to define the near-wall zone size.

The new ACRL-EVRC model was first applied to a series of increasingly complex test cases,including simple 2D channel flow, rotating channel flow, and flow in a U-bend. The results were very encouraging. Then the 3D vane conjugate heat transfer

problem was revisited with the new model. As anticipated, the new model showed proper response to curvature, including decreased turbulence along the convex curvature of the suction surface, reducing heat transfer, and therefore wall temperature locally. This brought the temperature distribution trend in line with the experimental data. Another benefit of the curvature-sensitive model was the ability to better predict heat transfer in the 180^{o}-turn region of a 3D channel, typical of the turns in a serpentine cooling passage in a turbine airfoil. This further extends the applicability of the overall conjugate methodology, since virtually any complex internal cooling geometry (ribbed and/or multi-pass channels) can be handled.

The importance of new, simple-to-implement, physics-based turbulence modeling has emerged as a critical finding of the present study. New modeling tools, such as ACRL-EVU (York et al., 2005), ACRL-SDSM (Holloway, 2005), and ACRL-EVRC (developed exclusively in present study) all proved themselves with better predictions for various building blocks in the CHT methodology. They are all variants of the k-ε model, meaning that, in theory, they could be combined. In practice, this is somewhat difficult, since slight variations in model formulation specific to the physics targeted make the marriage difficult. But Fluent, and most other mature RANS solvers, allow the use of multiple models in each simulation, as well as the zonal selection of models. Then each new model can be employed where it is most effective, such as ACRL-SDSM in straight sections of ribbed passages and ACRL-EVRC in the channel turns and in the external hot gas flow over the airfoils.

Original Contributions

In the course of the present research program, numerous original contributions were made in a variety of areas. The following list summarizes the unique features of this work:

- First documentation of a *fully-validated* conjugate heat transfer methodology for *three-dimensional*, internally-cooled airfoils at engine-realistic conditions that included solutions within the internal channels themselves.

- Development of an efficient gridding technique for turbine airfoil conjugate heat transfer problems (with solid and multiple fluid zones) that results in high-quality mesh and appropriate grid density in key areas.

- Investigation of the numerical algorithm for coupling the solid-fluid interface via energy conservation to find the most stable and efficient method for fastest solution convergence.

- Creation of a "enhanced" initialization scheme for the starting temperature distribution in the airfoil (solid zone) that is executed by a user-defined function in seconds and may reduce run-time by over eight percent.

- First study in the open literature to highlight the importance of capturing the effects of unsteady shear layer roll-up and breakdown on the heat transfer prediction on ribbed channel surfaces. Results also showed that existing turbulence models were incapable of sustaining the small-scale unsteadiness.

- Contribution to the development and testing of a new eddy-viscosity model, ACRL-EVU, that allows the unsteady roller vortices aft of the ribs to be resolved, giving much improved heat transfer predictions over steady models (which would not sustain unsteady motions).

- Documentation of new guidelines for determining convergence and refining the grid in shear-layer-type unsteady problems.

- Development of a new eddy-viscosity-based turbulence model that is correctly sensitized to streamline curvature and system rotation. Unlike other models designed for this purpose, the new ACRL-EVRC model eliminates second derivatives in its formulation of the eddy-viscosity. This makes it useful in practice, and not just theory, by allowing it to be efficiently implemented in a general-purpose solver and employed for virtually any problem.

- Implementation of a new near-wall turbulence treatment within the ACRL-EVRC model that has a more physical "dynamic scale matching" feature to effectively size the near-wall zone.

- Only study in the literature to show the importance of curvature effects, especially on the suction surface, on temperature predictions for gas turbine airfoils.

Conclusions

Many of the findings of the present research program are summarized earlier in this chapter. Still, it is worthwhile to highlight some of the key conclusions that emerged from the results of this study, which are listed below:

- The conjugate heat transfer methodology, when practiced with careful quality-control and validation, is an effective tool to study complex, coupled aerothermal problems, such as the internally-cooled gas turbine airfoil.

- The numerical implementation of the solid-fluid interface heat transfer coupling greatly influences the stability and run-time required in a CHT simulation. Also, the enhanced initialization of the solid temperature field, to mimic the final distribution as closely as possible, may significantly reduce computational expense.

- The standard k-ε turbulence model does not perform particularly well for turbine airfoil heat transfer problems (including CHT simulations) because it results in the spurious production of turbulence kinetic energy in regions of rapid, irrotational strain (at leading edge and in airfoil passage). This non-physical elevated turbulence causes overprediction of the heat transfer coefficients over the entire vane surface.

- The realizable k-ε turbulence model is the best "off-the-shelf" model tested for CHT turbine airfoil simulations, eliminating the problem with SKE discussed above. However, RKE overpredicts heat transfer on a portion of the highly-curved airfoil suction surface, largely because of its incorrect sensitivity to streamline curvature.

- In the ribbed-channel heat transfer problem, the ability to account for (resolve or model) the unsteady shear layer breakup and roller vortices aft of the ribs is of utmost importance in accurate predictions of heat transfer coefficients on the ribbed surface.

- Popular “off-the-shelf” models (such as SKE and RKE) in Fluent and other commercial codes will not sustain unsteady motions in a time-accurate simulation because they are exceedingly diffusive. A new in-house model was required to physically allow the unsteadiness to be resolved.

- Time-accurate simulations to capture the time-averaged heat transfer require a significant amout of run-time and are very sensitive to the grid size in the shear-layer zones. For this reason, new convergence monitoring and grid refinement are needed. The semi-deterministic stress model, ACRL-SDSM, developed by Holloway (2005) captures the effect of the unsteady roller vortices in a steady framework, greatly reducing computational expense.

- It is reasonable to make the assumption of locally two-dimensional, homogeneous shear in the development of a new eddy-viscosity model sensitized to streamline curvature and rotation. The new ACRL-EVRC model performed superior to all other models tested for a variety of gas turbine flows.

- Streamline curvature is indeed an important mechanism in the heat transfer process of gas turbine airfoils, and the ACRL-EVRC model fixed the poor prediction in wall-temperature trend on a short segment of the suction surface produced by other models.

Recommendations for Future Work

While the work presented in this thesis represents an extensive effort in creating a robust conjugate heat transfer methodology that may be used in the aerothermal design of gas turbine airfoils, the author has several recommendations for future work that could advance the technology even further. The first recommendation is the extension of the CHT methodology to include film cooling of the airfoils. Film cooling is an advanced cooling technology, used commonly on forward-stage airfoils and especially in aviation applications, in which the internal coolant air is forced through arrays of tens or even hundreds of tiny holes in the airfoil walls where it is introduced into the hot gas flow. Cooling of the part occurs, in theory, by forming a layer of cooler air over the surface of the airfoil, and also by convection inside the holes. Film-cooling flows involve complicated jet/crossflow interactions and strong secondary flows, both of which push

existing turbulence models to their physical limits. Because the basic CHT methodology has been validated for internally-cooled airfoils, this serves as a platform to confidently explore adding film cooling. Researchers in the ACRL at Clemson University, including the present author, have much experience in accurately simulating film-cooling problems (see York, 2000), and a marriage of this technology with the conjugate heat transfer methodology is a logical next step.

There is more room for advancement in physics-based turbulence modeling for RANS-based CFD that could further improve predictive capability for heat transfer problems. For example, there is a need for accurate sensitivity of models to both velocity and length scales of turbulence. Accomplishing this would allow the conjugate turbine vane simulation to be more responsive to the turbulence intensity and length scale of the inlet flow, which can both be quite large and vary significantly when a combustor is located immediately upstream of the airfoils. Also, the integration of a wall-roughness model into the near-wall turbulence model could allow the methodology to be used for aerothermal analysis of airfoils after years of service when they are no longer aerodynamically smooth. A difficulty to overcome with additional work is the combination of these turbulence modeling features into a single, cohesive model.

The author believes that the present work not only laid a foundation for the conjugate heat transfer methodology to be integrated into the gas turbine hot section design process, but also brought some maturity to the process with advanced tools like novel turbulence models. As computational resources increase in capacity and affordability, so will the scale of the CHT simulation. As none of the work herein is hard-wired specifically for the gas turbine industry, it may be used in design in a variety of

other applications where complex heat transfer problems exist. Further, through the heat-mass transfer analogy, this work can be applied to problems with coupled mass convection and mass diffusion.

APPENDICES

Appendix A: UDF Code for Enhanced Airfoil Initialization

The following is the User-Defined Function (UDF) code for enhanced initialization of the metal temperature field in the internally-cooled airfoil. It is designed to be quickly and easily executed on demand by the Fluent software user after the case file and fluid zones have been initialized. The UDF is written in the C language for integration with Fluent 6. Note that macros are defined in the udf.h header file, which is supplied by Fluent. See Fluent Inc. (2005) for more details on compilation and implementation of UDFs.

```
#include "udf.h"

/* Constants */

#define CTT 300.0           /* Input cool side total temperature [K] */
#define SPECHEAT 1007.0    /* Input cool side specific heat [J/kg-K] */
#define PR_C 0.704          /* Input cool side Prandtl number */
#define K_C 0.028           /* Input cool side conductivity W/m-K] */
#define VISC_C 0.000019   /* Input cool side dyn. viscosity [N-s/m2] */

#define HTT 796.0          /* Input hot side total temperature [K] */
#define RE 1800000.0       /* Input vane Reynolds number based on true
                              chord and average velocity */
#define PR_H 0.702         /* Input hot side Prandtl number */
#define K_H 0.054          /* Input hot side conductivity [W/m-K] */
#define AREA_H 0.0244     /* Input vane external surface area [m2] */

#define CHORD 145.0         /* Input vane true chord [mm] */
#define SPAN 76.2      /* Input airfoil span (radial dimension) [mm] */

#define X_1 20.592567    /* Input cooling channel centerline
                            coordinates [mm] */
#define X_2 10.985448
#define X_3 27.584846
#define X_4 36.403820
#define X_5 44.033781
#define X_6 51.237573
#define X_7 57.584501
#define X_8 63.550885
#define X_9 69.141223
#define X_0 74.442352
```

```
#define Y_1 120.089173
#define Y_2 110.766289
#define Y_3 102.952195
#define Y_4 90.144845
#define Y_5 77.089406
#define Y_6 63.048407
#define Y_7 49.352359
#define Y_8 34.957139
#define Y_9 20.667222
#define Y_0 6.056745


#define RAD_1 3.15    /* Input cooling channel radii [mm] */
#define RAD_2 3.15
#define RAD_3 3.15
#define RAD_4 3.15
#define RAD_5 3.15
#define RAD_6 3.15
#define RAD_7 3.15
#define RAD_8 1.55
#define RAD_9 1.55
#define RAD_0 0.99

#define FLOW_1 0.00889   /* Input cooling channel flow rates [kg/s] */
#define FLOW_2 0.00764
#define FLOW_3 0.00728
#define FLOW_4 0.00787
#define FLOW_5 0.00796
#define FLOW_6 0.00812
#define FLOW_7 0.00758
#define FLOW_8 0.00271
#define FLOW_9 0.00166
#define FLOW_0 0.000822

#define TOUT_1 350.0    /* Input coolant avg total temp at channel
                           outlets [K] */
#define TOUT_2 350.0
#define TOUT_3 348.0
#define TOUT_4 348.0
#define TOUT_5 350.0
#define TOUT_6 352.0
#define TOUT_7 355.0
#define TOUT_8 397.0
#define TOUT_9 417.0
#define TOUT_0 475.0

/* User Defined Scalars */

#define OW_DIST 0



/* User Defined Memory */

#define OW_DIST 0
#define INIT_TEMP 1
```

```
/* ----------------- Define on Demand ---------------------------*/

DEFINE_ON_DEMAND(ow_dist_to_mem) /* This execute on demand function
writes the smallest distance from each node to outer surface from a
user-defined scalar to memory – execute this first, then display
contours of User-Defined Memory UDM1 to verify correct */
{
Thread *t;
cell_t c;
real delta;
Domain *domain;
domain=Get_Domain(1);

thread_loop_c(t,domain)
{
 {
  begin_c_loop(c,t)
  {
   C_UDMI(c,t,OW_DIST)=C_UDSI(c,t,OW_DIST);
  }
  end_c_loop(c,t)
 }
}

}



DEFINE_ON_DEMAND(init_vane_temp)
{
Thread *t;
cell_t c;
real delta;
Domain *domain;
domain=Get_Domain(1);
real centroid[3];
real x, y, z;
real z_ref;
real iwd;
real d_1, d_2, d_3, d_4, d_5, d_6, d_7, d_8, d_9, d_0;
real temp_1,temp_2,temp_3,temp_4,temp_5,temp_6,temp_7,temp_8;
real area_c;
real q_tot;
real htc_c;
real walltemp_c_mid, walltemp_c_top, walltemp_c_bot;
real htc_h;
real walltemp_h_mid, walltemp_h_top, walltemp_h_bot;
real h_temp, c_temp;
real avg_exit_temp;
real delta_c_temp;
real pi = 3.14159;

/* Calculate total area of cooling channel walls */
area_c = (2. * SPAN * pi * (RAD_1 + RAD_2 + RAD_3 + RAD_4 + RAD_5 +
RAD_6 + RAD_7 + RAD_8 + RAD_9 + RAD_0)) / 1000000.;
```

```
/* Calculate total heat transfer rate [W] */
q_tot = SPECHEAT * (FLOW_1*(TOUT_1 - CTT) + FLOW_2*(TOUT_2 - CTT) +
FLOW_3*(TOUT_3 - CTT) + FLOW_4*(TOUT_4 - CTT) + FLOW_5*(TOUT_5 - CTT) +
FLOW_6*(TOUT_6 - CTT) +
FLOW_7*(TOUT_7 - CTT) + FLOW_8*(TOUT_8 - CTT) + FLOW_9*(TOUT_9 - CTT) +
FLOW_0*(TOUT_0 - CTT));

/* Calculate avg Nusselt number in cooling channels */

htc_c = 0.023 * K_C * pow(PR_C,0.4) * 0.1 * (
(500./RAD_1)*pow(((4.*FLOW_1)/(0.002*pi*RAD_1*VISC_C)) , 0.8) +
(500./RAD_2)*pow(((4.*FLOW_2)/(0.002*pi*RAD_2*VISC_C)) , 0.8) +
(500./RAD_3)*pow(((4.*FLOW_3)/(0.002*pi*RAD_3*VISC_C)) , 0.8) +
(500./RAD_4)*pow(((4.*FLOW_4)/(0.002*pi*RAD_4*VISC_C)) , 0.8) +
(500./RAD_5)*pow(((4.*FLOW_5)/(0.002*pi*RAD_5*VISC_C)) , 0.8) +
(500./RAD_6)*pow(((4.*FLOW_6)/(0.002*pi*RAD_6*VISC_C)) , 0.8) +
(500./RAD_7)*pow(((4.*FLOW_7)/(0.002*pi*RAD_7*VISC_C)) , 0.8) +
(500./RAD_8)*pow(((4.*FLOW_8)/(0.002*pi*RAD_8*VISC_C)) , 0.8) +
(500./RAD_9)*pow(((4.*FLOW_9)/(0.002*pi*RAD_9*VISC_C)) , 0.8) +
(500./RAD_0)*pow(((4.*FLOW_0)/(0.002*pi*RAD_0*VISC_C)) , 0.8));

/* Calculate inner avg wall temp at midspan */
walltemp_c_mid = CTT + q_tot  / (htc_c * area_c);

/* Calculate outside avg htc */
htc_h = (0.037 * K_H * pow(RE,0.8) * pow(PR_H,0.3333)) / (CHORD *
0.001) ;

/* Calculate outside wall avg temp */
walltemp_h_mid = HTT - q_tot / (htc_h * AREA_H);


thread_loop_c(t,domain)
{
 if (SOLID_THREAD_P(t))
 {
  begin_c_loop(c,t)
  {
   C_CENTROID(centroid,c,t);
   x=1000.*centroid[0];
   y=1000.*centroid[1];
   z=1000.*centroid[2];


   /*calculate the distance in x-y plane from centroid to closest
   inside interface*/
   d_1 = sqrt((x - X_1)*(x - X_1) + (y - Y_1)*(y - Y_1)) - RAD_1;
   d_2 = sqrt((x - X_2)*(x - X_2) + (y - Y_2)*(y - Y_2)) - RAD_2;
   temp_1 = MIN(d_1,d_2);
   d_3 = sqrt((x - X_3)*(x - X_3) + (y - Y_3)*(y - Y_3)) - RAD_3;
   temp_2 = MIN(temp_1,d_3);
   d_4 = sqrt((x - X_4)*(x - X_4) + (y - Y_4)*(y - Y_4)) - RAD_4;
   temp_3 = MIN(temp_2,d_4);
   d_5 = sqrt((x - X_5)*(x - X_5) + (y - Y_5)*(y - Y_5)) - RAD_5;
   temp_4 = MIN(temp_3,d_5);
   d_6 = sqrt((x - X_6)*(x - X_6) + (y - Y_6)*(y - Y_6)) - RAD_6;
   temp_5 = MIN(temp_4,d_6);
```

```
   d_7 = sqrt((x - X_7)*(x - X_7) + (y - Y_7)*(y - Y_7)) - RAD_7;
   temp_6 = MIN(temp_5,d_7);
   d_8 = sqrt((x - X_8)*(x - X_8) + (y - Y_8)*(y - Y_8)) - RAD_8;
   temp_7 = MIN(temp_6,d_8);
   d_9 = sqrt((x - X_9)*(x - X_9) + (y - Y_9)*(y - Y_9)) - RAD_9;
   temp_8 = MIN(temp_7,d_9);
   d_0 = sqrt((x - X_0)*(x - X_0) + (y - Y_0)*(y - Y_0)) - RAD_0;
   iwd = MIN(temp_8,d_0);


/* Calculate mass-flow-weighted average coolant exit temp */
   avg_exit_temp = (FLOW_1*TOUT_1 + FLOW_2*TOUT_2 + FLOW_3*TOUT_3 +
   FLOW_4*TOUT_4 + FLOW_5*TOUT_5 + FLOW_6*TOUT_6 + FLOW_7*TOUT_7 +
   FLOW_8*TOUT_8 + FLOW_9*TOUT_9 + FLOW_0*TOUT_0) / (FLOW_1 + FLOW_2
   + FLOW_3 + FLOW_4 + FLOW_5 + FLOW_6 + FLOW_7 + FLOW_8 + FLOW_9 +
   FLOW_0);

   /* delta temp */
   delta_c_temp = CTT – avg_exit_temp;

   /* Approximate wall temp on hot and cold side at top and bottom of
   airfoil based on change in coolant temp through airfoil*/

   walltemp_c_top = walltemp_c_mid + 0.2*delta_c_temp;
   walltemp_c_bot = walltemp_c_mid – 0.8*delta_c_temp;
   walltemp_h_top = walltemp_h_mid + 0.2*(0.5*delta_c_temp);
   walltemp_h_bot = walltemp_h_mid - 0.8*(0.5*delta_c_temp);

   /* The following applies a piecewise (2 segments) linear variation
   of temperature in the spanwise direction */

   z_ref = z - (SPAN / 2.);

   if (z_ref < 0.0)
   {
     h_temp = walltemp_h_mid + (2.*z_ref/SPAN)*(walltemp_h_mid –
     walltemp_h_bot);
     c_temp = walltemp_c_mid + (2.*z_ref/SPAN)*(walltemp_c_mid –
     walltemp_c_bot);
   }

   else
   {
     h_temp = walltemp_h_mid + (2.*z_ref/SPAN)*(walltemp_h_top –
     walltemp_h_mid);
     c_temp = walltemp_c_mid + (2.*z_ref/SPAN)*(walltemp_c_top –
     walltemp_c_mid);
   }

   /*calculate cell initial temperatures*/
   C_UDMI(c,t,INIT_TEMP) = h_temp * (iwd / (C_UDMI(c,t,OW_DIST) + iwd))
   + c_temp * (C_UDMI(c,t,OW_DIST) / (C_UDMI(c,t,OW_DIST) + iwd));
```

```
  /* Set solid cell temperature to the calculated initial temp */
   C_T(c,t) = C_UDMI(c,t,INIT_TEMP);

   }
  end_c_loop(c,t)
 }
}

}
```

Appendix B: ACRL-EVU (Unsteady) Model Equations

*The following is taken from York et al. (2005).

Specific Model Nomenclature

C_μ	turbulent viscosity coefficient
f_μ	viscous wall damping function
f_w	inviscid wall damping function
f_k	structural dissipation damping function
$f_{\varepsilon 2}$	dissipation rate destruction damping function
g_k	near-wall dissipation damping function
i,j	indices
k	turbulent kinetic energy
L_k	Kolmogorov length scale = $(\nu^3/\varepsilon)^{0.25}$ [m]
P_k	turbulent kinetic energy production term
Re_T	turbulence Reynolds number = $k^2/[\nu\varepsilon]$
S	magnitude of mean strain rate tensor = $\sqrt{2S_{ij}S_{ij}}$ [s^{-1}]
S_{ij}	strain rate tensor = $0.5\left(\frac{\partial U_i}{\partial x_j}+\frac{\partial U_j}{\partial x_i}\right)$ [s^{-1}]
$\tilde{U}_i$	instantaneous velocity vector [m/s]
u_i	modeled velocity vector [m/s]
$\|V\|$	velocity magnitude [m/s]
X	strain rate alignment factor

$-\overline{\rho u_i u_j}$ effective Reynolds stress tensor [kg/{ms^2}]

α_T eddy diffusivity for turbulence quantities [m^2/s]

$\bar{\beta}$ time-averaged eddy viscosity limiter

β' instantaneous eddy viscosity limiter

$\tilde{\varepsilon}$ turbulence structural dissipation rate [m^2/s^3]

γ wall distance to turbulence length scale ratio

μ molecular dynamic viscosity [kg/{ms}]

μ_T turbulent viscosity [kg/{ms}]

$\overline{\mu_T}$ turbulent viscosity contribution by time-averaged turbulence [kg/{ms}]

μ_T' turbulent viscosity contribution due to instantaneous departures from time-average [kg/{ms}]

σ limited dimensionless strain rate parameter

σ^* computed dimensionless strain rate parameter

Ω magnitude of mean rotation tensor = $\sqrt{2\Omega_{ij}\Omega_{ij}}$ [s^{-1}]

Ω_{ij} effective turbulence time scale [s]

Model Equations

The unsteady simulations in this study were run using a new, modified eddy-viscosity turbulence model (ACRL-EVU). The new model was implemented into Fluent 6 using the User-Defined Function (UDF) capability. The present version of this model represents a first attempt at being able to predict a wide variety of unsteady, turbulent flows using RANS-based models.

The equations for this model are listed below. The original background model based on Walters (2000) can be obtained by taking the steady contribution of the equations and parameters. The velocity field is decomposed into a resolved and a modeled component, similar to Reynolds decomposition, except that the resolved component is not taken as a time-averaged value, but instead may be unsteady:

$$\tilde{U}_i = U_i + u_i \,. \tag{B.1}$$

The resolved velocity is computed using equations identical to the Reynolds-averaged Navier-Stokes equations, with the only difference being that the unsteady term is included, and the additional terms appearing during the averaging process are effective, rather than actual, Reynolds stresses. The implementation is similar to URANS.

The effective Reynolds stress tensor in the new model is considered to be composed of two parts, one due to the time-averaged velocity field, and the other due to the instantaneous departure of the resolved velocity from the time average. The stress due to the instantaneous departure is damped based on the ratio of turbulent and mean flow time scales. In addition, the Reynolds stress is damped in regions corresponding to non-equilibrium separated shear layers, using the limiter expressed in equation (B.12) below.

The model includes transport equations for the turbulent kinetic energy, *k*, the scalar structural dissipation, $\tilde{\varepsilon}$, and a strain rate parameter, σ^*, included to better resolve the short-time response of the stress tensor to rapid strain rates (Walters, 2000). The effective Reynolds stresses are expressed using the Boussinesq form:

$$\overline{\rho u_i u_j} = \frac{2}{3}\rho k \delta_{ij} - 2\mu_T S_{ij} \,. \tag{B.2}$$

Here the turbulent viscosity, μ_T, is the sum of time-averaged and instantaneous turbulence effects:

$$\mu_T = \overline{\mu_T} + \mu_T' . \tag{B.3}$$

Transport equations for the three computed turbulence quantities are:

$$\frac{D(\rho k)}{Dt} = P_k - \rho f_k \tilde{\varepsilon} - g_k \frac{2\mu k}{d^2} + \frac{\partial}{\partial x_j}\left[\left(\nu + \frac{\alpha_T}{\mathrm{Pr}_k}\right)\frac{\partial k}{\partial x_j}\right] \tag{B.4}$$

$$\frac{D\left(\rho \tilde{\varepsilon}\right)}{Dt} = C_{\varepsilon 1}\frac{\tilde{\varepsilon}}{k}P_k - C_{\varepsilon 2} f_{\varepsilon 2}\rho f_k \tilde{\varepsilon}\frac{\tilde{\varepsilon}}{k} + \frac{\partial}{\partial x_j}\left[\left(\nu + \frac{\alpha_T}{\mathrm{Pr}_\varepsilon}\right)\frac{\partial \tilde{\varepsilon}}{\partial x_j}\right] \tag{B.5}$$

$$\frac{D\left(\rho\sigma^*\right)}{Dt} = C_\sigma \rho\left(< S > - \frac{\tilde{\varepsilon}}{k}\sigma^*\right) + \frac{\partial}{\partial x_j}\left[\left(\nu + \frac{\alpha_T}{\mathrm{Pr}_\sigma}\right)\frac{\partial \sigma^*}{\partial x_j}\right]. \tag{B.6}$$

Based on equation (B.4), the turbulence dissipation rate is comprised of a structural as well as a near-wall component:

$$\varepsilon = f_k \tilde{\varepsilon} + g_k \frac{2\nu k}{d^2} . \tag{B.7}$$

The strain rate parameter (σ^*) represents the local effective total strain (see Walters (2000) for more details). By solving a partial differential equation for σ^*, the strain rate history can be captured. This is not typical in eddy-viscosity models. To achieve an accurate response for rapid or increasing strain rates, the turbulent viscosity is a function of σ^* as opposed to the mean-to-turbulent time-scale ratio. However, the value is only applied in regions were the mean-to-turbulent time-scale ratio is greater than the effective total strain:

$$\sigma = MIN\left(\sigma^*, \frac{< S > k}{\tilde{\varepsilon}}\right). \tag{B.8}$$

The turbulence production is expressed as

$$P_k = \mu_T S^2 . \tag{B.9}$$

The time-averaged contribution to the eddy viscosity is calculated as

$$\overline{\mu_T} = X \bar{\beta} \rho f_\mu f_w C_\mu k \tau_{eff} . \tag{B.10}$$

The symbol X represents a measure of the alignment between the instantaneous and time-averaged resolved strain rate:

$$X = MAX\left(0, \frac{2 < S_{ij} > S_{ij}}{< S > S}\right). \tag{B.11}$$

A limiter is introduced so that the effective viscosity is reduced in non-equilibrium separated shear layers,

$$\bar{\beta} = MIN\left(1, \frac{3.33\tilde{\varepsilon}}{< \Omega > k}\right), if \frac{< \Omega > d}{< |V| >} > 1.1 \tag{B.12}$$

$$\bar{\beta} = 1 \text{, otherwise.}$$

The constants in equation (B.12) are intended to identify non-equilibrium separated shear layers. Their values are a result of information from the literature and the evaluation of flows that exhibit separated shear layers. A variable turbulent viscosity coefficient is included to enforce the realizability constraint on the effective Reynolds stresses:

$$C_\mu = \frac{1}{A_0 + A_s \sigma} , \tag{B.13}$$

and the viscous and inviscid wall damping functions are, respectively,

$$f_\mu = 1 - \exp\left(-\frac{d}{A_\mu L_k}\right), \tag{B.14}$$

$$f_w = \gamma(2 - \gamma) , \tag{B.15}$$

where γ is the ratio of wall distance to large-eddy turbulence length scale:

$$\gamma = MIN\left(1, \frac{C_L d \tilde{\varepsilon}}{k^{1.5}}\right). \tag{B.16}$$

The effective time scale depends on the strain rate parameter as

$$\tau_{eff} = MIN\left(\frac{k}{\tilde{\varepsilon}}, \frac{\sigma}{< S >}\right). \tag{B.17}$$

The instantaneous contribution to the eddy viscosity is computed as:

$$\mu_T^{'} = (1 - X)\beta^{'2}\rho f_\mu f_w C_{\mu,std} k^2 \Big/ \tilde{\varepsilon}, \tag{B.18}$$

where

$$\beta^{'} = MIN\left(\frac{3.33\tilde{\varepsilon}}{Sk}, 1\right). \tag{B.19}$$

The scalar eddy-diffusivity for the turbulence quantities is given as:

$$\alpha_T = \rho f_\mu f_w C_{\mu,std} k^2 \Big/ \tilde{\varepsilon}. \tag{B.20}$$

The remaining damping functions in the transport equations are:

$$f_k = 1 - \exp\left(-\frac{d}{A_k L_k}\right), \tag{B.21}$$

$$g_k = \exp\left(-0.2445\frac{d}{L_k}\right), \tag{B.22}$$

$$f_{\varepsilon 2} = 1 - \frac{2}{9}\exp\left(-\frac{\mathrm{Re}_T^2}{36}\right). \tag{B.23}$$

The last of the above is included to reproduce the correct decay rate of isotropic turbulence, as discussed by Hanjalic and Launder (1976).

The turbulent heat flux is implemented using an effective turbulent Prandtl number along with the eddy viscosity calculated in equation (B.3). The value of the turbulent Prandtl number adopted in the present study is 0.85.

All three of the turbulence transport equations are implemented with zero flux boundary conditions at solid surfaces, and constant inlet values. The effective strain rate parameter, σ^*, is set to zero at the inlet. A list of the constants used in the above equations is given below. These constants are related to the steady physics of the model and were developed by analyzing a series of steady flows (Walters, 2000).

Table B-1. Summary of ACRL-EVU model constants.

Pr_k	1.0
Pr_ε	1.17
Pr_σ	1
$C_{\varepsilon 1}$	1.44
$C_{\varepsilon 2}$	1.9
C_L	2.495
$C_{\mu,std}$	0.09
C_σ	4.2
A_0	4.04
A_k	3.5
A_s	2.12
A_μ	13.5

Appendix C: ACRL-EVRC (Curvature) Model Equations

Specific Model Nomenclature

C_μ	turbulent viscosity coefficient
i, j, k	indices
k	turbulent kinetic energy [m^2/s^2]
l_ε	modified length scale in near-wall region [m]
L_T	length scale of turbulence [m]
Re_y	turbulent Reynolds number for wall-bounded flows = $\frac{\sqrt{k}\cdot y}{\nu}$
S	magnitude of mean strain rate tensor = $\sqrt{2S_{ij}S_{ij}}$ [s^{-1}]
S_{ij}	strain rate tensor = $\frac{1}{2}\left(\frac{\partial U_i}{\partial x_j}+\frac{\partial U_j}{\partial x_i}\right)$ [s^{-1}]
t	time [s]
U	mean component of velocity [m/s]
W	magnitude of rotation term = $\sqrt{2W_{ij}W_{ij}}$ [s^{-1}]
W_{ij}	flow rotation term [s^{-1}]
x	principle coordinate direction [m]
y	smallest distance to solid boundary [m]
ε	turbulence structural dissipation rate [m^2/s^3]
$\overline{\rho}$	density [kg/m^3]
μ	molecular dynamic viscosity [kg/m-s]
μ_T	turbulent viscosity [kg/m-s]

ν kinematic viscosity [m^2/s]

Ω magnitude of mean rotation tensor = $\sqrt{2\Omega_{ij}\Omega_{ij}}$ [s^{-1}]

Ω_{ij} rotation rate tensor = $\frac{1}{2}\left(\frac{\partial U_i}{\partial x_j} - \frac{\partial U_j}{\partial x_i}\right)$ [s^{-1}]

Model Equations

The equations for the new ACRL-EVRC turbulence model developed within the present work are listed below in the generalized, compressible form. Since Chapter 8 is devoted to the model's development, only brief commentary is provided here. The new model is designed for correct sensitivity to streamline curvature and system rotation. It is a two-equation *k*-ε model, and the curvature/rotation effects enter through an algebraic expression for the eddy-viscosity. The model also designed to meet the realizability conditions for the turbulent stresses. The ACRL-EVRC "high-Reynolds number" form is coupled with a new dynamic two-layer near-wall model for integration down to the wall. The new model was designed for robustness in a general purpose RANS solver.

Turbulent Kinetic Energy Transport Equation

$$\frac{\partial(\bar{\rho}k)}{\partial t} + \frac{\partial}{\partial x_j}\left(\bar{\rho}U_j k\right) =$$

$$\frac{\partial}{\partial x_j}\left[\left(\mu + \frac{\mu_T}{\mathrm{Pr}_k}\right)\frac{\partial k}{\partial x_j}\right] + \left[2\mu_T\left(S_{ij} - \frac{1}{3}\delta_{ij}\frac{\partial U_k}{\partial x_k}\right) - \frac{2}{3}\bar{\rho}k\delta_{ij}\right]\frac{\partial U_i}{\partial x_j} - \bar{\rho}\varepsilon \qquad \text{(C.1)}$$

Turbulence Dissipation Rate Transport Equation

$$\frac{\partial(\bar{\rho}\varepsilon)}{\partial t}+\frac{\partial}{\partial x_j}(\bar{\rho}U_j\varepsilon)=$$

$$\frac{\partial}{\partial x_j}\left[\left(\mu+\frac{\mu_T}{\mathrm{Pr}_\varepsilon}\right)\frac{\partial\varepsilon}{\partial x_j}\right]+C_{\varepsilon 1}\frac{\varepsilon}{k}\left[2\mu_T\left(S_{ij}-\frac{1}{3}\delta_{ij}\frac{\partial U_k}{\partial x_k}\right)-\frac{2}{3}\bar{\rho}k\delta_{ij}\right]\frac{\partial U_i}{\partial x_j}-C_{\varepsilon 2}\bar{\rho}\frac{\varepsilon^2}{k} \quad \text{(C.2)}$$

Turbulent Viscosity Definition

$$\mu_T=C_\mu\bar{\rho}\frac{k^2}{\varepsilon} \quad \text{(C.3)}$$

Turbulent Viscosity Coefficient

$$C_\mu=\frac{K_1+K_2C_\mu\left(\frac{Sk}{\varepsilon}\right)^2+K_3C_\mu\left(\frac{Sk}{\varepsilon}\right)+K_4C_\mu^2\left(\frac{Sk}{\varepsilon}\right)^3}{K_5+K_6C_\mu\left(\frac{Sk}{\varepsilon}\right)^2+K_7C_\mu^2\left(\frac{Sk}{\varepsilon}\right)^4+K_8\left(\frac{Wk}{\varepsilon}\right)^2} \quad \text{(C.4)}$$

where

$$S=\sqrt{2S_{ij}S_{ij}} \quad \text{(C.5)}$$

$$W=\sqrt{2W_{ij}W_{ij}} \quad \text{(C.6)}$$

Modified Flow Rotation Term

$$W=\left|S\cdot\left(1-\frac{C_4-4}{C_4-2}\right)+\Omega\cdot\left(\frac{C_4-4}{C_4-2}\right)\right| \quad \text{(C.7)}$$

where the *fluid* rotation rate magnitude is:

$$\Omega=\sqrt{2\Omega_{ij}\Omega_{ij}} \quad \text{(C.8)}$$

Turbulent Stresses (Boussinesq's Assumption)

$$-\overline{\tilde{\rho}u_i u_j} = 2\mu_T S_{ij} - \frac{2}{3}\delta_{ij}\left(\mu_T \frac{\partial U_k}{\partial x_k} + \bar{\rho}k\right) \tag{C.9}$$

Model Turbulence Length Scale

$$L_T = \text{MIN}\left(C_L y, \frac{k^{3/2}}{\varepsilon}\right) \tag{C.10}$$

Near-Wall Turbulence Dissipation Rate

* The following equations are used only when $C_L y$ is the minimum length scale in Equation C.10.

$$\varepsilon = \frac{k^{3/2}}{l_\varepsilon} \tag{C.11}$$

$$l_\varepsilon = C_L y\left[1 - \exp\left(\frac{-\text{Re}_y}{A_\varepsilon}\right)\right] \tag{C.12}$$

Near-Wall Turbulent Viscosity

* The following equation is used only when $C_L y$ is the minimum length scale in Equation C.10.

$$\mu_T = C_\mu \bar{\rho}\sqrt{k} \cdot C_L y\left[1 - \exp\left(\frac{-\text{Re}_y}{A_\mu}\right)\right] \tag{C.13}$$

where

$$\text{Re}_y = \frac{\sqrt{k} \cdot y}{\nu} \quad , \tag{C.14}$$

Model Constants

Table C-1. Constants in ACRL-EVRC model

Pr_k	1.0
Pr_ε	1.19
$C_{\varepsilon 1}$	1.44
$C_{\varepsilon 2}$	1.92
K_1	0.66
K_2	3.9
K_3	1.0
K_4	5.3
K_5	2.9
K_6	17.0
K_7	10.0
K_8	3.84
C_4	0.4
C_L	2.495
A_ε	4.99
A_μ	25.0

REFERENCES

Abdel-Wahab, S. and Tafti, D.K. (2004). "Large Eddy Simulation of Flow and Heat Transfer in a Staggered 45^{o} Ribbed Duct," ASME Paper No. GT2004-53800.

Acharya, S., Myrum, T, Qiu, X., and Sinha, S. (1997). "Developing and Periodically Developed Flow, Temperature and Heat Transfer in a Ribbed Duct," *International Journal of Heat and Mass Transfer*, v. 40, pp. 461-479.

Amano, R., Song, B., and Reza, M. (2005). "A Study of Flow and Heat Transfer in Strongly Curved U-Bend," ASME Paper No. GT2005-68005.

Bardina, J., Ferziger, J.H., and Reynolds, W.C. (1983). "Improved Turbulence Models Based on Large-Eddy Simulation of Homogeneous, Incompressible Turbulent Flows", Stanford University Technical Report TF-19.

Besserman, D.L. and Tanrikut, S. (1991). "Comparison of Heat Transfer Measurements With Computations for Turbulent Flow Around a 180 Degree Bend," ASME Paper No. 91-GT-2.

Bohn, D.E., Bonhoff, B., and Schonenborn, H. (1995). "Combined Aerodynamic and Thermal Analysis of a Turbine Nozzle Guide Vane," *Proceedings of the 1995 Yokohama International Gas Turbine Congress*, IGTC Paper 95-108

Bohn, D.E. and Schonenborn, H. (1996). "3-D Coupled Aerodynamic and Thermal Analysis of a Turbine Nozzle Guide Vane," *Proceedings of the 19th ICTAM, Kyoto, Japan.*

Bohn, D.E., Becker, V.J., and Kusterer, K.A. (1997a). "3-D Conjugate Flow and Heat Transfer Calculations of a Film-Cooled Turbine Guide Vane at Different Operation Conditions," ASME Paper No. 97-GT-23.

Bohn, D.E., Becker, V.J., and Rungen, A.U. (1997b). "Experimental and Numerical Conjugate Flow and Heat Transfer Investigation of a Shower-Head Cooled Turbine Guide Vane," ASME Paper No. 97-GT-15

Bohn, D.E., Becker, V.J., Kusterer, K.A., Otsuki, Y., Sugimoto, T, and Tanaka, R. (1999). "3-D Internal Flow and Conjugate Calculations of a Convective Cooled Turbine Blade with Serpentine-Shaped and Ribbed Channels," ASME Paper No. 99-GT-220.

Bohn, D.E. and Tummers, C. (2003). “Numerical 3-D Conjugate Flow and Heat Transfer Investigation of a Transonic Convection-Cooled Thermal Barrier Coated Turbine Guide Vane With Reduced Cooling Fluid Mass Flow,” ASME Paper No. GT2003-38431.

Bonhoff, B., Parneix, J., Johnson, B., Schabacker, J. and Bolcs, A. (1999). “Experimental and Numerical Study of Flow and Heat Transfer in Coolant Channels With 45 Degree Ribs,” *International Journal of Heat and Fluid Flow*, v. 20, pp. 311-319.

Boussinesq, J. (1877). “Essai Sur La Theorie Des Eaux Courantes,” *Mem. Presentes Acad. Sci.*, v. 23, p. 46.

Bredberg, J. (2002). *Turbulence Modelling for Internal Cooling of Gas Turbine Blades*, Ph.D. Thesis, Chalmers University of Technology, Goteborg, Sweden.

Bredberg, J., and Davidson, L. (1999). “Prediction of Flow and Heat Transfer in a Stationary Two-Dimensional Rib Roughened Passage Using Low-Re Turbulent Models,” IMECH Paper C557/074/99.

Chen, H.C. and Patel, V.C. (1988). “Near-Wall Turbulence Models for Complex Flows Including Separation,” *AIAA Journal*, v. 26, pp. 641-648.

Chmielniak, T., Wroblewski, W., Nowak, G., and Wecel, D. (2003). “Coupled Analysis of Cooled Gas Turbine Blades,” ASME Paper No. GT2003-38657.

Facchini, B., Magi, A., Del Greco, A. (2004). “Conjugate Heat Transfer Simulation of a Radially-Cooled Gas Turbine Vane,” ASME Paper No. GT2004-54213.

Ferguson, J.D., Walters, D.K., and Leylek, J.H. (1998). “Performance of Turbulence Models and Near-Wall Treatments in Discrete Jet Film Cooling Simulations,” ASME Paper No. 98-GT-438.

Fluent Inc. (2005). *Advanced User Defined Function Training*, Fluent Incorporated, Lebanon, New Hampshire, USA.

Fu, S. and Qian, W.Q. (2002). “Development of Curvature Sensitive Nonlinear Eddy-Viscosity Model,” *AIAA Journal*, v. 40, no. 11, pp. 2225-2233.

Gatski, T.B. and Speziale, C.G. (1993). “On Explicit Algebraic Stress Models for Complex Turbulent Flows,” *Journal of Fluid Mechanics*, v. 254, pp. 59-78.

Goldsmith, A., Waterman, and T.E., Hirschhorn, H.J. (1961). *Handbook of Thermophysical Properties of Solid Materials - Volume II: Alloys*. The Macmillan Company, New York, USA.

Han, Z-X, Dennis, B.H., and Dulikravich, G.S. (2000). "Simultaneous Prediction of External Flow-Field and Temperature in Internally Cooled 3-D Turbine Blade Material," ASME Paper No. 2000-GT-253.

Hanjalic, K. and Launder, B.E. (1976). "Contribution Towards a Reynolds Stress Closure for Low Reynolds Number Turbulence," *J. Fluid Mechanics*, v. 74, pp. 593-610.

Heidmann, J., Kassab, A., Divo, E., Rodriguez, F., and Steinthorsson, E. (2003). "Conjugate Heat Transfer Effects on a Realistic Film-Cooled Turbine Vane," ASME Paper No. GT2003-38553.

Holloway, D.S. (2005). *Development of Turbulence Models for Complex, Unsteady Flows: Applications for the Automotive and Gas Turbine Industries*, Ph.D. Thesis, Clemson University, Clemson, SC.

Hylton, L.D., Milhec, M.S., Turner. E.R., Nealy, D.A., and York, R.E. (1983). *Analytical and Experimental Evaluation of the Heat Transfer Distribution Over the Surface of Turbine Vanes*, NASA CR 168015.

Iacovides, H., Launder, B., and Li, H-Y. (1996). "The Computation of Flow Development Through Stationary and Rotating U-Ducts of Strong Curvature," *International Journal of Heat and Fluid Flow*, v. 17, pp. 22-33.

Iacovides, H. and Raisee, M. (1999). "Recent Progress in the Computation of Flow and Heat Transfer in Internal Cooling Passages of Turbine Blades", *International Journal of Heat and Fluid Flow*, v. 20, pp. 320-328.

Jang, Y-J, Chen, H-C, and Han J-C. (2001). "Computation of Flow and Heat Transfer in Two-Pass Channels With 60 Deg Ribs," *ASME Journal of Heat Transfer*, v. 123, pp. 563-575.

Johnston, J.P., Halleen, R.M., and Lezius, D.K. (1972). "Effects of Spanwise Rotation on the Structure of Two-Dimensional Fully-Developed Channel Flow," *Journal of Fluid Mechanics*, v. 56, pp. 533-558.

Kim, J., Moin, P., and Moser, R.D. (1987). "Turbulence Statistics in Fully-Developed Channel Flow at Low Reynolds Number," *Journal of Fluid Mechanics*, v. 177, pp. 133-186.

Kristoffersen, R. and Andersson, H.I. (1993). "Direct Numerical Simulation of Low-Reynolds-Number Turbulent Flow in a Rotating Channel," *Journal of Fluid Mechanics*, v. 256, pp. 163-197.

Kusterer, K., Bohn, D., Sugimoto, T., and Tanaka, R. (2004). "Conjugate Calculations for a Film-Cooled Blade Under Different Operating Conditions,"ASME Paper No. GT2004-53719.

Kusterer, K., Torsten, H., Bohn, D., Sugimoto, T., and Tanaka, R. (2005). "Improvement of a Film-Cooled Blade by Application of the Conjugate Calculation Technique," ASME Paper No. GT2005-68555.

Launder, B.E. (1989). "Second Moment Closure: Present … and Future?," *International Journal of Heat and Fluid Flow*, v. 10, pp. 282-300.

Launder, B.E. and Spalding, D.B. (1972). *Lectures in Mathematical Models of Turbulence*. Academic Press, London, England.

Liou, T.-M., Hwang, J.-J., and Chen, S-H. (1991). "Turbulent Heat Transfer and Fluid Flow in a Channel with Repeated Rib Pairs," *ASME/JSME Thermal Engineering Proceedings*, v. 3, pp. 205-212.

Liou, T.-M., Hwang, J.-J., and Chen, S-H. (1992). "Turbulent Transport Phenomena in a Channel with Periodic Rib Turbulators," *J. Thermophysics and Heat Transfer*, v. 6, pp. 513-521.

Mazur, Z., Hernandez-Rossette, A., Garcia-Illescas, R., and Luna-Ramirez, A., (2005). "Analysis of Conjugate Heat Transfer of a Gas Turbine First Stage Nozzle," ASME Paper No. GT2005-68004.

McDowell, P., York, W., Walters, D., and Leylek, J. (2003). "Effects of 3-D Local Unsteadiness on Heat Transfer Prediction in Turbulated Passages," ASME Paper No. IMECE2003-42268.

Monson, D.J., Seegmiller, H.L., McConnaughey, P.K., and Chen, Y.S. (1990). "Comparison of Experiment With Calculations Using Curvature-Corrected Zero and Two Equation Turbulence Models for a Two-Dimensional U-Duct." AIAA Paper No. 90-1484.

Nikas, K.P. and Iacovides, H. (2003). "The computation of Flow and Heat Transfer Through Square-Ended U-Bends, Using Low-Reynolds-Number Models," *International Journal of Numerical Methods for Heat and Fluid Flow*, v. 14, no. 3, pp. 305-324.

Patankar, S.V. (1980). *Numerical Heat Transfer and Fluid Flow*, Hemisphere, Washington, D.C.

Prakash, C. and Zerkle, R. (1995). "Prediction of Turbulent Flow and Heat Transfer in a Ribbed Rectangular Duct With and Without Rotation," *ASME Journal of Turbomachinery*, v.117, pp. 255-264.

Rahman, M.M. and Siikonen, T. (2005). "An Eddy-Viscosity Model With Near-Wall Modifications." *International Journal for Numerical Methods in Fluids*," v. 49, pp. 975-997.

Rigby, D.L. and Lepicovsky, J. (2001). “Conjugate Heat Transfer Analysis of Internally Cooled Configurations,” ASME Paper No. 2001-GT-0405.

Rigby, D., Ameri, A., and Steinthorsson, E. (2002). “Computation of Turbulent Heat Transfer on the Walls of a 180 Degree Turn Channel With a Low Reynolds Number Reynolds Stress Model,” ASME Paper No. GT-2002-30211.

Rodi, W. (1980). “Turbulence Models and Their Applications in Hydraulics – A State of the Art Review,” Technical Memo, University of Karlsruhe.

Rumsey, C.L., Gatski, T.B., and Morrison, J.H. (2000). “Turbulence Model Predictions of Strongly Curved Flow in a U-Duct.” *AIAA Journal*, v. 38, no. 8, pp. 1394-1402.

Saha A. K., and Acharya, S. (2003). “Flow and Heat Transfer in an Internally Ribbed Duct with Rotation: An Assessment of LES and URANS,” ASME Paper No. GT2003-38619.

Saha, A.K. and Acharya, S. (2004). “Unsteady RANS Simulation of Turbulent Flow and Heat Transfer in Ribbed Coolant Passages of Different Aspect Ratios,” ASME Paper No. GT2004-53986.

Sarkar, S. and Balakrishnan, L. (1990). “Application of a Reynolds-Stress Turbulence Model to the Compressible Shear Layer,” ICASE Report 90-18, NASA CR 182002.

Sewall, E.A. and Tafti, D.K. (2004). “Large Eddy Simulation of the Developing Region of a Stationary Ribbed Internal Turbine Blade Cooling Channel,” ASME Paper No. GT2004-53832.

Sewall, E.A. and Tafti, D.K. (2005). “Large Eddy Simulation of Flow and Heat Transfer in the 180^{o} Bend Region of a Stationary Ribbed Gas Turbine Internal Cooling Duct,” ASME Paper No. GT2005-68518.

Shih, T. –H., Liou, W.W., Shabbir, A., and Zhu, J. (1995). “A New k-ε Eddy-Viscosity Model for High Reynolds Number Turbulent Flows: Model Development and Validation,” *Computers and Fluids*, v. 24, no. 3, pp. 227-238.

Shur, M.L., Strelets, M.K., Travin, A.K., and Spalart, P.R. (2000). “Turbulence Modeling in Rotating and Curved Channels: Assessing the Spalart-Shur Correction,” *AIAA Journal*, v. 38, no. 5, pp. 784-792.

Spalart, P.R. and Allmaras, S.R. (1992). “A One-Equation Turbulence Model for Aerodynamic Flows,” AIAA Paper No. 92-0439.

Tafti, D.K. (2003). “Large-Eddy Simulations of Heat Transfer in a Ribbed Channel for Internal Cooling of Turbine Blades,” ASME Paper No. GT2003-38122.

Takahashi, T., Watanabe, K., and Takahashi, T. (2000). “Thermal Conjugate Analysis of First Stage Blade in a Gas Turbine,” ASME Paper No. 2000-GT-251.

Takahashi, T., Watanabe, K., and Takayuki, S. (2005). “Conjugate Heat Transfer Analysis of a Rotor Blade With Rib-Roughened Internal Cooling Passages,” ASME Paper No. GT2005-68227.

Taslim, M.E., Li, T., and Spring, S.D. (1998). “Measurements of Heat Transfer Coefficients and Friction Factors in Passages Rib-Roughened on All Walls,” *ASME Journal of Turbomachinery*, v. 120, pp. 564-570.

Viswanathan, A.K. and Tafti, D.K. (2005). “Large Eddy Simulation in a Duct With Rounded Skewed Ribs,” ASME Paper No. GT2005-68117.

Viswanathan, A.K. and Tafti, D.K. (2005). “Detached Eddy Simulation of Flow and Heat Transfer in a Stationary Internal Cooling Duct With Skewed Ribs,” ASME Paper No. GT2005-68118.

Walters, D.K. (2000). *Development of Novel Turbulence Modeling Techniques for Turbomachinery Applications*. Ph.D. Thesis, Clemson University, Clemson, SC.

Walters, D.K., and Leylek, J.H. (2000). “Impact of Film-Cooling Jets on Turbine Aerodynamic Losses,” *ASME Journal of Turbomachinery*, v.122, pp. 537-545.

Watanabe, K. and Takahashi, T. (2002). “LES Simulation and Experimental Measurement of Fully Developed Ribbed Channel Flow and Heat Transfer,” ASME Paper No. GT-2002-30203.

Wilcox, D.C. (1988), "Re-assessment of the Scale-Determining Equation for Advanced Turbulence Models", *AIAA Journal*, v. 26, pp. 1414-1421.

Wolfstein, M. (1969). “The Velocity and Temperature Distribution of One-Dimensional Flow With Turbulence Augmentation and Pressure Gradient,” *International Journal of Heat and Mass Transfer*, v. 12, pp. 301-318.

Yakhot, V. and Orszag, S.A. (1986). “Renormalization Group Analysis of Turbulence: I. Basic Theory,” *Journal of Scientific Computing*, v. 1, pp. 1-51.

York, W.D. (2000). *A Detailed Numerical Investigation of Turbine Airfoil Leading Edge Film Cooling*, M.S. Thesis, Clemson University, Clemson, SC.

York, W.D., Holloway, D.S., and Leylek, J.H. (2005). “Prediction of Heat Transfer in a Ribbed Channel: Evaluation of Unsteady RANS Methodology,” ASME Paper No. GT2005-68821.